Fatigue Crack Growth Behaviour in Proton Irradiated Austenitic Stainless Steel

Thesis submitted in accordance with the requirements of the University of Liverpool for the degree of Doctor in Philosophy by Rory Philip Spencer.

September 2019

Abstract

This thesis describes the work undertaken over three years into the investigation of the effect of proton irradiation on the fatigue crack behaviour of an austenitic stainless steel. Many in-core nuclear reactor components that are subjected to radiation damage and repeated thermal stresses are made from austenitic stainless steels. A thorough understanding of the effect of the material changes caused by the radiation damage on the fatigue cracking behaviour is essential for safely extending the lifetime of nuclear plant components.

Proton irradiation from an ion accelerator has been used in this study as a surrogate for the neutron irradiation experienced by real components. Despite the different interactions of protons and neutrons with matter, under certain conditions, proton damage can result in a similar damaged end-state to neutrons. In contrast to reactor neutrons, accelerated protons can be produced at a higher rate, allowing component end-of-life damage levels to be reached in a much shorter time.

A review of the literature identified thermoelastic stress analysis (TSA) as the technique most capable of measuring the required variables during a fatigue crack growth test, i.e. stress intensity factor and plastic zone size. Two key gaps in the literature were identified. Firstly, few studies of fatigue crack growth in irradiation damaged specimens exist and those that do typically report a small number of specimens. Due to the inherent variability of fatigue crack growth, a large number of specimens should be tested at each damage level to obtain statistically meaningful data. Secondly, fatigue crack growth studies rely on analytical relations based on crack length for both stress intensity factor and plastic zone size measurements in many cases. Using TSA allows direct measurement of these quantities and hence a deeper understanding of the actual specimen behaviour.

A novel method was developed to measure the extent of the cyclic plastic zone based on the in-phase second harmonic temperature signal. This allowed measurement of the plastic zone area, without prior knowledge of the yield strength. Further, the total energy dissipated from the plastic zone could be calculated, without assuming the plastic zone size and shape. Investigations of the second harmonic temperature data revealed signals originating in the crack flanks that were demonstrated to be related to crack closure. This allowed a simple binary check for closure without further data analysis.

A number of austenitic compact tension specimens were prepared and irradiated using accelerated protons at a set of increasing proton fluence levels. Following irradiation, the specimens were loaded in fatigue and imaged regularly with a TSA system as the crack grew. This gave simultaneous measurements of plastic zone size and effective stress intensity factor, and represented the first time the TSA technique has been used to investigate radiation damaged material. The experimentally obtained stress intensity factors and crack growth rates were fitted using the Paris' Law model and analysis of covariance suggested that there is not a statistically significant difference in the gradient of the fit with increasing irradiation damage. However, a significant effect ($p < 0.05$) was found in the offset value. This suggests that greater radiation damage causes a greater reduction in crack growth rate, in agreement with literature.

Measurements of the TSA output suggest that, contrary to theory, the apparent plastic zone increased in size with more radiation damage. However, the dissipated energy from the plastic zone did tend to increase with radiation damage. Hence, it is hypothesised that the physical plastic zone decreases in size due to the greater hardness induced by the irradiation, but emits a larger amount of energy as the vacancies and interstitials generated by the radiation damage make dislocation movement more energetically difficult, resulting in an apparent increase in plastic zone size when measured using the TSA system.

Acknowledgements

I am grateful for the support of my supervisor, Professor Eann Patterson, during this project and the helpful advice of Dr Maulik Patel.

The helpful conversations with industrial sponsors Dr Nick Riddle, Dr Dan Cogswell and Dr Keith Wilford all of Rolls-Royce have been invaluable.

Special thanks go to Jijimon Mathew for his manufacturing expertise in producing the specimens and equipment modifications for this work and to Dave Atkinson for training and support in specimen surface preparation, microscopy and microhardness testing.

My work at DCF would have been impossible if not for the help and guidance given by Samir de Moraes Shubeita. Thanks also go to Nick Mason, Andy Smith and Paul Wady for their experimental support.

Finally, I would like to thank my friends and family, and in particular my wife, Sally, for all her invaluable support.

Contents

List of Tables

List of Figures

Chapter 1

Introduction

1.1 Background

1.1.1 Pressurized Water Reactors

Pressurized water reactors (PWR) are a type of light water reactor (LWR) that uses light water as both a coolant and moderator. PWRs were initially developed for naval use, beginning with the first nuclear submarine, the U.S.S *Nautilus*. PWRs are also used globally for commercial grid electricity generation. The United Kingdom has one PWR located at Sizewell B that has been operational since 1995.

The PWR design is built around a central pressure vessel containing the nuclear core. A primary coolant loop connects the pressure vessel to steam generators and pressurizers. A secondary loop runs from the steam generators to a turbine to generate power. The pressure in the primary loop is kept high, typically 15.5MPa, to prevent the water boiling, allowing the water temperature to reach 300°C. The pressurizer in the primary loop consists of a pressure vessel partially filled with water and equipped with cooling spray nozzles and submerged electric heating elements to maintain the pressure in the loop during thermal transients.

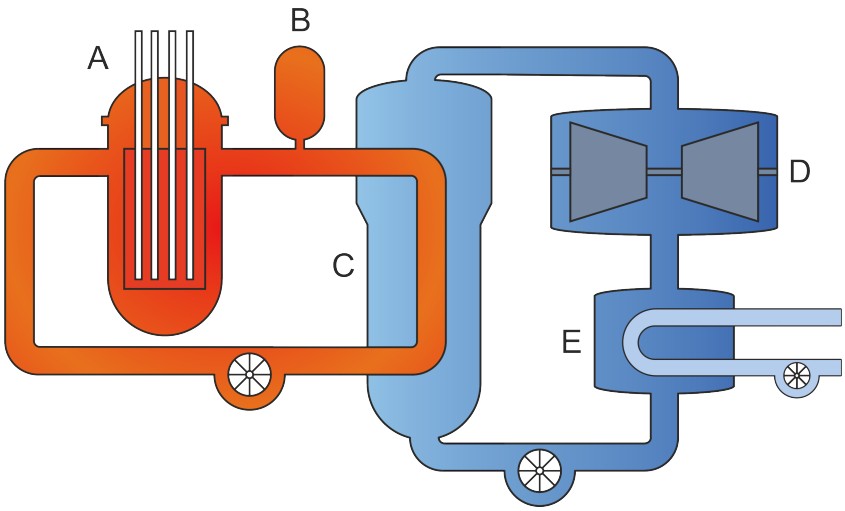

Figure 1.1: Schematic showing main components of a PWR. The primary loop is red, with: the reactor pressure vessel containing the core (A), the pressurizer (B). The secondary loop (blue) meets the primary loop in the steam generator (C), which turns water into steam to drive the turbines (D). The steam is returned to liquid phase in the condenser (E).

PWRs are fuelled by enriched uranium, in the form of uranium dioxide pellets. The pellets are held within fuel pins, typically made of a zirconium alloy, which are themselves grouped together into fuel assemblies.

The reactivity and therefore power output of the core is controlled by the use of control rods and the water chemistry of the primary loop. Control rods are made from neutron absorbing materials and are able to move in and out of the core. Changing the water chemistry is known as using a chemical shim and involves the introduction of a neutron absorbing chemical to the primary loop coolant, such as boric acid. Absorbing neutrons decreases the neutrons available to cause further fission events, thus decreasing the reactivity.

1.1.2 Thermal Stresses

Thermal stresses are caused by the non-uniform thermal expansion of materials due to non-uniform temperature distributions. These repeated thermal stresses act as fatigue loading on the components and can result in fatigue cracking. Such situations are common

during start-up, shut down and during a change of power output.

Typically, nuclear reactors used for power generation are assumed to provide the grid baseload electricity with more rapidly changeable sources such as gas turbines used to load-follow the demand. However, countries such as France, with a high percentage of nuclear power, and Germany, with a high proportion of intermittent power sources, use nuclear reactors in a load-following role [1]. Thermal stresses and the resulting fatigue need to be considered in the design and regulation of PWRs that are intended to perform load-following as they will potentially experience more and larger thermal transients.

1.1.3 Component End-of-Life

Nuclear reactors are designed to maximise their service life, but different components will be exposed to various deleterious conditions, such as fatigue loading, corrosion and radiation damage.

Towards the end-of-life of the core, the core internal structure of a civil PWR can expect to see tens of displacements per atom (dpa) of radiation damage in components close to the fuel elements, whereas the reactor pressure vessel (RPV) itself would only see up to one dpa [2].

The lifetime of components subjected to fatigue loading is typically limited by the presence of a sufficiently large crack, the length of which is dictated by an appropriate standard, such as the ASME Boiler and Pressure Vessel code [3]. If a large component such as the RPV or steam generator is deemed unsafe, then the plant will be unable to operate.

It is therefore of fundamental importance to understand the fatigue behaviour, in particular the cracking behaviour, associated with the different conditions and damage levels these components will see over their lifetime, so as to inform the design and maintenance strategies to safely maximise plant lifetime.

1.2 Research Aims

The aim of the project was to design and perform a series of experiments to investigate the effect of radiation damage on fatigue crack growth in an austenitic stainless steel.

To achieve that aim, the following objectives had to be met:

1. Characterise the fatigue crack growth behaviour and plastic zone morphology in as-received material;
2. Induce radiation damage using an ion beam as a surrogate for neutron irradiation;
3. Characterise the fatigue crack growth behaviour and plastic zone morphology in the irradiated material; and
4. Determine the relationship between level of radiation damage and fatigue cracking behaviour.

1.3 Thesis Structure

This thesis describes the experimental program undertaken to determine the extent of the effect of radiation damage on fatigue crack growth in irradiation damaged austenitic stainless steel, with a particular focus on crack tip plastic zone behaviour.

Chapter 2 provides an introduction to fracture mechanics and reviews the available measurement techniques to assess their suitability for the project. The effects of radiation damage are outlined and use of proton irradiation as a surrogate for neutron is justified. Finally, the results of previous studies investigating fatigue crack growth and irradiation damage are reviewed, and knowledge gaps are identified.

The experimental methods used in the project are described in detail in chapter 3. A detailed description of the irradiation procedure is provided. Modifications and updates to

the techniques and experimental set up are outlined.

The development of a new technique for measuring crack tip plasticity is outlined in chapter 4. The necessity for a new method is demonstrated using finite element analysis and data. An overview of relevant theory from the literature is given, followed by a demonstration of the utility of the new method for: measurement of the plastic zone area, closure detection and measurement of the energy dissipated in the crack tip region.

Chapter 5 outlines the design and results of the main experimental program, concerning the irradiation and fatigue crack growth testing of thin-gauge compact tension specimens. A short follow-up experiment is included to qualitatively demonstrate some of the behaviour found in the main tests. Finally, a discussion of the results considers the effects of irradiation on the fatigue crack growth and plastic zone behaviour, with reference to the results of comparable studies in the literature.

Chapter 6 presents the conclusions of the experimental program and highlights the advances made and techniques developed during this work. Possible directions for future work are provided, to help guide interested future researchers.

Chapter 2

Literature Review

This chapter provides an overview of the relevant fracture mechanics concepts and reviews available techniques for measurement of stress intensity factors and crack tip plastic zones. An introduction to radiation damage, its effects on materials and the use of accelerated protons as a surrogate is provided. A review of irradiation damage fatigue crack growth studies is undertaken, and gaps in knowledge are identified.

2.1 Introduction to Fracture Mechanics

Fracture mechanics is the study of the initiation and propagation of cracks in materials. Crack growth reduces the service lifetime of components and can ultimately result in their failure. A thorough understanding of crack growth behaviour in a variety of environments is required to make informed decisions on the service and replacement of components to ensure operational safety.

This section will provide an introduction to the concepts of fracture mechanics as they have been developed historically. Beginning with the study of fracture of brittle materials subject to static loading, then including the effects of ductile materials, before finally applying the lessons learned in static fracture to the crack growth caused by fatigue loading.

2.1.1 Linear Elastic Fracture Mechanics

Linear Elastic Fracture Mechanics (LEFM) is study of the fracture of materials that remain predominantly linear elastic.

Fracture of materials occurs when the applied stress is high enough to overcome the cohesive strength of the atomic bonds holding the material together. However, real materials will fracture long before they reach the stresses required to rupture bonds. In 1913 a mathematical analysis of elliptical cracks by Inglis [4] demonstrated the stress concentration effect of cracks. When the ellipse axes are equal in length, the crack is circular and the stress increases by a factor of 3 near to the crack. By increasing the length of one axis the shape approaches that of a sharp crack. As the crack tip radius ρ approaches zero, the stress concentration effect results in infinite stresses at the crack, which is evidently unrealistic.

In 1920, by studying brittle solids such as glass, A.A. Griffith [5] proposed a global energy balance argument for the crack problem to obviate the apparent paradox of infinite crack tip stresses. The introduction of a crack to an infinite plate reduces the elastic strain energy stored in the plate; however the creation of new crack surfaces requires energy. Therefore, if the strain energy released by an increment of crack growth is greater than the energy required to form the new fracture surfaces, the crack growth is energetically favourable.

In an attempt to expand Griffith's model for brittle solids to account for solids that exhibit limited plasticity at the crack tip, Irwin [6] introduced the energy release rate $\mathcal{G}$, the rate of change of potential energy with crack area. Crack growth occurs in this model when $\mathcal{G}$ exceeds the resistance to crack growth, $\mathcal{G}_c$, where $\mathcal{G}_c$ is a measure of fracture toughness that includes the surface energy factor proposed by Griffith with the addition of a plastic strain work component to account for the small scale yielding.

Using the elastic stress field solutions developed by Westergaard [7], Irwin [8] later introduced the concept of the stress intensity factor K as a local parameter governing the

crack tip stress field and crack growth behaviour. In polar coordinates centred on the crack tip, this is expressed as:

$$\sigma_{ij} = \frac{k}{\sqrt{2\pi r}} f_{ij}(\theta) + \sum_{m=0}^{\infty} A_m r^{\frac{m}{2}} g_{ij}^{m}(\theta) \tag{2.1}$$

$$\sigma_{ij} = \frac{K}{\sqrt{2\pi r}} f_{ij}(\theta) \tag{2.2}$$

where σ_{ij} is the stress tensor, k is a constant, K is the stress intensity factor and $f_{ij}(\theta)$ is a dimensionless function based on the geometry and loading of the cracked specimen.

Cracking can be split into three distinct modes: opening mode I, in-plane shear mode II and out-of-plane shear mode III. The mode will change the proportionality of k and f_{ij}. This is denoted as a subscript on the stress intensity factor K, such as the mode I stress intensity factor K_I.

Under the assumption of similitude, where cracks with similar K will exhibit similar growth behaviour, the stress intensity factor uniquely characterises the stress state present in the vicinity of the crack tip. For example, for a mode I crack under plane stress conditions:

$$\sigma_{xx} = \frac{K_I}{\sqrt{2\pi r}} \cos\left(\frac{\theta}{2}\right)\left[1 - \sin\left(\frac{\theta}{2}\right)\sin\left(\frac{3\theta}{2}\right)\right] \tag{2.3}$$

$$\sigma_{yy} = \frac{K_I}{\sqrt{2\pi r}} \cos\left(\frac{\theta}{2}\right)\left[1 + \sin\left(\frac{\theta}{2}\right)\sin\left(\frac{3\theta}{2}\right)\right] \tag{2.4}$$

$$\sigma_{xy} = \frac{K_I}{\sqrt{2\pi r}} \cos\left(\frac{\theta}{2}\right)\sin\left(\frac{\theta}{2}\right)\cos\left(\frac{3\theta}{2}\right) \tag{2.5}$$

$$\sigma_{zz} = 0 \tag{2.6}$$

Irwin also demonstrated that the global parameter $\mathcal{G}$ was related to the local parameter K in the following way:

$$\mathcal{G} = \frac{K^2}{E} \tag{2.7}$$

K can therefore be used a single parameter describing crack growth behaviour in the case where the crack tip stress field remains predominantly elastic. This also allows a crack

growth criterion similar to that of the strain energy release rate to be applied, such that a crack will grow when K exceeds some critical value, K_c.

However, the problem Inglis identified reappears. Close to the crack tip, as $r \to 0$, the terms in the summation in equation (2.1) become zero or finite and equation (2.1) reduces to equation (2.2), and the leading term becomes infinite. This is known as a stress singularity and the region in which equation (2.2) is valid is known as the singularity dominated zone. The singularity cannot be physical however, as it would imply failure of a cracked body at any applied load. Rather than return to a energy-based approach like Griffith, modifications can be made to the stress intensity approach to account for the physical effects that reduce the crack tip stress, such as local yielding.

2.1.2 Crack Tip Plasticity

The effect of the stress singularity raises the stresses in the immediate vicinity of the crack tip to a level higher than the yield stress of the material. This results in a region of material that is plastically deformed, called the crack tip plastic zone. Provided the plastic zone is small compared to the crack length, an assumption called small-scale yielding, it will not overwhelm the effect of the elastic stress field [9] and the stress intensity factor will still control the majority of the crack growth behaviour.

In LEFM, corrections for the plastic zone size can be applied to include the effects of yielding without performing a non-linear analysis. The correction is made by increasing the nominal length of the crack by the size of the plastic zone. This accounts for the reduced stress carried by the plastic zone compared to situation where it remained elastic.

Two approaches to estimating the size of the plastic zone for mode I cracks were developed at similar times: the Irwin model and the Dugdale strip-yield model. These are shown diagrammatically in figure 2.1.

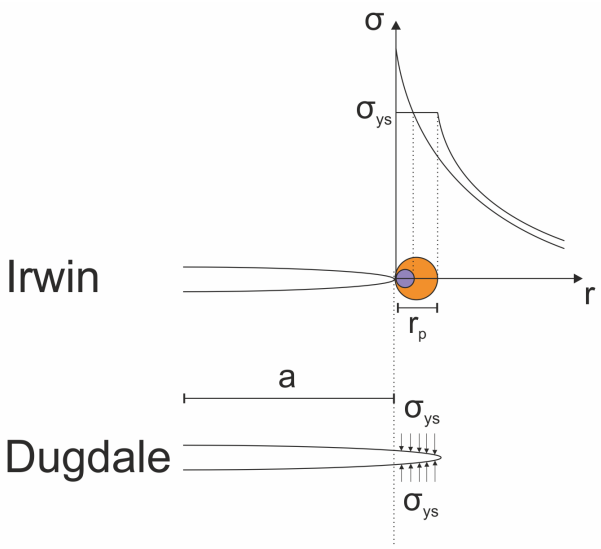

Figure 2.1: Diagram showing the different approaches taken to approximate plastic zone corrections by Irwin & Dugdale.

Irwin's model [10] assumes a circular plastic zone centred upon a notional crack increment of ΔA and with a radius of ΔA, giving a full plastic zone length of $r_p = 2\Delta A$. A first-order estimate of this radius can be obtained by assuming that only the material stressed above the yield stress forms the plastic zone. However, the yielded material of the plastic zone can not support any stresses higher than the yield stress, so these must be redistributed in order for the plastic zone estimate to be correct. This is shown in figure 2.1 as the purple and orange circles. The size of the plastic zone generated by the stress redistribution is given by:

$$r_p = \frac{1}{\pi}\left(\frac{K_I}{\sigma_{YS}}\right)^2 \tag{2.8}$$

The strip yield model approach taken by Dugdale [11] and Barrenblat [12] instead imagines the plastic zone as an infinitely thin strip of yielded material extending a length r_p from the crack tip. An estimate of the plastic zone length is achieved by superimposing two elastic solutions: of the crack under remote tension and the crack with closure stresses. This gives:

$$r_p = \frac{\pi}{8}\left(\frac{K_I}{\sigma_{YS}}\right)^2 \tag{2.9}$$

The two different approaches lead to solutions of the same form and with a very similar

constant: $1/\pi = 0.318$ and $\pi/8 = 0.392$ and therefore predict similar plastic zone sizes.

Thus far both models have considered plastic zones only in their extent ahead of the crack tip as a means to nominally increase crack length. However, plastic zones will have an associated shape as well as length and this shape is dependent on the cracking mode and specimen constraint (i.e. a plane stress or plane strain state). By applying a yield criterion such as von Mises to the stresses given in equations (2.3) to (2.5), it is possible to generate an estimate of plastic zone shape. However, the same caveat applies as with Irwin's plastic zone analysis as the equations are based on purely elastic considerations and do not have the stress redistribution taken into account.

2.1.3 Elastic-Plastic Fracture Mechanics

Rather than modifying LEFM to account for the effects of plasticity, it is possible to use different methods, belonging to elastic-plastic fracture mechanics (EPFM).

Rather than the stress intensity factor K, EPFM typically utilises the non-linear elastic energy release rate J to characterise crack growth behaviour. J is broadly analogous to K and is obtained by performing a line integral of the strain energy density around the crack tip.

EPFM is more suitable than LEFM when the size of the plastic zone is large compared to the crack dimensions and the stress intensity factor concept is no longer applicable. It is not expected that EPFM methods will be required in this work.

2.1.4 Fatigue Cracking

Fatigue is the repeated application of load to a material, in the laboratory setting this is generally sinusoidal loading between $P_{\min}$ and $P_{\max}$, generating an alternating stress $\Delta\sigma = \sigma_{\max} - \sigma_{\min}$. In the uniaxial loading case this can be represented as:

$$\sigma(t) = \sigma_m + \Delta\sigma \sin(2\pi f t) \tag{2.10}$$

where: σ is the stress at time t, σ_m is the mean stress, $\Delta\sigma$ is the stress amplitude and f is the loading frequency.

Typically, the magnitude of the applied stresses are much less than the yield stress of the material. The ratio between the minimum and maximum stress is called the R-ratio, where $R = \frac{\sigma_{\min}}{\sigma_{\max}}$. A positive R-ratio indicates tension-tension loading, $\sigma_m > 0$, whereas an R-ratio of -1 indicates fully reversed loading, $\sigma_m = 0$.

Fatigue cracks will initiate after a number of load cycles, usually at a local stress concentration, and will then subsequently propagate through the material. Initiation of a crack is generally dominated by material microstructure or micro-scale defects, but once a crack has initiated, fracture mechanics can be used to understand its behaviour.

Prior discussions concerned the process of fracture in statically loaded materials. Despite this, the stress intensity factor concept developed statically is also useful to characterising the behaviour of cracks growing under fatigue conditions. This observation was made by Paris et al [13][14], who formulated an empirical equation, now known as the Paris Law, based on K to describe fatigue crack growth behaviour:

$$\frac{da}{dN} = C\left(\Delta K\right)^m \tag{2.11}$$

where: $\frac{da}{dN}$ is the crack growth rate, ΔK is the amplitude of the stress intensity factor and C,m are constants to be empirically determined.

Figure 2.2 shows the typical behaviour of a fatigue crack. The crack is initiated in region I and undergoes a rapid change in crack growth rate. In region II, the crack growth is stable and the crack growth rate increases linearly. Failure occurs in region III as the crack growth rate rapidly increases.

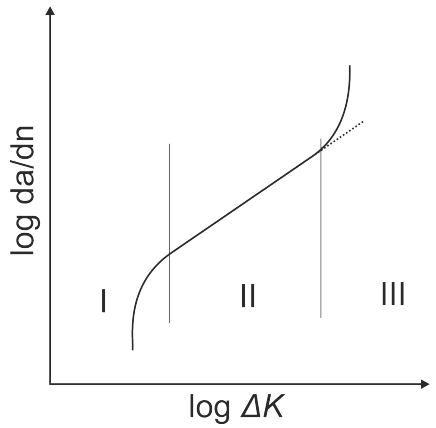

Figure 2.2: Schematic log-log plot of stress intensity factor amplitude, ΔK, and crack growth rate, $\frac{da}{dN}$, showing typical fatigue crack growth behaviour. The crack initiates in region I, undergoes stable growth in region II and transitions to unstable rapid crack growth in region III.

Soon after the introduction of the Paris Law, the influence of other factors on the crack growth rate were noticed. Broek & Schijve [15] found an influence of the R-ratio on the crack growth rate in cracked aluminium specimens, where $R = \frac{K_{\min}}{K_{\max}}$. Higher R-ratios correlated with larger observed crack growth rates and therefore had to be considered when formulating a crack growth law.

Forman et al [16] expanded on this further, taking into account the R-ratio and the onset of instability as the crack progresses into region III. It was assumed that $\frac{da}{dn} \to \infty$ when $K_{\max} \to K_c$. This lead to the modification of equation 2.11 to:

$$\frac{da}{dN} = \frac{C(\Delta K)^m}{(1-R)K_c - \Delta K} \tag{2.12}$$

2.1.5 Crack Closure

Paris Law type equations are useful, but do not capture the full complexity of behaviour that is present in fatigue crack growth. The crack closure phenomenon is an example of this complexity. Elber [17] first observed crack closure occurring in aluminium 2024-T3 specimens, as their compliance varied over the load cycle. Compliance is a measure of how

much the material deforms when subjected to a load and it was found that near the crack tip the compliance changed between two regimes: one similar to an uncracked specimen and a lower regime. It would be expected that the compliance of a cracked specimen is lower than an uncracked specimen as the crack will reduce the specimen stiffness. Elber's observations during the lower load portions of the load cycle suggested that the specimen was behaving like an uncracked specimen and he concluded that crack closure was the cause of this change.

Elber introduced the concept of the opening stress intensity factor K_{op}, above which the crack behaves as if it is open and below which the crack is partially or fully closed. To quantify the closure effects Elber [18] later introduced the effective stress intensity factor, ΔK_{eff} and the effective stress range ratio U, given as:

$$U = \frac{\Delta K_{\mathrm{eff}}}{\Delta K} = \frac{K_{\max} - K_{\mathrm{op}}}{K_{\max} - K_{\min}} \tag{2.13}$$

Elber argued that the crack could not grow during the portion of the load cycle when the crack was closed and therefore the stress intensity factor experienced at the crack tip was consequently reduced. The proposed mechanism for the closure was residual plastic deformation of the crack flanks. During fracture the plastic zone deforms permanently and hence, when the crack length increases and the prior plastic zone material becomes the flank it is no longer compatible. The deformed flanks therefore come together as the load reduces. This is shown diagrammatically in figure 2.3.

The effects of closure are related to the R-ratio, as higher R-ratios correspond to a greater time during the load cycle with the crack open. Elber noted closure effects up to $R = 0.7$ in his aluminium specimens.

Subsequently, additional closure mechanisms have been identified such as oxide-induced closure and roughness-induced closure [19].

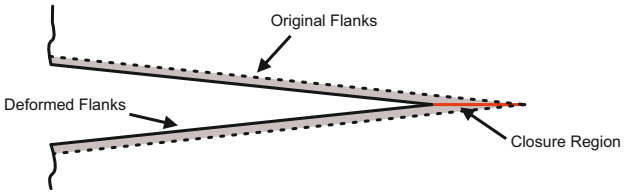

Figure 2.3: Diagram showing closure effect due to crack flank contact. Plastic deformation in the crack tip plastic zone becomes the crack flank as the crack continues to grow. This material has been permanently deformed in the vertical axis, and hence the faces contact one another during unloading.

2.1.6 Cyclic Crack Tip Plasticity

As with the stress intensity factor concept extending from static fracture to fatigue fracture, the concept of the crack tip plastic zone is also applicable in fatigue. The main difference is the absence of a singular K value, which must be replaced with ΔK in equations 2.8 and 2.9. However, a simple substitution is not analytically correct and a different approach must be used.

During the load cycle, a monotonic plastic zone is formed as with the static case, but dependent on $K_{\max}$ rather than K. Upon load reversal, a smaller plastic zone is formed called the cyclic plastic zone. Rice [9] used a superposition argument to propose that the size of the cyclic plastic zone is dependent on $2\sigma_{YS}$ rather than σ_{YS} as for the monotonic plastic zone. In order to reach this result, Rice superposed the result of the plastic zone generated at $K = K_{\max}$ and σ_{YS} with a plastic zone generated by $K = -\Delta K$ and $2\sigma_{YS}$. The yield stress is doubled to ensure that the magnitude and direction of the stresses is correct in the superposition. This is shown schematically in figure 2.4.

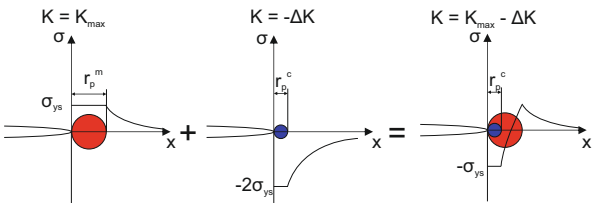

Figure 2.4: Diagram showing superposition of two plastic zone solutions to give the cyclic plastic zone embedded in a larger monotonic plastic zone.

This gives equations for the monotonic and cyclic plastic zones of the form:

$$r_p^m = \alpha^m \left(\frac{K_{\max}}{\sigma_{YS}}\right)^2 \tag{2.14}$$

$$r_p^c = \alpha^c \left(\frac{\Delta K}{\sigma_{YS}}\right)^2 \tag{2.15}$$

where: $\alpha^{m,c}$ are model dependent parameters. For example, the strip yield model from equation (2.9) gives $\alpha^m = \frac{\pi}{8}$. Note that for the Irwin and strip-yield models, which do not include strain hardening effects, $\alpha^c = \frac{\alpha^m}{4}$ to account for the doubled yield stress in the case of the cyclic plastic zone.

The difference in size between the cyclic and monotonic plastic zone is governed purely by the R-ratio. By substituting in $\Delta K = (1-R)K_{\max}$ to equation (2.15) the relationship is given by:

$$\frac{r_p^m}{r_p^c} = \left(\frac{K_{\max}}{\sigma_{YS}}\right)^2 \left(\frac{2\sigma_{YS}}{(1-R)K_{\max}}\right)^2 = \frac{4}{(1-R)^2} \tag{2.16}$$

2.2 Fracture Mechanics Applications

This section discusses the available methods for determining the fracture mechanics quantities of interest in this project, namely stress intensity factor, closure and plastic zone size. The methods have been split into two groups: contact and non-contact. The quantities they are able to measure are discussed and the utility of each method for this project has been evaluated.

2.2.1 Analytical Approach

Generally the stress intensity factor is not a measured quantity, as historically it has been difficult to do so. Numerous analytical solutions exist to calculate it from the applied load and knowledge of specimen geometry. For example, the ASTM E-647 method of measurement of fatigue crack growth rates [20], provides the following formula for calculating ΔK for a compact tension (CT) specimen:

$$\Delta K = \frac{\Delta P}{B\sqrt{W}} \frac{(2+\alpha)}{(1-\alpha)^{3/2}} \left(0.886 + 4.64\alpha - 13.32\alpha^2 + 14.72\alpha^3 - 5.6\alpha^4\right) \tag{2.17}$$

where: $\alpha = \frac{a}{W}$, a is crack length, W is specimen width, ΔP is load amplitude and B is thickness. This expression is only valid for $\alpha > 0.2$.

This kind of equation is useful for calculating a value of ΔK, and provided it is used consistently provide a comparison between different experiments, but clearly does not include allowances for any effects of closure.

Plastic zone size can also of course be obtained analytically using equations (2.14) and (2.15), but due to the assumptions used in the models to create them, these also are not a reliable indicator of the actual size and shape of the plastic zone.

2.2.2 Contact Methods

Hardness Testing

Hardness is a measure of a material's resistance to localised plastic deformation. Hardness is not a fundamental material property as it is strongly influenced by microstructure and other factors related to the processing or history of the material rather than its atomic composition. Therefore, hardness is quoted as a number and reference to the method used to measure it.

Measuring hardness usually is performed by indenting a material with an indenter using a known force and measuring the size of the indent created. These measurements are typically

made *ex-situ* after a fatigue crack has been grown. Different indenter shapes have been used historically, such as a sphere for the Brinell hardness test [21], but for small-scale tests a pyramidal indenter was developed by Smith & Sandland [22] whilst working for Vickers Ltd, which hence became known as the Vickers hardness test. The Vickers indenter is a square-based pyramid with an angle between its faces of 136°. The Vickers hardness number is given by:

$$HV = 0.1891\frac{F}{d^2} \tag{2.18}$$

where: F is the force in Newtons and d is the average length in mm of the diagonals created in the indent.

In metals, hardness is usually increased by plastic deformation, so called work-hardening. Austenitic stainless steels in particular work-harden readily, which makes them difficult to machine [23]. The plastic zone therefore has an increased hardness compared to the surrounding material and a hardness testing method could be used to determine its size and shape. Due to the small size of plastic zones, microhardness testing must be used. This is typically is the same as a Vickers hardness using a pyramidal indenter, but with smaller loads of a few hundred grams rather than kilograms.

The technique appears to have been first used by Bathias & Pelloux [24] to examine the size of plastic zone as a function of ΔK in maraging and austenitic steels. Their work confirmed the presence of the cyclic plastic zone within a monotonic plastic zone. Purcell & Weertman [25] were other early authors who studied the increase in hardness around the fatigue crack tip of copper single crystals. The region of increased hardness was found to be in agreement with a plastic zone they calculated from an unspecified 'fracture mechanics criteria'.

A study by Chalant & Rémy used etching and microhardness to locate the monotonic and cyclic plastic zones. Unlike Bathias & Pelloux they did not observed a plateau in the

microhardness results and found a monotonic plastic zone size that did not agree with the finite element results given by Levy et al [26] that was used as a comparison.

Loye et al [27] found that microhardness could be used to measure the cyclic plastic zone in 316 stainless steel and achieved good agreement with Levy et al [26]. Rather than directly using the hardness, Loye et al [27] correlated the increase in hardness around the plastic zone with an increase in plastic strain and used that value to determine both the size and shape of the cyclic plastic zone.

Guerra-Rosa et al [28] successfully used microhardness measurements to determine the size of the cyclic plastic zone in a ferrite-pearlite steel, but also had difficulty finding the monotonic plastic zone. The authors also provide a comprehensive list of $\alpha^{m,c}$ (equations (2.14) and (2.15)) values from other authors using other measurement techniques, and demonstrate the ability of microhardness testing for determining α^{c} for their material.

The papers discussed above present a complex picture of the use of microhardness to determine monotonic plastic zone size, but are generally in agreement that the size of the cyclic plastic zone can be reliably measured. The repeated cycles of yielding in the cyclic plastic zone work-harden the material more, generating a larger increase in hardness, that is easier to distinguish from the un-hardened material away from the crack tip.

Small scale hardness testing was developed further by the invention of nanoindentation. Nanoindentation relies on a pyramidal indenter, but triangular rather than square-based. The principle of operation also differs, as the hardness is not determined from the measured indent size, but instead from the load-depth curve of the indenter.

An early example of the technology is described by Doerner & Nix [29] for the study of the hardness of thin films. The technique was used in combination with stylus profilometry by Nyström et al [30] to distinguish the monotonic and cyclic plastic zones and measure their sizes in both ferritic and austenitic stainless steels. Nanoindentation successfully located the

cyclic plastic zone in both steel types, but despite the sensitivity and resolution, Nyström et al had to rely on other methods to distinguish the monotonic plastic zone from the rest of the specimen.

Similarly, Yang et al [31] noted an increase in hardness associated with a cyclic plastic zone, but no obvious correlation with the monotonic plastic zone using nanoindentation in 4340 steel in an annealed and quenched condition.

More recently, Tao et al [32] used nanoindentation to measure the hardness in a grid pattern around the crack tip in 304 stainless steel and concluded that the technique has the possibility of determining a non-specific plastic zone size.

It appears that, whilst reducing the scale of hardness testing and increasing the resolution has been able to more clearly resolve cyclic plasticity, the utility of hardness testing for determining the monotonic plastic zone has still not been demonstrated. Clearly, there is a strong effect of material and microstructure on the change in hardness in the cyclic plastic zone and generally a lot of scatter in the measured hardness values, both of which present problems when quantitatively measuring plasticity.

Compliance Techniques

Compliance is the reciprocal of stiffness, and is calculated as:

$$C = \frac{\delta}{F} \tag{2.19}$$

where δ is the deformation and F the applied force.

During a load-controlled test, the deformation of the specimen at different points on its surface must be measured to determine the compliance at those points. Experimentally, this is usually accomplished by either bonding a strain gauge to the specimen or by using an extensometer in contact with the specimen. Elber [17] demonstrated using an extensometer that compliance behind the crack tip changes when closure occurs and can therefore be used

as an indication of closure.

Strain gauges are electrical sensors that are bonded to a specimen and change in resistance with changing strain. Kikukawa et al [33] proposed a method for bonding a strain gauge to the back face of a compact tension specimen to measure compliance during a fatigue crack growth test. The output of the strain gauge gives a load-displacement curve that has a characteristic hockey stick or 'L' shape, when closure occurs. By determining the load at which the compliance deviates from linear behaviour, the onset of closure can be found.

This method was used by de Matos & Nowell [34], who also used a extensometer to measure crack mouth opening and digital image correlation (DIC) to compare the ability of each to determine closure. The focus of the work was on the effect of specimen thickness on closure effects, and it was concluded the back face strain gauge was the most suitable method for determining closure as the surface measurements from DIC began to differ from the bulk measurement of the back face gauge in thicker specimens.

Pacey et al [35] used compliance methods in combination with full-field analysis using photoelasticity, discussed in more detail later. The authors concluded that the photoelastic data was an improvement on compliance as it allowed direct measurement of the effective stress intensity factor and crack face contact force. Diaz et al [36] demonstrated the ability of thermoelastic stress analysis, another full field technique to provide closure information that compared favourably with results obtained from a back face strain gauge.

Compliance based methods were useful for early investigations into closure; however, the information that can be obtained from full-field methods eclipses that gained from compliance measurements during testing and has obviated their use.

Acoustic Emission

Acoustic emission (AE) techniques use transducers bonded to the specimen to detect elastic waves. The sources of these waves are due to local deformation events or crack growth. The data obtained can be analysed in a number of ways, such as the count of waves or the rise time of a wave. These are then correlated to fatigue crack parameters, usually with the intention of determining remaining life or the transition to unstable crack growth.

Chai et al [37] used a derived measure they called AE entropy to create a probabilistic model for predicting remaining fatigue life of a 316LN CT specimen. The data presented shows extensive noise and no strong correlation between AE entropy and crack length. Despite this, Chai et al conclude that the cumulative entropy can be used as a method to detect the transition between crack initiation behaviour and stage II crack growth.

Bhuiyan & Giurgiutiu [38] also demonstrated the noise related issues with AE methods. The authors tested a cracked plate and tried to remove noise sources by applying clay to the outer edges of the specimen to absorb acoustic waves and reduce the reflection of the waves from the specimen boundary. AE events were correlated to the loading of the specimen in most cases, but not reliably. Even with the physical damping provided by the clay, a de-noising procedure had to be applied to the data from the transducers. Ultimately Bhuiyan & Giurgiutiu conclude that AE hit-based analyses do not capture all the phenomena involved with fatigue cracking, and that grouping waveforms by similarity of frequency spectrum may be a better methodology.

AE methods are unsuitable for the measurements required in this project. The methodology appears particularly sensitive to noise and there is significant difficulty in interpreting any results obtained and how they relate to fatigue processes.

2.2.3 Non-Contact Methods

Photoelasticity

Photoelasticity is a full-field optical technique that takes advantage of the birefringence phenomenon of certain transparent materials and the change of the birefringence with applied stress. Typically, the specimen used is a transparent polymer, in so-called transmission photoelasticity. A birefringent reflective coating can be applied to opaque specimens for reflective photoelasticity. The method works by illuminating a stressed material with a polarised light source and measuring the isochromatic fringe pattern generated. An equation known as the stress-optic law can be used to determine the difference in principal stresses:

$$\sigma_1 - \sigma_2 = \frac{NF_\sigma}{h} \tag{2.20}$$

$$F_\sigma = \frac{\lambda}{C} \tag{2.21}$$

where: N is the fringe number, h is material thickness, λ is wavelength of the light used and C is the relative stress-optic coefficient.

Irwin [39] first proposed that photoelasticity could be used to obtain the stress intensity factor by evaluating the stress at a point on the apogee of a fringe, where the shear stress is constant with respect to the polar coordinate θ and the stress equations become tractable.

Sanford & Dally [40] developed the technique further by introducing an multi-point overdeterministic methodology (MPODM) to determine mixed-mode stress intensity factors K_I, K_{II} and the opening load σ_{op} from photoelastic data. The shape of fringes can be determined by an equation of the form:

$$\frac{NF_\sigma}{h} = f(r, \theta, K_I, K_{II}) \tag{2.22}$$

where: r, θ are the polar coordinates of points along the fringe.

Equation (2.22) is under-determined as it has an equal number of known quantities (r, θ) that can be measured and unknown quantities (K_I, K_{II}) that need to be determined.

Sanford & Dally's MPODM addresses this issue by measuring multiple points along the isochromatic fringes, creating a version of equation (2.22) at each point and then performing a least-squares minimisation on these to determine K_I, K_{II} and σ_{op}.

A key finding by James et al [41] was that photoelasticity could 'see' the effects of crack closure. Using the technique, the authors were able to link plasticity-induced closure with changes to the crack tip stress field and changes to ΔK_{eff}. This work was expanded upon by Pacey et al [35] who used a Muskhelishvilli-type stress distribution, which allows a non-uniform passing stress in the vicinity the crack tip, unlike the Westergaard distribution used by Sanford & Daly. The authors demonstrated that the stress intensity factors could readily be obtained and there was clear evidence of closure that could be seen in the photoelastic data.

Digital photoelastic data using phase-stepping to obtain accurate fringe information was used by Christopher et al [42], with a similar MPODM as Pacey et al [35], to investigate plasticity-induced shielding. The 'CJP' model was developed to understand the effect of plasticity on crack growth retardation and the effect on the elastic stress field.

The utility of photoelasticity to measure ΔK_{eff} has been demonstrated extensively since the inception of the technique and more recently, the effects of closure have been observed. There would however be some difficulty in applying the technique to the small geometry metallic specimens, which would require the application of a birefringent coating and high magnification lens to observe any fringes.

Moiré Interferometry

Moiré is an optical technique for measuring in-plane strain, by creating contour maps of in-plane displacements. The technique works by applying or etching a grid to the surface of the specimen that will deform with the specimen, then analysing this through a master grid,

i.e. an undeformed grid of the same specification. This generates Moiré fringes, which are contours of constant displacement in the direction perpendicular to that of the grid. Moiré interferometry replaces the physical master grid with a virtual grid created by the intersection of two coherent laser beams [43]. The contour interval of the fringes is proportional to the size of the master grating pitch and therefore the relative displacement between two points can be calculated by counting the number of fringes between the points and multiplying by the pitch.

As a fracture mechanics technique, McDonach et al [44] demonstrated the ability to measure crack opening displacements, by aligning a Moiré grating such that displacements perpendicular to the crack were measured.

Nicoletto [45] used Moiré interferometry to measure the size of both monotonic and cyclic plastic zones in 7075-T6 aluminium. Monotonic plasticity was identified using a strain threshold method and cyclic plasticity appeared as a kink in the Moiré fringes.

Work by Smith et al [46] attempted to use Moiré to determine stress intensity factors through the thickness to verify photoelastic results with some success. The stress intensity was calculated using the following equation applied along the line $\theta = \frac{\pi}{2}$:

$$K_{AP} = \frac{2\sqrt{\pi}}{\sqrt{r}} \frac{E}{(3-\nu)} N_x p \tag{2.23}$$

where: K_{AP} is the apparent stress intensity factor, which is equivalent to K_I in the singularity dominated zone, E is the elastic modulus, ν is Poisson's ratio, N_x is the fringe order and p the pitch of the grating used. This equation was used by Gray et al [47] during their investigation of crack closure using Moiré. Gray et al also demonstrated that the fringe pattern was sensitive to closure effects, with changes occurring due to crack flank contact, and that crack opening occurs over a wider range of stress intensities than previously thought.

From the literature, Moiré seems to be a powerful technique for measuring stress intensity and potentially observing plasticity and closure. However, a review by Patterson & Olden

[48] that compared multiple optical methods for measuring crack tip stress fields highlights some of the difficulties in employing Moiré. Bonding a suitable grating to the specimen and the skill required to perform observations compared to the other techniques make Moiré unfavourable.

Caustics

The method of caustics, also known as the shadow spot method, is an optical technique for measuring the stress intensity factor of a cracked specimen. The stress distribution at the crack tip causes the material to contract out-of-plane due to the Poisson effect, with more contraction at higher stresses. This changes the planar specimen surface into a lens-like arrangement. When illuminated by a light point source, such as a laser, the reflected image on a plane at a distance z_0 from the specimen surface will have a dark spot surrounding the crack tip region surrounded by a ring of high intensity light, the caustic. The radius r_0 of the shadow spot is related to the mode I stress intensity factor by the following relationship:

$$K_I \propto \frac{E r_0^{5/2}}{\nu z_0} \tag{2.24}$$

where: E is the elastic modulus and ν is Poisson's ratio.

Rosakis & Freund [49] investigated the possibility of using caustics to measure the J-integral, analogous to K for Elastic Plastic Fracture Mechanics, within the plastic zone of a ductile steel. By changing the distance of the measurement plane z_0 they were able to generate caustics from inside or outside the plastic zone, described by the ratio r_0/r_p, the size of the caustic, r_0, to plastic zone, r_p,. Inside the plastic zone, the caustic shape changes from circular to more 'D' shaped and the relationship for K_I is no longer valid. Further work by Rosakis et al [50] demonstrated that reliable K_I measurements were possible for $r_0 > 1.5 r_p$ and below this value there was an influence of plasticity on the results.

The method of caustics also has utility for the determination of closure, as demonstrated

by Bull & Hermann [51]. The authors compared the diameter of the caustic generated during the unloading between $K_{\max}$ and $K_{\min}$ of one cycle during a fatigue crack growth test. The results of this procedure were compared to the back-face strain gauge method (see 2.2.2) and it was found that the caustic diameter underwent a similar behaviour, with a change in gradient below the load at which closure occurred.

Tomlinson & Patterson [52] investigated the effects of residual stress and closure on the caustic generated by fatigue cracks in high strength steel EN24. The theoretical and experimental stress intensity factors were measured at a number of points during a fatigue crack growth test. The authors found the the experimental stress intensity factors were offset to a higher value than the theoretical values and the offset was equal to the residual stress determined by measuring the caustic at zero load. By measuring the residual caustic, closure could be quantified without having to perform the load-reducing method used by Bull & Hermann [51].

The method of caustics has the advantage of being able to measure an effective stress intensity factor and able to determine the effects of closure. However, measurement of the plastic zone size is not possible using caustics.

X-Ray Diffraction

X-ray diffraction is a technique that can determine residual stress and dislocation density of a crystalline material by analysing the diffraction patterns produced by illuminating regions of the specimen with monochromatic X-rays. In a polycrystalline material with random grain orientation the crystal planes of the material diffract the incident X-rays, forming a ring in the detector.

An X-ray microbeam technique was initially developed by Hirsch & Kellar [53] to determine the effects of rolling on aluminium. By reducing the volume of material illuminated by

the X-rays, the diffraction ring turns into a series of spots. The number of spots determines the mean size of the grains and the distortion of the spots depends on the deformation of the grains. It was found that the initial 'spotty' rings form into arcs after deformation by rolling.

Shuji & Keisuke [54] used this technique to determine the excess dislocation density, from the diffraction arc widths, and the sub-grain size from the number of spots in each arc. Excess dislocations are arise from plastic work in excess of the geometrically necessary dislocations, which are required dislocations for the grains in the material to be compatible at the grain boundaries. These parameters correlated with the fatigue crack propagation rate da/dn, indicating the effect of microstructure on fatigue crack growth behaviour. Excess dislocation density was calibrated with true strain to allow the strain around the crack tip to be measured. From these measurements, the residual stress from the crack tip was measured and found to have a similar shape to that predicted by Rice [9], but was much smaller.

Historically, the strains measured by X-ray diffraction techniques were confined to near-surface, however more recently, the development of large synchrotons such as the Diamond Light Source have allowed the use of high energy X-rays to perform measurements deeper into specimens. Withers [55] provides a thorough review of the techniques available for fracture mechanics studies using synchrotron X-rays.

X-ray diffraction techniques are capable of identifying the plastic zone and mapping strains, which can then be converted into stresses via the elastic modulus and thereby obtain ΔK. Current technology allows the collection of this information *ex-situ*, although some authors have performed *in-situ* measurements for crack formation due to step-wise loading [56]. A further difficulty is the deficit of available beam time on high-energy X-ray sources that limit the number of specimens that could be tested.

Digital Image Correlation

Digital Image Correlation (DIC) is an optical technique for measuring full-field surface displacements. DIC can be performed by a single camera to measure in-plane displacements (2-D DIC) or by two cameras arranged stereoscopically to also measure out-of-plane displacements (3-D DIC). The technique requires the specimen surface to have a high-contrast random pattern that deforms with the specimen, typically this is in the form of an applied coating of black speckles on a white background or vice-versa. Deformed images are compared to a reference image by breaking the image into subsets and determining the relative motion of each subset between the images. Strains can be calculated from the displacement maps, and then converted to stress using a knowledge of the elastic modulus.

DIC was successfully used by Lopez-Crespo et al [57] to measure ΔK_{eff} and they demonstrated that the technique is sensitive to the effects of plasticity in Al 7010 T7651 alloy, but did not measure the plastic zone size directly. Loading at increasing R-ratios from $0 - 0.4$ was found to increase ΔK_{eff} from a low value to the nominal ΔK value demonstrating that the technique was sensitive to the effects of closure also.

Direct measurements of plastic zone size are possible using DIC, for example Zhang & Liu [58] utilised the DIC technique on microscope images of a crack captured during loading and unloading and determined the plastic zone size by determining when the strain exceeded yield using the Von-Mises strain criterion. Using this technique the authors were able to measure both the monotonic and cyclic plastic zones and achieved reasonable agreement with theory when closure was accounted for. A similar methodology was used by Vasco-Olmo et al [59] to measure the plastic zone size in commercially pure titanium.

DIC is a powerful technique for obtaining full-field displacements and is capable of measuring ΔK_{eff} and the effects of closure. Plastic zone size measurements can also be obtained, provided that the yield stress is known.

Thermoelastic Stress Analysis

Thermoelastic Stress Analysis (TSA) is a non-contact full-field technique for measuring surface stresses in dynamically loaded objects. The technique is based on the principle of the thermoelastic effect, first proposed by Lord Kelvin [60], whereby a volumetric change in a material causes a change in its temperature. TSA uses an infrared camera locked-in to a reference signal to measure the temperature changes that occur in sync with the specimen loading.

Provided there is no conduction through the specimen and the deformations remain elastic, the temperature change due to the thermoelastic effect can be expressed as [61]:

$$\Delta T = \frac{-\alpha T}{\rho C_p} \Delta \left(\sigma_1 + \sigma_2 \right) \tag{2.25}$$

where: T is absolute temperature, α is the coefficient of thermal expansion, ρ is the density, C_p is the specific heat at constant pressure and $\sigma_{1,2}$ are the principal stresses. Including detector related constants, the simplest form of the TSA relationship is given as [62]:

$$AS = \Delta \left(\sigma_1 + \sigma_2 \right) \tag{2.26}$$

where: A is a calibration constant and S is the detector signal.

In order to obtain high-quality data, the specimen surface must have a uniform and high emissivity in the infrared spectrum. Typically, this is achieved by applying a coating with these properties, such as matte black paint or graphite powder.

The data obtained from a TSA system is in the form of a vector, with magnitude S and phase angle θ between the loading signal and the temperature response.

Early TSA systems, such as SPATE, were single infrared detectors that used a mirror to permit a raster scan over a specimen. However, more recently staring array cameras have been developed that can capture full-field images without rastering. A SPATE system was used by Stanley and Dulieu-Smith [63] to demonstrate that ΔK_I and ΔK_{II} could be

obtained from the plot of the inverse of the squared maximum signal $1/S_{\max}^2$ against the vertical distance from the crack plane y.

Following the development of staring array cameras, Diaz et al [64] fitted the Muskhelishvili-type stress distribution, first employed by Nurse & Patterson [65] for photoelastic data, to obtain mixed-mode stress intensity data for cracked single-edge notched specimens. Diaz et al also noted that the phase data potentially contained information related to crack tip plasticity as it indicated a breakdown in the adiabatic/elastic assumption. Further work by Diaz et al [66] developed a multipoint-over-deterministic technique based on the Muskhelishvili-type stress distribution and demonstrated that it was measuring the effective stress intensity factor and was sensitive to closure effects measured by compliance techniques.

Patki & Patterson [67] explored the phase data and found that the size of region of inverted phase near the crack tip behaved like the cyclic crack tip plastic zone and was affected by overloads. More recent work by Palumbo et al [68] and Sakagami et al [69] suggest that the second harmonic of the thermoelastic signal might be more suitable for measuring plastic effects.

TSA has been demonstrated to be able to measure ΔK_{eff} and the effects of closure and can simultaneously measure cyclic plastic zone size. No prior knowledge of the elastic modulus or yield stress is required to determine the crack-tip stress state. Measurements must be collected during loading, as static TSA is not possible.

2.2.4 Comparison

From the above review of techniques, the most suitable methodology to use is TSA as it has the potential for simultaneous measurement of $\Delta K_{\text{eff}}$and plastic zone size. TSA does not require knowledge of Young's modulus to measure the surface stresses, provided the system is calibrated with a specimen manufactured from the same material. TSA can also

measure plasticity without knowledge of the yield stress, which is of particular use as the yield stress will be increased by an unknown amount by the radiation damage.

Table 2.1: Comparison of the reviewed techniques, showing the available measurement quantities, advantages and disadvantages of each technique.

Technique	ΔK	r_p	Closure	In-Situ	Advantages	Disadvantages
Hardness	×	✓	×	×	High resolution with nano-indentation	Noisy, microstructure sensitive
Compliance	×	×	×	✓	Simple to utilise	Noisy, point-based
Acoustic Emission	×	×	×	✓		Limited understanding of sources
Photoelastic	✓	✓	×	✓	Accurate	Small geometry difficult
Moiré	✓	✓	×	✓		Grating difficult to apply
Caustics	✓	✓	×	✓		Small geometry difficult
X-Ray Diffraction	✓	✓	✓	✓	Sub-surface data possible	Beam time availability
DIC	✓	✓	✓	✓	Full-field strain data	Stress needs E knowledge
TSA	✓	✓	✓	✓	No prior material knowledge	Fast loading frequency

2.3 Radiation Damage

Radiation, broadly, is the transmission of energetic particles. The type of particle can vary, for example: photons, electrons, protons, neutrons or light nuclei. Radiation damage is caused when these energetic particles interact with matter, typically causing a change to the microstructure of the target material. This section will focus on the effects of energetic protons and neutrons incident on metals, with a focus on austenitic steels.

2.3.1 Damage Cascades

Radiation damage is caused by the transfer of energy between an incident particle and the atoms in a target material. If the incident particle has enough energy, it will displace an atom from its lattice site in the material, creating a primary knock-on atom (PKA). This PKA can itself travel through the lattice and create further knock on atoms, forming a damage cascade. Eventually the PKA energy will drop below the binding energy of the lattice and no further knock ons will occur and the PKA will remain as an interstitial atom. The result of the damage cascade process is the creation of material defects, such as Frenkel pairs composed of Schottky and Frenkel defects (vacancies and interstitials).

The length scale of the damage cascade produced is dependent on the incident particle. At the two extremes are direct impact damage and defect accumulation [70]. In the direct impact case, the damage is localised and affects a large number of atoms. In the damage accumulation case, the damage occurs over a longer length but affects a smaller volume of atoms in total. High mass recoiling atoms such as those produced during fission or alpha decay cause direct impact damage, whereas high energy, low mass particles such as protons, neutrons and alpha particles cause defect accumulation.

The defects generated by the damage cascade are not immutable, i.e. there will be an element of recovery due the the migration of the defects through the lattice. Higher

temperatures promote greater recovery as vacancies and interstitials are more mobile.

2.3.2 Reactor Neutrons

Neutrons are uncharged particles that are produced during fission reactions in the reactor core. The neutrons are produced over a range of energies from fractions of an eV to MeV[71][72]. Neutrons are electrically neutral and can therefore only interact with the atoms in the target via collisions with nuclei. This results in damage cascades that are dispersed over a relatively long length scale, as each collision with an atomic nucleus only takes a fraction of the energy from the neutron.

2.3.3 Accelerated Ions

Accelerated ions are energetic charged particles that can be used to generate radiation damage in specimens. The charge means that the interactions between the incident particles and the target are both nuclear and electrical and therefore not completely analogous to neutron interactions. The dominant form of energy loss for the charge particles is due to interactions with the electrons in the target material, so-called electronic interactions, analogous with drag in aerodynamics. Below a certain energy, dependent on the incident particle and target material, collisions with the atomic nuclei become more likely. This results in a region of high damage, called the Bragg peak, where the remaining particle energy is deposited. Beyond the Bragg peak there is no further radiation damage, this limits the range of charge particles in matter.

Ions are accelerated to high energy levels in a particle accelerator, such as the linear tandem pelletron at the Dalton Cumbrian Facility (DCF) [73]. Particle accelerators generate a monoenergetic beam of ions that typically must be rastered over a specimen to generate an area of damage.

2.3.4 Effects of Radiation Damage on Austenitic Stainless Steels

Embrittlement & Hardening

Under irradiation, the mechanical properties of the steel will be altered. In general, the strength will increase and elongation will decrease, resulting in an increase in hardness. This is due to the introduction of radiation induced defects, such as: interstitials, vacancies, voids and precipitates, which act to prevent dislocation motion[74].

The increase in hardness caused by radiation is known to plateau at some damage level and not increase further. This is due to the generation of dislocations and their recovery reaching a steady-state value [75]. This steady state value is dependent on irradiation temperature and dose rate of the radiation damage. Recent work by Jin et al [76], using proton irradiation at 360°C and a dose rate of $5E-6$dpa/s in austenitic stainless steel, found that the radiation hardening effect saturated at 2.5dpa. This value differs from the neutron damage data reviewed by Zinkle et al [75], who found that damage levels of 10dpa or more were needed for dislocation density to saturate at 400°C. Jin et al ascribe this difference to the damage rate, which is an order of magnitude higher or more for the proton irradiations than neutron irradiations.

Segregation and Stress Corrosion Cracking

Elemental segregation during irradiation was first observed by Okamoto & Wiedersich [77] in an austenitic stainless steel. The authors observed that, under 3.25MeV Ni^{+} irradiation at 650°C, alloying elements would diffuse towards or away from the bombarded surface depending on their size relative to the bulk element of the alloy. For example, undersized elements such as nickel and silicon become enriched at the surface, whilst oversized elements like chromium became depleted.

A later paper by Marwick [78] introduced the concept of the inverse Kirkendall effect

to help explain the segregation of alloying elements at higher concentrations that are not appreciably different in size to the average size of elements in the alloy. Kirkendall et al [79] first observed that the diffusion of the component elements of an alloy could not be described by a single parameter and instead each had their own diffusion constant. This finding meant that diffusion was mediated by the presence of vacancies and not by the swapping of atoms on adjacent lattice sites. The inverse Kirkendall effect, as described by Marwick, is caused by the introduction of a vacancy gradient due to the radiation damage. Nickel is enriched at the surface and chromium depleted due to the faster diffusion of nickel through the lattice.

Stress corrosion cracking (SCC) is the growth of cracks due to the simultaneous presence of a corrosive environment and stress [80]. Austenitic stainless steels are usually highly corrosion resistant due to their high chromium content, which causes the formation of a passivation layer on the surface of the metal, preventing corrosion of the bulk. However, if the passivation layer is disturbed or removed, a process known as sensitization, corrosion can occur. Radiation induced segregation, discussed above, can sensitize the steel by depleting the chromium near the surface and grain boundaries. This leaves the steel vulnerable to SCC, so called irradiation assisted stress corrosion cracking. IASCC is more common in boiling water reactors than pressurized water reactors due to the chemistry of the coolant water under radiolytic decomposition [81].

Transmutation & Activation

Transmutation reactions occur when the incident energetic particle is captured by the nucleus of an atom causing a change in the atomic mass or number of the target atom. Transmutation can occur for both neutron and proton irradiation and often results in an unstable atom that subsequently decays, resulting in a activated target.

Stainless steels are relatively resistant to transmutation under most fission neutron spec-

tra [82] compared to other metals. However, some components of the alloys are sensitive to transmutation, in particular manganese will readily transmute under the reaction $\mathrm{Mn}^{55}(n,\gamma)\mathrm{Mn}^{56}$, which decays to Fe^{56}. This causes problems as Mn forms MnS precipitates in the material, which help by preventing sulphur impurities present in the alloy from migrating. Under irradiation the manganese transmutes to iron, releasing the sulphur to migrate to grain boundaries and increase IASCC susceptibility [83].

In addition to changing alloy composition, transmutation reactions are a source of hydrogen and helium, that can cause embrittlement and bubble formation.

Swelling

Swelling is the volumetric change of a material when subject to irradiation damage. There are three mechanisms that cause swelling [70]: vacancy and interstitial formation, decreased density due to disorder and gas bubble formation.

Austenitic stainless steels are particularly sensitive to swelling due to their face centred cubic crystal structure. In ferritic steels with a body centred cubic structure, swelling typically saturates at around a 5% increase in volume, whereas austenitic steels have not been observed to saturate, and volume increases of 80% have been observed in 316 under neutron irradiation [82].

Swelling is known to be particularly sensitive to the presence of helium. Helium is produced by alpha decay of transmuted elements during neutron irradiation and is insoluble in metals so will form gas bubbles in cavities. This acts to stabilise the cavities and change the behaviour of the metal being irradiated. Helium changes the relative sink strengths, altering the vacancy and interstitial diffusion behaviour. This alters the radiation induced segregation and precipitation behaviour of solute atoms, resulting in increased swelling [84]. During proton irradiation helium formation is not expected, so will not be able to alter the

swelling behaviour.

Recent work by Malaplate et al [85] suggests that swelling in 304 stainless steel is not particularly severe, even at high doses, using heavy ion irradiations at 450°C. This temperature was chosen to approximate low rate neutron damage in a PWR. Limited swelling was noted at 5dpa, above the damage level expected in this work.

2.3.5 Protons as a Surrogate for Neutrons

Achieving high levels of damage, such as found at the end-of-life in in-core components, with neutrons is difficult. Irradiations take a long time to reach high damage levels and specimens become highly active in the process, resulting in high costs for post-irradiation handling [86]. Ion beams were proposed as a remedy to this, as they are capable of significantly higher damage rates and result in less active specimens.

However, as outlined above, neutrons and accelerated ions interact differently when travelling through matter, which must be accounted for when using protons as a neutron surrogate. Mansur [87] developed a theoretical basis to account for the differences in particle type on the effects of swelling due to irradiation, proposing a method whereby the irradiation parameters are varied to achieve a similar end state. Mansur focussed on the effect of the recombination of voids and interstitials and suggested that the irradiation temperature for ion irradiations must be increased to account for the increase in dose rate.

A thorough experimental study by Was et al [86] compared neutron irradiations at 275°C to 3.2MeV proton irradiations at 360°C, investigating a number of effects such as grain boundary segregation, stress corrosion cracking, microstructure and hardness. It was found that there is good agreement in these features between the two types of irradiation up to 5dpa.

2.4 Fatigue Crack Growth & Radiation Damage

The study of the combined effects of irradiation damage and fatigue has been of interest for a number of years. Early work on the effects of radiation damage to fatigue crack propagation was performed on specimens irradiated by neutrons using either a low energy thermal spectrum, such as found in PWRs, or a higher energy fast spectrum.

A comprehensive review by James [88] summarises the results of a number of such studies into the effect of neutron irradiation on austenitic stainless steels. No consistent effect of neutron irradiation was found with studies reporting no change in crack growth rate, an increase in crack growth rate and a decrease in crack growth rate with neutron damage. Factors such as irradiation temperature, test temperature, prior cold work, and stress intensity factor range were found to influence the effect of the irradiations.

Following the work of Mansur [87] proton irradiation has been used as a surrogate for neutrons in fatigue crack growth investigations. Weertman & Green [89] proposed a theoretical basis for the fatigue crack growth rate to decrease during such an in-situ experiment for materials that harden during radiation damage. Fenici & Suolang [90] demonstrated this behaviour in thin-gauge (0.15mm) specimens manufactured from stainless steel containing an edge notch . In-situ proton irradiations at 300°C caused an increase in the time taken for a fatigue crack to initiate and a decrease in crack growth rate. Rickerby & Fenici [91] had previously demonstrated the validity of thin-gauge specimens for crack growth rate studies. Later work by Murase et al [92] on similar specimens showed the same in-situ behaviour, with an extension of fatigue life by up to $2.5\times$. It was also noted that post-irradiation testing showed a larger growth rate reduction.

2.5 Knowledge Gaps

The use of proton irradiation as a surrogate for neutron irradiation has been firmly established in the literature in microstructural studies. However, there has been relatively few studies investigating the effects of the proton irradiation of laboratory scale structures. The few studies that report on the effects of proton irradiation, present results for a small number of specimens, understandable with the difficulties obtaining beam time. However, fatigue crack growth is often enormously variable with variations of up to a factor of two between nominally identical specimens. Hence, a larger number of specimens need to be tested to obtain statistically meaningful information.

Many fatigue crack growth studies have measured only the crack length and used the analytical relationship provided by the ASTM to calculate ΔK and then calculate a theoretical plastic zone size. This approach can miss some of the more subtle effects such as closure that may effect results. Additionally, plastic zone size, when it has been investigated, has often been measured by ex-situ techniques or techniques which require the interruption of the test, which could have introduced uncertainties.

The authors of the studies into the effect of radiation on fatigue crack propagation have suggested that the change in growth behaviour is generally due to change in the hardness caused by the radiation damage. This should manifest as a change in the crack tip plastic zone size. Currently, there appears to have been no studies on the effect of irradiation on the plastic zone size after irradiation.

This work aims to investigate the effects of proton irradiation on a significant sample of specimens, prepared and irradiated in nominally the same way, to increase the statistical power of any conclusions. In addition, the effective stress intensity factor and crack tip plastic zone size will be measured regularly during the fatigue crack growth test, without interruption of the test. This will allow conclusions to be drawn about the effect of radiation

damage on the fatigue crack growth behaviour, the crack-tip stress state, and development of the plastic zone during crack growth in irradiated material.

Chapter 3

Experimental Methods

This chapter details the materials, techniques and methods used in this project. An overview of the specimen material composition, manufacture and preparation is provided, followed by a description of the experimental TSA setup employed. A detailed description of the accelerator and target stage used for irradiation damage is given, in addition to the operational procedures and challenges the setup presented. The use of microhardness testing to determine the location of the radiation damage on the specimens is introduced, followed by the improvements and modifications made to the fatigue crack growth testing setup.

3.1 Specimen Material & Preparation

3.1.1 Material

The material used in this project was 304 stainless steel, an austenitic stainless steel, used in the nuclear industry for in-core support structures and external plant pipe work. As an austenitic steel it has a high ductility, maintains strength at high temperatures and is corrosion resistant. The elemental composition of the 304 alloy used is given in table 3.1.

Table 3.1: Elemental composition of the 304 stainless steel used, provided by Rolls-Royce.

Element	Cr	Ni	Mn	Si	Mo	Cu	C	P	S	Fe
Wt%	18.38	8.09	1.82	0.46	0.27	0.19	0.03	0.018	0.003	Base

Table 3.2: Mechanical and thermal properties of the 304 stainless steel used. Young's modulus and yield strength were measured by performing a tensile test using a dogbone specimen.

Property	Value	Source
Young's Modulus	189GPa	Measured
$\sigma_{\mathrm{YS}(0.2\%)}$	225MPa	Measured
α	17.3×10^{-6}°C^{-1}	ASM MatWeb

The steel was supplied by Rolls-Royce in the form of 5mm thick plates, from which compact tension (CT) specimens were cut using electric discharge machining (EDM). The specimens are of a similar design to ASTM E647 [20], but of a reduced thickness in order to be better accommodated in the irradiation stage, as shown in figure 3.1.

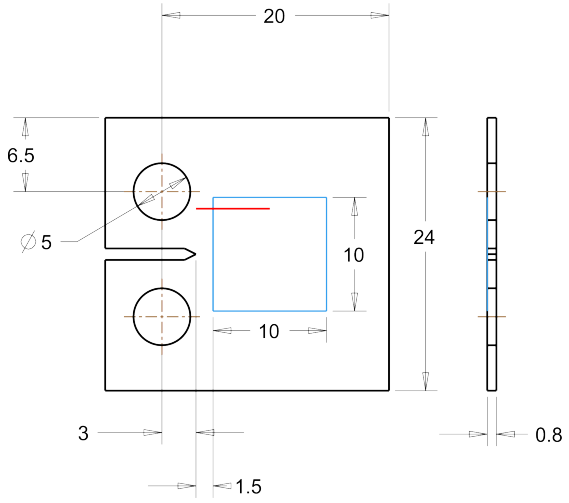

Figure 3.1: Compact tension specimen geometry, in mm. Dashed blue lines indicate the planned irradiation area. The red line shows the typical location where a hardness profile is collected.

3.1.2 Polishing

As the radiation damage will only be a shallow level of damage, it is important that the surface is ground and polished to remove any defects introduced by the machining.

Due to the size of the specimens it was necessary to mount them to a puck with a wax to polish them correctly. The initial puck used was brass and excessively heavy, causing difficulty with fine hand control and snagging on the polishing wheels. A redesigned puck was produced from aluminium to rectify these issues.

After mounting on the pucks, using a hot plate to melt the wax, the specimens were ground by hand on increasingly fine grit papers, from 300 to 600, 800, 1200 and finally 2400. The specimens were then transferred to an automated polishing machine and polished for one hour with one micron alumina. Final polishing was performed on a second automated polisher using 40nm aqueous silica at 50% concentration for one hour.

Specimens were unmounted from the pucks by heating on a hot plate. Wax residue was removed by submerging the specimens in hot 10% concentration sodium carbonate solution and placing in a ultrasonic bath for 30 minutes.

For specimens to be irradiated, two crosses were scribed onto the surface to indicate the two corners of the planned irradiation region closest to the notch. This allowed alignment of the beam position to be more easily performed during the setup of the irradiation experiments.

3.1.3 High Emissivity Coating

As discussed in the section 2.2.3 of the literature review, the TSA technique requires the imaged surface to have a uniform and high emissivity in the infrared spectrum. Any coating used for this must be thin enough to transmit the heat of the specimen underneath and not so thick as to generate its own thermoelastic effect [93].

Initial experiments were attempted to perform TSA with only the bare polished surface, with no success. Most previous TSA studies used matt black paint, applied using a spray can, to coat the specimens as it fulfils the above criteria. Early experiments were conducted with such a paint, with reasonable success in TSA imaging, but there was some difficulty removing the paint after testing to perform microscope investigations. After a second batch of paint was received it was found that there was a change in the composition of the paint, reducing its infrared emissivity and necessitating a change in coating.

A series of experiments with other paints and coatings was performed, using other spray paint types and, upon recommendation from the infrared camera manufacturer, candle soot. It was found that none of the paint-based coatings performed as well as the original paint formulation, and also not as well as soot. Candle soot was difficult to apply and often formed an irregular surface coating, but its infrared performance was significantly better than paint. Following this result, a graphite based spray (Graphit33) was tested. Like the soot, it had superior infrared emissivity and, like the paint, was easy to apply because it was supplied in a spray can. Unlike the paint, the graphite could be also easily removed, making it the best coating choice for all subsequent work.

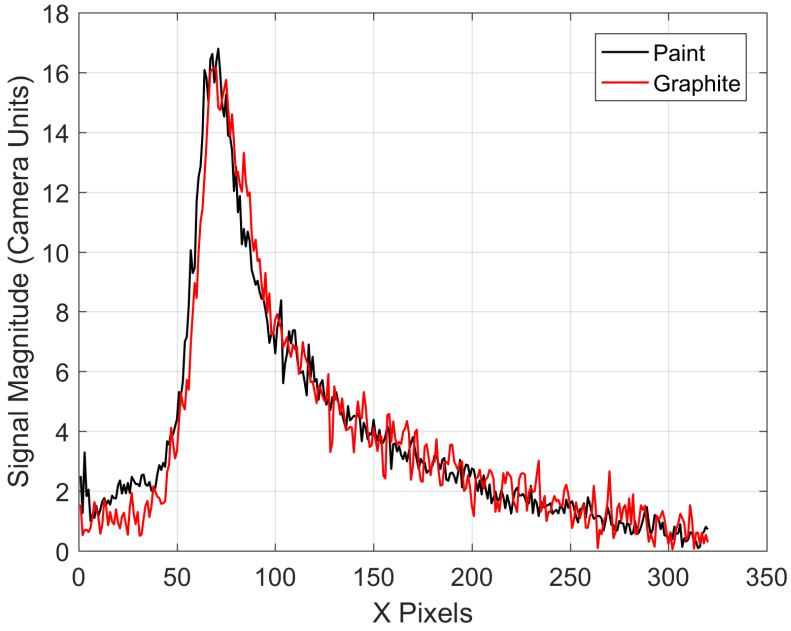

*Figure 3.2: In-phase TSA signal magnitude along a horizontal line from the notch through the crack tip, for a specimen coated with PlastiKote Matt black paint (*Motip Dupli B.V.*, Netherlands) (black) and a specimen coated with Graphit 33 spray (*Kontakt Chemie, Germany*) (red). Both specimens had an approximately* 5*mm crack, with the crack tip located at pixel 65. The difference in signal along this profile is less than* 1%.

3.1.4 Precracking

The final stage of specimen preparation was to generate a fatigue precrack. This ensures that the fatigue crack growth test will start from a sharp crack and away from any influence of machining damage in the notch region. ASTM E647 [20] dictates that a precrack of 1mm from the notch is required, for a total crack length of $a = 4$mm. To generate the crack, the initial load amplitude and mean used were higher than the main test values. The mean and amplitude were gradually decreased as the crack grew, during which the R-ratio was kept constant. The final load levels were equal to that used during the main test. The details of each load step is provided in table 3.3.

A program was created using WaveMatrix (*Instron, Norwood, MA, USA*) to control the

tensile test machine during precracking. The following load steps were used:

Table 3.3: Load dropping procedure used to precrack specimens. During the steps, the R-ratio is maintained at 0.5. The size of the drops is in agreement with ASTM E-647 [20] and the final load step is equal to the test conditions.

P_{mean}	P_{amp}	No. of Cycles
600	200	$30,000$
570	190	$30,000$
540	180	$30,000$
510	170	$30,000$
480	160	$30,000$
450	150	$30,000$

The crack length was monitored using the TSA system during this procedure. Due to the statistical nature of crack initiation, the precrack was not sufficiently long after the load dropping procedure in some cases. An extension of as many cycles necessary at the testing load of $P = 450 \pm 150$N was used until the precrack was 1mm long.

The precracking was observed by the TSA system, necessitating the coating of specimens with graphite, which had to be removed prior to irradiation.

3.2 Thermoelastic Stress Analysis

Thermoelastic stress analysis (TSA) is a non-contact infrared technique that measures full-field surface stress on dynamically loaded objects, as discussed in section 2.2.3 of the literature review.

In the simplest case, the thermal signal generated by an object under a cyclic stress is given by:

$$AS = \Delta\left(\sigma_1 + \sigma_2\right) \tag{3.1}$$

where A is a calibration constant, S is the detector signal, and $\sigma_{1,2}$ are the principal stresses.

TSA uses a sensitive infrared detector to measure the temperature changes associated with the changing stress, which are typically several mK in magnitude.

In order to acquire accurate TSA data, the specimen surface must have a uniform and high infrared emissivity. This is discussed in more detail in section 3.1.3. Additionally, the specimen must be loaded at a high enough frequency, such that any temperature changes can be considered reversible.If the frequency is too low, the specimen is not adiabatic and the temperature difference generated by the thermoelastic effect is conducted away.

3.2.1 Equipment and Setup

In the setup used for this work, the specimens were loaded using an Electropuls E3000 (*Instron, Norwood, MA, USA*). TSA was performed using a FLIR SC7600 staring array infrared camera (*FLIR, Wilsonville, OR, USA*), with data processing and capture performed using DeltaTherm2 software (*Stress Photonics Inc. Maddison, WI, USA*).

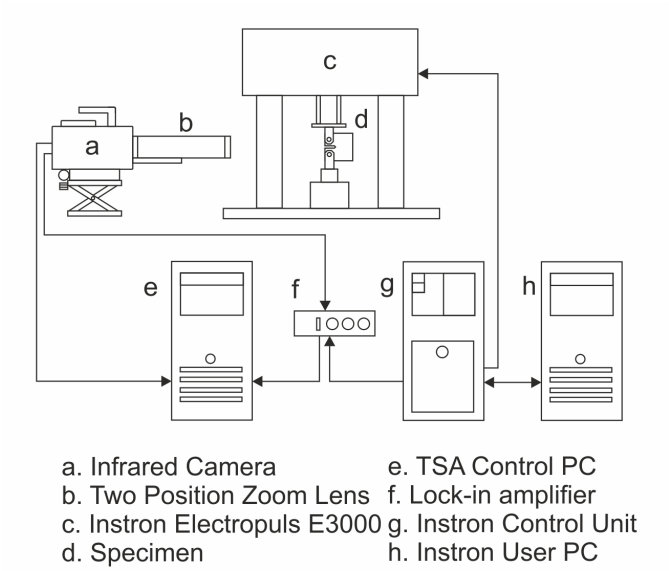

Figure 3.3: Schematic showing the a TSA equipment setup when using an external reference signal source.

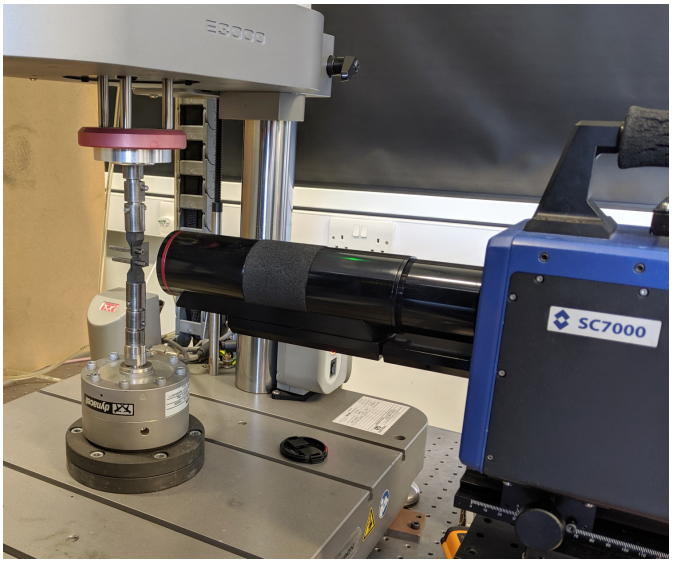

Figure 3.4: TSA setup showing the loading-machine with specimen installed viewed by the infrared camera, with two-position zoom lens attached giving a pixel resolution of 30.15*px/mm.*

The infrared camera is a staring-array design, with a self-contained Stirling pump to cool the detector array. The array is 640×512 pixels; however, a sub-window of 320×256 was used as this allowed the camera to run at a faster frame rate. The camera was mounted on

a scissor jack to allow vertical motion and a micrometer-controlled translation stage to give fine control of the left-right camera position.

A dual-position infrared zoom lens was used to acquire all data during this work. In the regular position, the lens gives a resolution of $30.15\mathrm{px/mm}$ and in the zoom position gives a resolution of $146\mathrm{px/mm}$. The lens has a fixed focal length of 50mm. Over the course of testing it was found that the zoom position data was excessively noisy, likely due to the motion of the specimen causing blurring, and it was not used for the main testing program.

3.2.2 Signal Processing

TSA data is vectorial, with both a signal magnitude, R_{TSA}, and phase angle θ_{TSA} for each pixel in the detector array. Signal magnitude is proportional to the sum of the amplitude of the applied stresses, whereas phase angle is the phase difference between the thermal response and the applied load over the image. Using the polar to Cartesian coordinate transforms, the data can be represented as projections onto the X and Y axes as X_{TSA} and Y_{TSA}.

$$X_{\mathrm{TSA}} = R_{\mathrm{TSA}} \cos(\theta_{\mathrm{TSA}}) \tag{3.2}$$

$$Y_{\mathrm{TSA}} = R_{\mathrm{TSA}} \sin(\theta_{\mathrm{TSA}}) \tag{3.3}$$

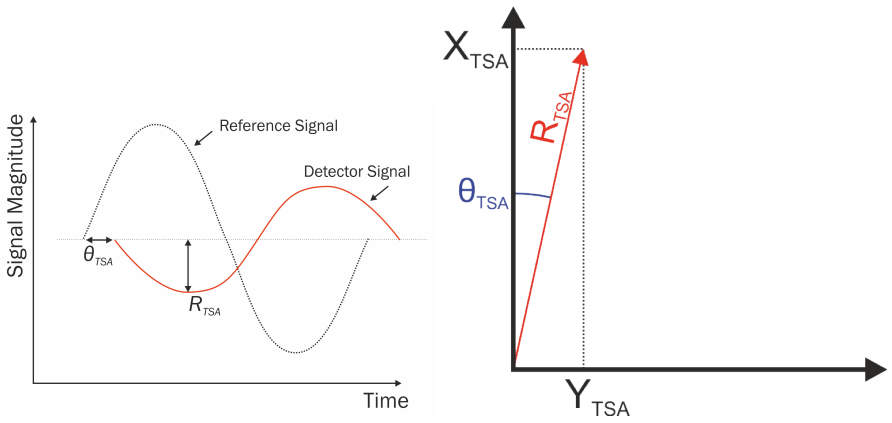

(a) (b)

Figure 3.5: Schematic showing the relationship between the reference signal and detector signal (a) and the relationship between the vectorial components of TSA data (b).

It can be seen that as $\theta_{\mathrm{TSA}} \rightarrow 0$ then $X_{\mathrm{TSA}} \rightarrow R_{\mathrm{TSA}}$. Therefore the X- and Y-images are referred to as the in-phase and out-of-phase data respectively.

The objective therefore of TSA signal processing is to extract the amplitude, R_{TSA}, and phase, θ_{TSA}, of a small sinusoidal temperature signal from background temperature fluctuations. This can be achieved using a fast Fourier transform (FFT) on the temperature signal, a fit to the temperature signal or a lock-in amplifier.

The DeltaTherm2 system used in this work uses the lock-in amplification approach. This method requires the use of a reference signal that is at the same frequency and in-phase with the load signal.

Typically the source of the reference signal is the load cell of the test-machine, which requires synchronising to ensure that the far-field phase angle, away from the crack tip, is zero and the TSA X-data are the in-phase temperature changes. The DeltaTherm2 system can also use a self-reference algorithm which generates a synthetic reference signal from the data collected in a specified section of the field-of-view of the infrared camera. This is the preferred option, as the reference signal is in-phase by definition and does not require any

extra electronics to interface with the test-machine output.

Lock-in amplification works by multiplying together the reference signal and the thermal signal at each pixel in the detector array. Prior to this multiplication, the reference signal is conditioned to have an amplitude of one and split into an in-phase reference F and a $90°$ out-of-phase reference signal G. The thermal signal is offset such that mean of the signal is zero. The result of the multiplication is a signal that has a component at twice the reference frequency and a constant. By using a low-pass filter, the component at $2f$ can be filtered out, leaving only a constant that is proportional to the amplitude of the thermal signal.

This calculation is performed for every pixel in the frame. In order to reduce the noise in the output, the result of all the frames over the accumulation time is averaged; then a further noise reduction is achieved by averaging the results of multiple accumulations over an integration time.

The calculations performed during the accumulation time are as follows:

$$X_{\mathrm{TSA}} = \frac{N\Sigma(S \times F) - \Sigma S \times \Sigma F}{N\Sigma F^2 - (\Sigma F)^2} \tag{3.4}$$

$$Y_{\mathrm{TSA}} = \frac{N\Sigma(S \times G) - \Sigma S \times \Sigma G}{N\Sigma G^2 - (\Sigma G)^2} \tag{3.5}$$

where: $X_{\mathrm{TSA}}, Y_{\mathrm{TSA}}$ are the in-phase and out-of-phase components of the detector signal, N is the number of frames in the accumulation time, S is the detector signal, F, G are in the in-phase and out-of-phase reference signals respectively. Summations are performed over all N frames.

By using Cartesian to polar coordinate transforms, the signal magnitude and phase can be obtained, as:

$$R_{\mathrm{TSA}} = \sqrt{X_{\mathrm{TSA}}^2 + Y_{\mathrm{TSA}}^2} \tag{3.6}$$

$$\theta_{\mathrm{TSA}} = \arctan\left(\frac{Y_{\mathrm{TSA}}}{X_{\mathrm{TSA}}}\right) \tag{3.7}$$

3.2.3 Calibration

In order to convert the measured temperature signal into stress values, a calibration must be performed. This can be performed by capturing TSA data for a known stress distribution [94], and is made more simple by using a uniaxial stress distribution, such that:

$$AS = \Delta\left(\sigma_1 + \sigma_2\right) \tag{3.8}$$

$$\Delta\sigma_2 = 0 \ (\mathrm{Uniaxial}) \tag{3.9}$$

$$AS = \Delta\sigma_1 \tag{3.10}$$

$$A = \frac{\Delta\sigma_1}{S} \tag{3.11}$$

A separate calibration specimen was produced for the purpose of calibration. The design, shown in figure 3.6, was based on an middle tension (MT) specimen specified in ASTM $\mathrm{E}-647$ [20], without a notch or crack, as this shared the same grips as the CT specimen and had a uniform, uniaxial stress in its centre. The MT specimen was produced and prepared in the same way as the CT specimens.

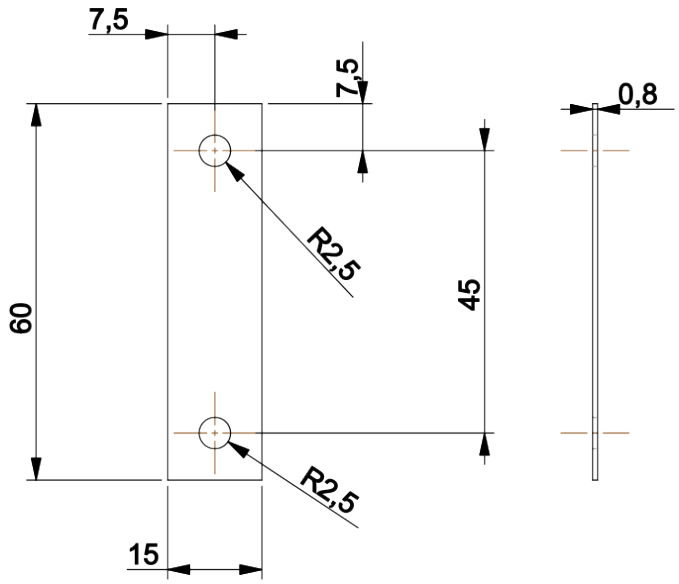

Figure 3.6: Middle tension specimen geometry, in mm.

It is necessary to capture calibration data each time an experiment is performed. This is due to the change in radiant energy with temperature described by the Stefan-Boltzmann law:

$$j^{\star} = \epsilon \sigma T^4 \tag{3.12}$$

where: $j^{\star}$ is the radiant emittance, ϵ is the surface emissivity, σ is the Stefan-Boltzmann constant equal to $5.67 \times 10^{-8} \mathrm{Wm}^{-2}\mathrm{K}^{-4}$ and T is the absolute temperature.

An increased specimen temperature therefore leads to an increase in radiant emittance, which manifests as a larger signal for a given stress.

3.2.4 Plastic Zone Measurement

Prior research by Patki & Patterson [67] and Diaz et al [64] used the phase image, θ_{TSA}, to locate plasticity, under the assumption that a change in the phase indicated a breakdown in the adiabatic assumption caused by crack tip plasticity. A thorough review of the assumptions made in TSA operation is given in chapter 4.

Provided the far-field phase is close to zero, a characteristic change in the phase occurs near to the crack tip.

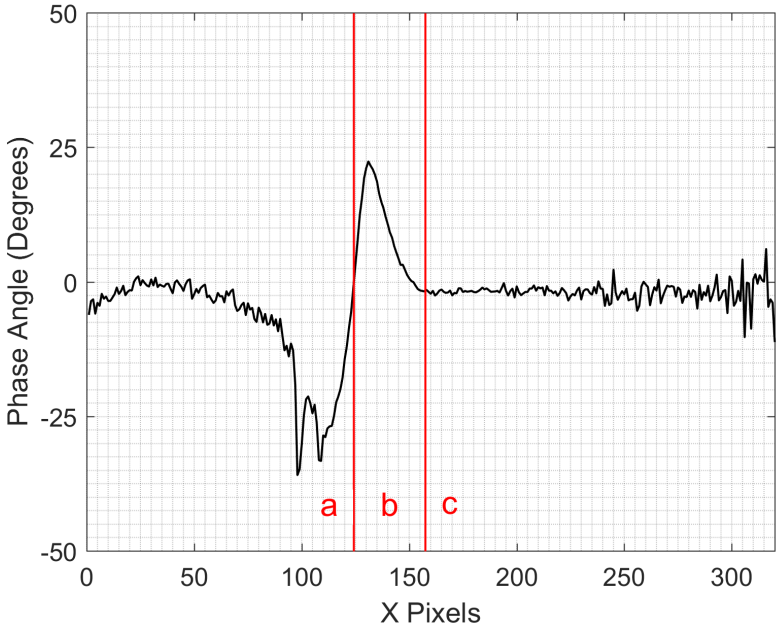

Figure 3.7: Typical phase data along a vertical line level to the crack path. Data obtained for a ≈ 7mm crack using DeltaTherm2 software. The crack tip is estimated to be at pixel 125.

Figure 3.7 shows the typical profile formed by the phase data taken along a line level with the crack path. The profile has been split into three regions as outlined by Diaz et al [64]. Region c is the far field region where the phase angle is close to zero. Region a is the crack flank region where frictional effects due to crack flank contact cause a breakdown in adiabatic behaviour. Region b is the plastic zone where the heat generated by dislocation movement causes a phase shift. A first estimate of the crack tip location is given by the zero-crossing between regions a and b.

Region b can be selected out performing a threshold on the phase image data.

3.2.5 Stress Intensity Factor Measurement

After calibration, outlined in section 3.2.3, it is possible to determine the change in effective stress intensity factor ΔK_{eff} from the TSA X-image. It is therefore sensitive to closure, which causes a reduction in the effective stress intensity factor.

A software tool called FATCAT [64] (*http://www.experimentalstress.com*), was used to compute ΔK_{eff}. FATCAT fits a Muskhelishvili-type stress distribution to the thermoelastic data using a multi-point overdeterministic method. The region where data points are used for the fit is determined by the user and aided by a 'Stanley plot' which shows the inverse square of the maximum signal on each image row, following the work of Stanley & Dulieu-Smith [63]. Close to the crack tip this value becomes non-linear due to plasticity effects and outside the K-dominated region it becomes non-linear due to the inability of the stress distribution to describe stress fields far from the crack tip. In between these extremes is a region where the Stanley plot is approximately linear, and valid ΔK_{eff} data can be collected.

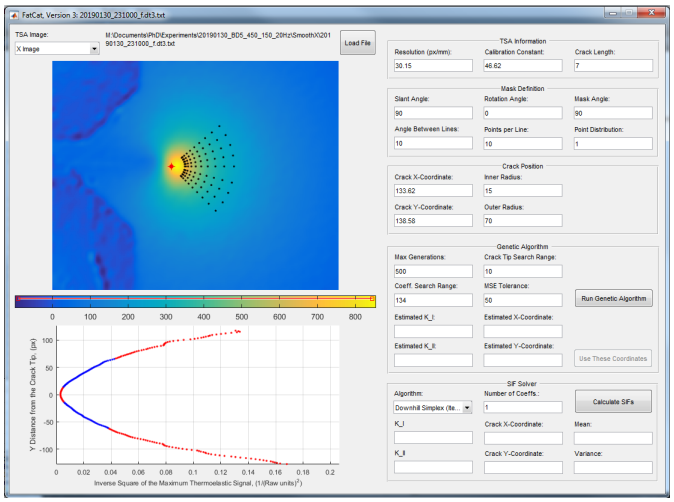

Figure 3.8: Screenshot of the FATCAT tool, showing data for a ≈ 7mm crack.

The outputs of FATCAT are a measure of the effective stress intensity factors ΔK_I, ΔK_{II} and an estimate of the crack tip coordinates (x_t, y_t). These coordinates are used to calculate the nominal crack length, given the image resolution, which was 30.15px/mm.

Despite the success of FATCAT in previous studies, a number of difficulties were encountered when using it on the data collected for the 304 stainless specimens. An initial difficulty came from the noise in the images preventing the fitting algorithm finding a stable result and was remedied by applying a Gaussian filter to the data prior to processing with FATCAT.

More difficult to diagnose was a series of measured ΔK_{eff} that were much higher than the nominal, by as much as 50%. An investigation was performed into all of the influences on FATCAT algorithm, including the calibration procedure and specimens, mean stress effects, the Muskhelishvili complex potential formulae and the nature of the TSA data collected.

The issue was finally resolved by providing FATCAT with a known stress distribution, and analysing its output. A Westergaard stress distribution with a ΔK of 12.25,resolution of 10px/mm, and calibration of 1MPa/camera unit was created using MATLAB and loaded into FATCAT. Using this known distribution allowed the variation of other control parameters of the FATCAT algorithm. Particular focus was given to the initial crack length estimation, seen in the top right of figure 3.8. A review of the mathematics behind the algorithm was performed to determine the function of this parameter. The algorithm was based upon work by Patterson & Nurse [65] and Tomlinson et al [95], using the conformal mapping procedure outlined by Muskhelishvili [96]. It was found that the initial crack length parameter was used to perform the initial conformal mapping, but was cancelled out before the results were output. Therefore, the value of the parameter should not effect the output. However, at short crack length inputs, such as those used for the small geometry specimens in this study, an instability was noted with the algorithm. As shown in figure 3.9, when the input crack length is short (< 20mm) the FATCAT output stress intensity factor range, ΔK_{eff}, diverges from the known input stress intensity factor range, ΔK_{Nom}.

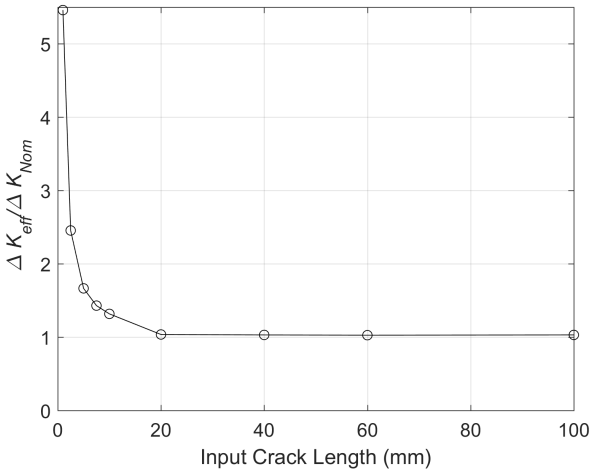

Figure 3.9: Ratio of the FATCAT computed stress intensity factor range, ΔK_{eff}, to known input stress intensity factor range, ΔK_{Nom}, showing convergence of the FATCAT output with increasing input crack length.

The settings derived from this exercise are shown in table 3.4. Large values were used for the 'crack length' to process the data to ensure convergence and reduce the uncertainty introduced to the ΔK_{eff} results from the FATCAT software.

Table 3.4: Parameters used for the computation of ΔK_{eff} using FATCAT. Calibration factors were measured for each specimen.

Parameter	Value
Resolution	30.15
Crack Length	100
Slant Angle	90
Rotation Angle	0
Mask Angle	140
Angle Between Lines	10
Points per Line	10
Point Distribution	1
Inner Radius	12
Outer Radius	30

3.3 Proton Irradiation

3.3.1 Accelerator

All irradiation experiments were performed at the Dalton Cumbrian Facility (DCF). An initial exploratory experiment was performed using the DAFNE tandem pelletron accelerator; but following the introduction of the BABY single-ended pelletron, all subsequent experiments were performed using the BABY accelerator, due to its higher current output.

The BABY accelerator consists of a positive ion source inside a high-voltage terminal that operates similarly to a Van de Graaff generator, and is enclosed in a tank containing sulphur hexafluoride gas. A pair of moving chains consisting of alternating metal pellets and

nylon links accumulate a high voltage on the terminal, which is used to accelerate the ions. An accelerating tube of reducing potential rings extends from the terminal to the end of the tank, from where the beamline extends.

Inside the source, a radio frequency antenna excites hydrogen gas to create a plasma of protons. The high-voltage terminal repels the positively charged protons down the accelerating tube, giving the protons the energy equivalent to the terminal voltage multiplied by the charge on the proton.

The BABY accelerator is located within an accelerator hall next to the larger DAFNE accelerator. Both are managed from a control room, separated from the hall by a thick concrete wall and interlocked concrete labyrinth passage. Bespoke software (Accelnet *National Electrostatics Corp. Wisconsin, USA*) was used to control the accelerators and beamlines.

3.3.2 Beamline

An overview of the main components is provided for the high vacuum beamline from the exit of the accelerator to the end-station. The beamline has a series of vacuum valves that allow the end-station to be isolated and returned to atmospheric pressure in order to load the target stage.

Steering Magnet

After exiting the accelerator, the beam first encounters a set of steering and focussing elements, which aim and focus the beam towards the steering magnet. The steering magnet directs the beam to one of two connected beamlines, LA and LB. A steering magnet is required to separate the different charge states produced in higher atomic number elements, and thus must be tuned to allow through the correct combination of mass and charge.

Rasters & Vanes

After the steering magnet the beamline enters a target room. The target room has thick concrete walls and is isolated from the accelerator hall other than via the beamline.

Immediately prior to the end-station are the rasters and tantalum vanes. The rasters allow the beam to scan a larger area of the specimen and can be controlled to determine the size of the scan area.

However, rather than raster directly onto the specimen a series of tantalum vanes are placed between the target and rasters. There are four vanes (top, bottom, left and right) that can be moved independently to achieve a more accurate definition of the irradiated area.

Monitoring and Control

Beam position and focus is monitored by beam position monitors. These are probes that rotate in the beamline and display the profile of the beam on an oscilloscope in the control room. The level of focus in the X and Y directions can then be easily seen by the sharpness of the peaks, and beam alignment determined by the position of the peaks.

Focussing of the beam is performed by a number of Einzel lenses and magnetic quadropole elements in addition to X and Y steering elements to control beam location.

Along the beam are a series of Faraday cups (tantalum cups) that can be inserted into the beam to stop the beam at that point. These measure the beam energy and can be used to ensure there is no loss of current due to misalignment, such as through the steering magnet.

3.3.3 Target Stage

The target stage holds the specimen to be irradiated and provides charge measurement and temperature control. The stage consists of a nickel block, with a cooling loop, upon which various layers are mounted.

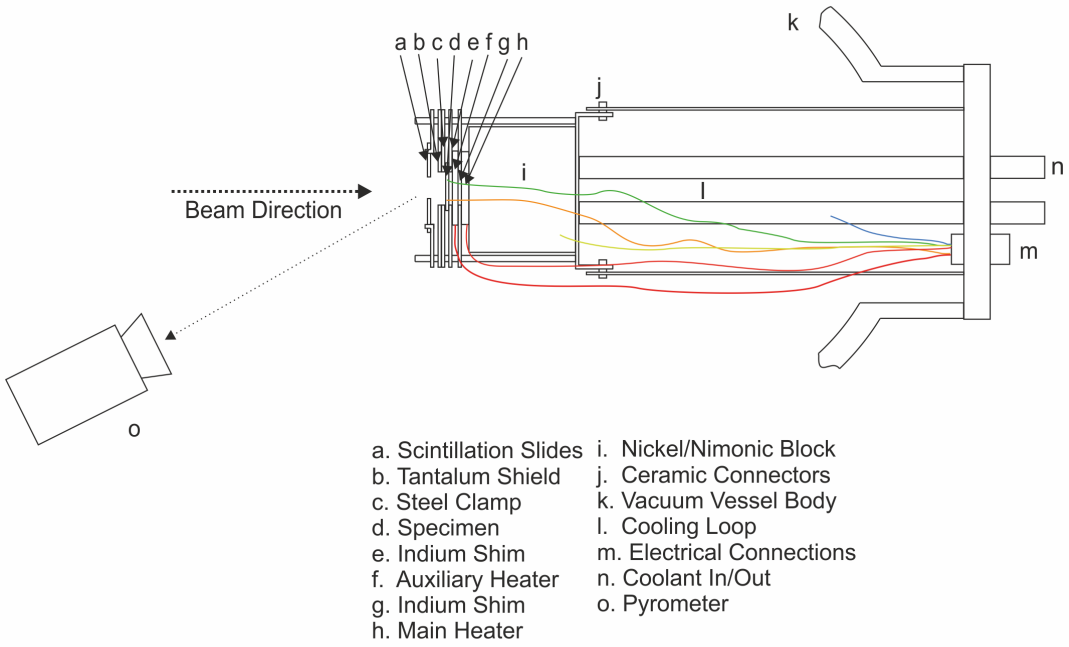

Figure 3.10: Schematic showing the target stage with detail on the mounted layers.

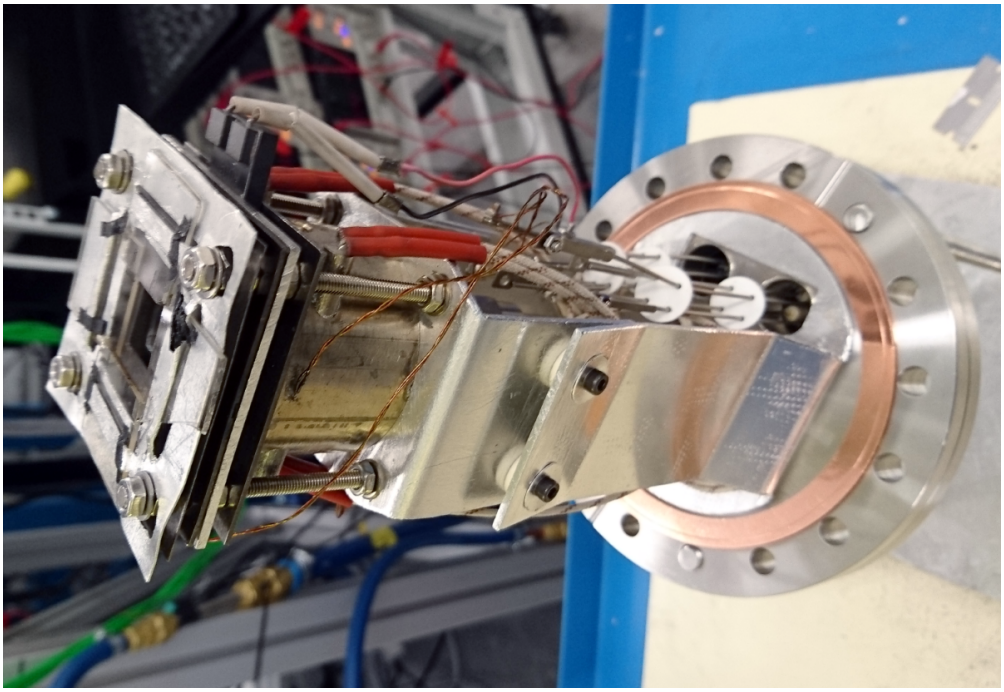

Figure 3.11: Photograph of the target stage as mounted immediately prior to irradiation. The beam would impact the target stage from the left of the image.

A description of the purpose and function of layers, from bottom up, is as follows:

i. Nickel Block The block contains the cooling loop, which extracts the excess heat deposited by the beam.

h. Main Heater Three 90W cartridge heaters embedded into the block make up the main heater.

g. Indium Shim Lower The indium shim is a 1mm thick plate with a 12×12mm square hole cut in the middle. Indium is placed in the hole, which is sandwiched between the block (h) and auxiliary heater (f). During irradiation the indium melts, providing good thermal contact between the layers. The lower shim provides good thermal contact between the block (and cooling loop) and the other layers. In later irradiations this shim was removed and replaced with a eutectic layer after issues were encountered with poor temperature

control due to this layer freezing during irradiation.

f. Auxiliary Heater The auxiliary heater is a 270W ceramic heater. It provides additional heating as the cartridge heaters in the block are not capable of holding the specimen at the required irradiation temperature.

e. Indium Shim Upper The upper shim is the same as the lower shim in design. It provides good thermal contact between the specimen and the other components of the stage.

c. Steel Clamp The stainless steel clamp is a thin plate with a square hole, of slightly larger dimensions than the shield (b). The back of the plate features two grooves to allow thermocouples to be fed through and welded to the specimen.

b. Tantalum Shield The tantalum shield is a thin plate that covers the clamp (c), with a square hole that allows the beam through to the specimen. Tantalum is used due to its low activation under proton irradiation, unlike steel. If the beam becomes misaligned during the test, it will hit the tantalum, which will not activate.

a. Scintillation Slides The scintillation slides are a set of four quartz slides that are arranged to the top, bottom, left and right of the area to be irradiated. Prior to irradiation, marks are made on the slides to indicate the extent of the area to be irradiated. Under irradiation from the beam, the slides glow and the marks are visible, which allows the operator to move the tantalum vanes in the beamline to ensure that only the planned area is irradiated.

Temperature Control

Prior to irradiation the stage is heated to the irradiation temperature with the specimen mounted using both the main and auxiliary heaters. The specimen temperature is monitored with a spot-welded thermocouple and an infrared camera. The thermocouple is attached to the specimen in a region covered by the tantalum shield, protected from the beam, but therefore also not visible to the infrared camera. To ensure the thermocouple and infrared camera are reading the same temperature, the stage is allowed to heat up and reach a steady-state temperature. The thermocouple temperature is then used to calibrate the emissivity used in the infrared camera temperature calculations. During irradiation, the infrared camera must be used to measure temperature as it can image the irradiated area, unlike the thermocouple which is mounted beneath the clamp away from this area.

Further temperature monitoring was provided by thermocouples attached to the top of the block and cooling loop inlet. These are primarily for safety monitoring as an excessive temperature on the loop or block could suggest a failure of the cooling system.

During an irradiation experiment the cooling loop circulated water through the block at 20°C, the cartridge heaters were generally run at maximum power and the voltage of the auxiliary heater varied to maintain the temperature.

Charge Measurement

The block assembly is electrically isolated from the rest of the stage with insulating ceramic bushes. A nano-ammeter was used to measure the current on the block, which was integrated over time to give the accumulated charge.

In addition to the block charge measurement, the tantalum vanes in the beam line were also monitored to determine the extent to which the raster scan by the beam overlapped onto the vanes. This over-raster is required to ensure that the beam is fully covering the

planned irradiation area.

3.3.4 Accelerator Operation

Specimen Mounting

The following procedures were undertaken to mount the specimen in the target stage described in section 3.3.3. This process started from the nickel block containing the cooling loop, with no other components mounted.

1. The target stage was placed in a cradle that held it vertically.
2. The top of the block was cleaned of any residue from previous irradiations.
3. A layer of eutectic was applied to the top of the block. The auxiliary heater was then placed on top of the eutectic and an empty shim placed on top of the heater, that was held in place temporarily by four nuts.
4. The cooling loop pipes and electrical connections were attached and the cooling loop pump turned on. Then the heaters were turned on.
5. Indium was placed into the shim, where it melted. The molten indium was manipulated such that it filled the shim completely.
6. The heaters were turned off, causing the indium to freeze. Any excess indium was removed carefully using a razor blade. The cooling loop was turned off and disconnected.
7. The nuts holding the shim were removed and the specimen located on top of the indium shim.
8. The steel clamp was placed over the specimen and temporarily held in place with four nuts.

9. A thermocouple was fed through the clamp and spot welded to the specimen.

10. The temporary nuts were carefully removed and a tantalum shield placed over the steel clamp. The nuts were replaced, to hold the shield and clamp tightly to the specimen.

11. The scintillator slides are placed on top and held in place using washers and nuts.

12. Fiducial marks were made on the slides using a black marker, following the guide marks etched onto the specimens.

13. The copper gasket was replaced, to ensure a vacuum-tight seal with the end-station.

Irradiation Experiment Procedure

Following the specimen mounting, the following procedure was used to perform the irradiation experiment:

1. The target stage was loaded into the end-station and bolted in place. A roughing vacuum pump was turned on, which reduced the end-station pressure to 1×10^{-2}Torr.

2. The vacuum turbo pump was turned on, which brought the end-station pressure to a high vacuum of 1×10^{-7}Torr.

3. The electrical connector and cooling loop pipes were attached.

4. The cooling loop pump was turned on. The three block heaters were turned on, using 30V power supplies.

5. The auxiliary heater power was slowly increased, using three 30V power supplies connected in series.

6. The temperature was monitored using the attached thermocouple and the power to the auxiliary heater was varied to maintain the irradiation temperature of 360°C.

7. Once the specimen was held stable at the correct temperature, the emissivity used in the temperature calculations of the observing infrared camera was adjusted to calibrate the camera with the thermocouple.

8. The beam transmission and alignment up to the final Faraday cup before the end-station were optimised using the focussing and steering elements along the beamline.

9. A low beam current (3μA) was used to align the tantalum vanes such that the glow of the scintillator slides matched the fiducial marks.

10. The beam current was increased up to the desired level, typically 30μA, while the auxiliary heater power was reduced to compensate for the beam heating.

11. The irradiation experiment continued for as long as required, determined by the charge accumulated on the specimen. The temperature was continuously monitored and the auxiliary heater power was manually adjusted to maintain the temperature.

3.3.5 Operational Challenges

During the course of experimentation a number of challenges were encountered with the operation of the accelerator.

Temperature Control

The first setup used two indium shims, (e) and (g) in figure 3.10, rather than one shim and one eutectic layer. Occasionally shim (g) would freeze or partially freeze during the experiment, reducing the thermal contact between the layers and cooling loop, causing large temperature excursions. This loss of control typically occurred as the experiment was beginning and temperatures of 440°C could be reached for short periods of time.

3.3.6 Damage Profile

As discussed in the literature review, section 2.3, one of the primary differences between proton and neutron irradiations is the damage profile through the specimen. Due to the charge on the proton, it will interact with the electrons in the target. This results in an electronic stopping force which initially slows the proton down, before nuclear stopping dominates. Around the point where nuclear stopping dominates, the protons will collide with a nucleus in the target, causing a damage cascade and come to rest. As the beam was monoenergetic this stopping point is in approximately the same place for all the incident protons. This results in a concentrated region of damage known as the Bragg peak.

A further difference relating to neutron damage is the presence of protons themselves. As the specimen thickness is much larger than the Bragg peak, there will be protons left in the specimen. Protons are simply ionised hydrogen atoms, which are well known for causing embrittlement in steels. Murakami et al [97] found that hydrogen embrittlement caused an increase in fatigue crack growth rates, particularly at low loading frequencies (< 1Hz). It is known that radiation damage acts to trap some hydrogen; but, due to the high irradiation temperature and high diffusivity of hydrogen in austenitic steels it is unlikely much hydrogen will remain. The amount of hydrogen retained has not been measured, and is a possible avenue of further study.

In order to estimate the damage, a Monte Carlo simulation was performed, using a program called SRIM [98]. Following the best practice guidance of Stoller et al [99], a displacement energy of 40eV and lattice binding energy of 0eV were used. The elemental composition of the target was as per table 3.1, with a density of 8gcm^{-3}, however there no microstructural considerations made by SRIM, i.e. the elements are uniformly distributed throughout the target thickness. The output of SRIM was a file with the estimated vacancies generated per Angström per ion. The number of ions impacting the specimen could be

calculated by the measured charge accumulated on the target stage.

The following equation was then be used to scale the SRIM output and estimate the total damage in dpa:

$$D = \frac{VH}{N_t} \times 1 \times 10^8 \tag{3.13}$$

$$H = \frac{C}{eA} \tag{3.14}$$

$$N_t = \frac{m}{\rho N_{Av}} \tag{3.15}$$

where: D is estimated total damage in dpa, V is the estimated vacancies given by SRIM in vacancies per Angström per ion, H is the total proton fluence of the irradiation in ions/cm^2, N_t is the atomic density of the target in atoms/cm^3, C is the total accumulated charge, e is the charge on the proton (1.602×10^{-19}C), A is the irradiated area in cm^2, m is the average mass number of the target, ρ is the density of the target in g/cm^3, and N_{Av} is Avogadro's number.

Deposited hydrogen was estimated using the distribution of recoiled ions in the range data produced by SRIM.

The damage profile after this procedure was performed is shown in figure 3.12 for each increment of depth into the target.

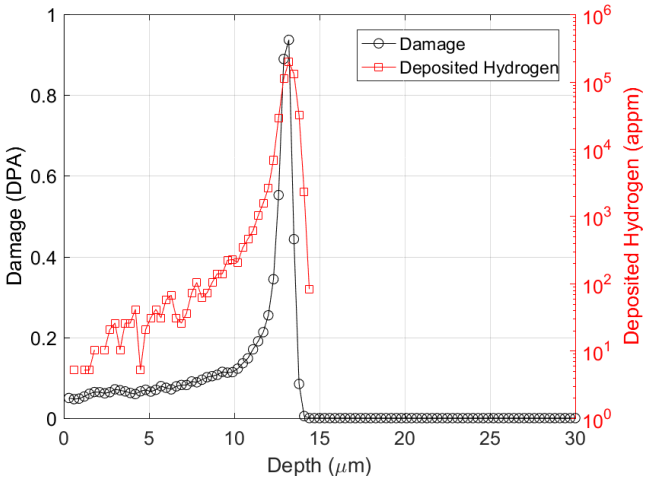

Figure 3.12: Result of Monte Carlo simulation using SRIM showing estimated damage profile (left axis) and deposited hydrogen (right axis) for 1.35×10^{18}protons/cm^2*, with a proton energy of* 1.6*MeV*

It is important to note that whilst dpa is used as an attempt to correlate damage caused by neutron and proton irradiations, it is only an estimate and will be provided for reference, but damage levels will be described using the proton fluence.

3.4 Microhardness Testing

In order to detect the edge of the irradiation damaged area, microhardness testing has been used. As discussed in the literature review, section 2.2.2, this involved indenting the specimen with a pyramidal indenter with a known force and measuring the size of the indent created.

A DMH-2 microhardness tester (*Matsuzawa Seiko Co. LTD, Tokyo, Japan*) was used to take measurements with a load of 200gF. Following ASTM E384, indents were made no closer than 2.5 times the indenter diagonal size. In practice, the indenter diagonal had a maximum dimension of 50μm, giving a minimum spacing of 0.125mm. For all measurements, a separation of 0.2mm was used. Measurements were made manually using an adjustable calliper in the viewing eye piece.

The grain size in the 304 stainless steel used was approximately 50μm, and roughly equiaxed, estimated using light microscopy on the surface of a etched specimen. This meant that a single indent could be contained in only one grain. This could lead to variability in results as the crystallographic orientation of each grain can effect the resistance to indentation.

The observed increase in hardness across the boundary between the unirradiated and irradiated material was modelled using a sigmoid-type curve of the form:

$$H(x) = H_0 + \frac{H_I}{e^{-s(x-x_I)}} \tag{3.16}$$

where: x is the distance from the load-line, H is the Vickers hardness measure at 200gF, H_0 is the hardness of the unirradiated material, H_I is the increase in hardness, s is the sharpness of the change in hardness and x_I is the mid-point of the increase.

3.5 Fatigue Crack Growth Testing

Fatigue crack growth tests were performed by applying a dynamic load to a specimen containing a crack and measuring the crack extension at regular intervals. The crack growth $\frac{da}{dN}$ in mm per cycle could then be obtained.

3.5.1 Grip Design

ASTM E647[20] provides a standard pin and clevis design for the grips to be used for a compact tension specimen. However, over the course of testing it was found that there was an asymmetry occurring in the data, which was unexpected as the setup used should produce a symmetric stress distribution either side of the crack plane. The asymmetry was manifest as a 'hotspot' in the second harmonic TSA signal which was always inclined towards the bottom right hand side of the specimen, regardless of specimen orientation in the grips. This can be seen in figure 3.13.

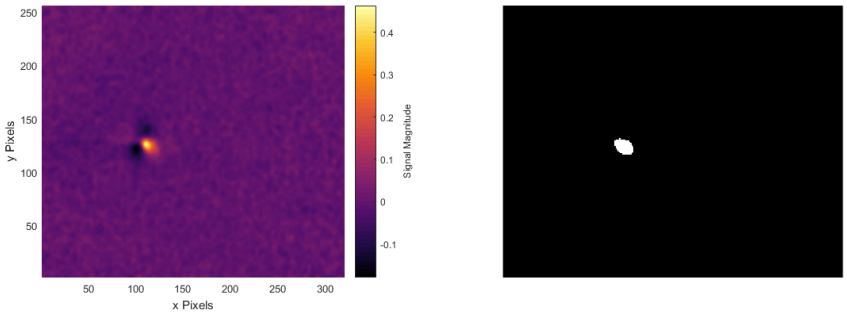

(a) (b)

Figure 3.13: Raw second harmonic TSA X-image (a) and the thresholded X-image (b) showing asymmetry of the hotspot inclined towards the bottom right hand corner.

A similar report of asymmetry in compact tension fracture toughness tests had been reported by Bubsey et al [100]. The authors found friction on the loading pins prevented smooth rotation of the specimen. The original grip design, shown in figure 3.14 (a) had a thick clevis cross section. Using a higher strength steel, it was possible to thin the clevis cross section, so that the contact patch with the pins was reduced.

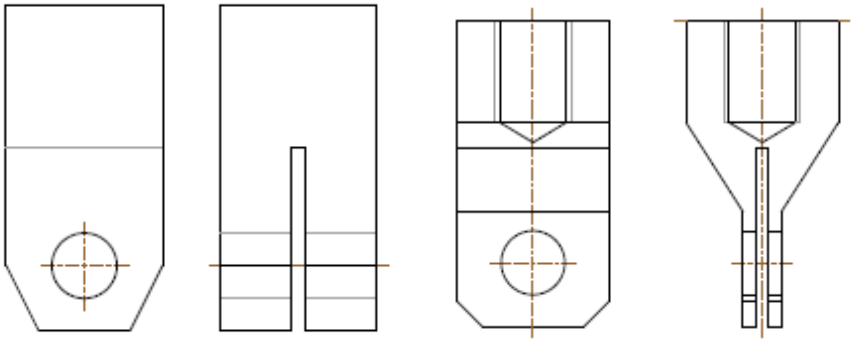

(a) (b)

Figure 3.14: Original grip design (a) and modified grip with smaller pin contact patch (b).

It was found that the new grip design did not give as large an improvement as expected. Further modifications were made based on Bubsey et al [100] to change the shape of the pin hole from circular to a modified circle, as shown in figure 3.15. This design was intended to

be used with a smaller diameter pin (4 vs 5mm).

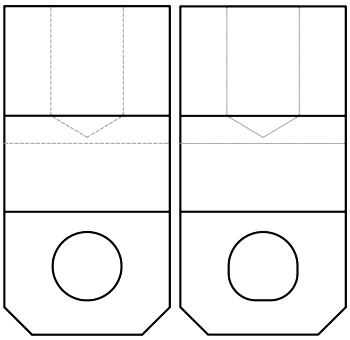

(a) (b)

Figure 3.15: Circular clevis hole (a) and modified circular hole (b).

However, the smaller diameter pin introduced an uncertainty of the location of the pin within the hole and therefore difficulty in determining the exact location of the loading line, which has consequences for crack length measurement.

The final setup used was with the thin-section grips with a modified pin hole, but with 5mm diameter pins. This provided some improvement over the initial asymmetry, but did not completely eliminate the issue.

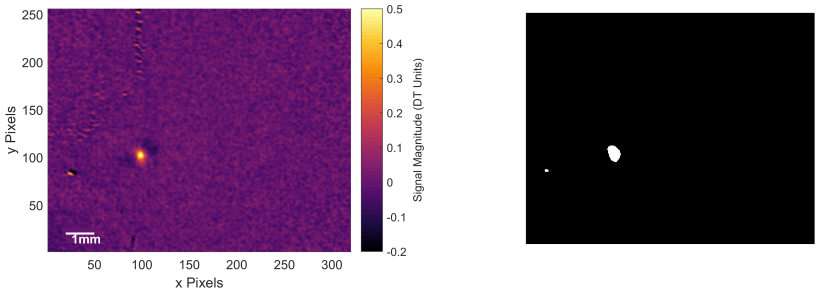

(a) (b)

Figure 3.16: Raw second harmonic TSA X-image (a) and thresholded X-image (b) showing reduction in asymmetry compared to figure 3.13 when using the new grip design.

3.5.2 Self-Aligning Load String

In addition to testing new grip designs to rectify the asymmetry, the load string was examined to determine if there was a possibility of a misalignment generating an out-of-plane load.

A misalignment of approximately 0.05mm was found in the Z-direction between the top and bottom grip. Such a small displacement would normally be within tolerance, but as the specimens used are only 0.8mm thick, this constitutes nearly 7% of the specimen thickness.

In order to rectify the misalignment a set of self-aligning connectors were designed for the load string. The intent of the design was to provide freedom for the specimen to rotate in all planes, such that the load was applied vertically to the specimen in its own frame of reference.

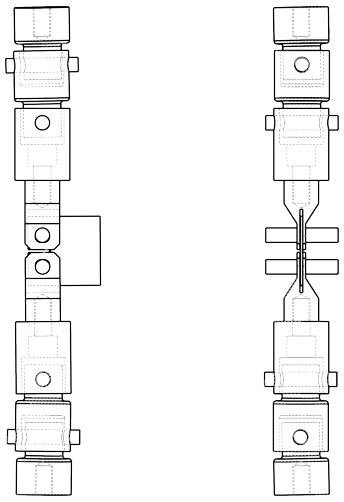

Figure 3.17: Design of new load string including self-aligning couplings above and below the clevis grips.

Chapter 4

Plastic Zone and Closure Detection with Thermoelastic Stress Analysis

Previous authors such as Diaz et al [64] have demonstrated the ability of thermoelastic stress analysis to detect the effects of plasticity by means of a phase shift, as outlined in chapter 3 section 3.2.4. However, during the course of this study it was found that this method did not produce results that were consistent with previous studies or results that were in agreement with theory. This chapter focusses on the likely source of this issue and a potential solution using the second harmonic of the thermal signal.

4.1 Thermoelastic Phase Difference

One of the fundamental assumptions made during the derivation of the relationship used in TSA is that the temperature changes occur adiabatically, i.e. any temperature changes are reversible. This assumption is true under the following circumstances:

1. The loading frequency is sufficiently high.

2. Stress gradients are low.

3. There are no other heat sources.

Assumption 1 is somewhat dependent on the others, as it essentially requires that the loading frequency is high enough that conduction is minimised. One way of assessing conduction is by the thermal diffusion length, u, the characteristic length for heat conduction during one period of a cyclic load. It is given by [101]:

$$u = \sqrt{\frac{D}{\pi f}} \tag{4.1}$$

$$D = \frac{k}{\rho C_p} \tag{4.2}$$

where: D is the thermal diffusivity in $\mathrm{m^2 s^{-1}}$, f is the loading frequency in Hz, k is the thermal conductivity in $\mathrm{W(m.K)^{-1}}$, ρ is density in $\mathrm{kgm^{-3}}$ and C_p is the heat capacity at constant pressure in $\mathrm{J(kg.K)^{-1}}$.

For 304 stainless steel, D can be calculated as $4.05 \times 10^{-6} \mathrm{m^2 s^{-1}}$ [102] and ideally, the thermal diffusion length, u, should be smaller than the spatial resolution of the TSA system, 30.15px/mm. In practice, this is extremely difficult to achieve and would require loading at frequencies of thousands of hertz. As a compromise, the highest practical loading frequency should always be used in order to minimise the effect of conduction. For example, in this work a loading frequency of 20Hz was used. This gave a reasonable range of crack growth rates over the duration of the test. Faster loading frequencies caused rapid crack growth that resulted in blurring due to the crack tip moving during the accumulation time of the data captures. This 20Hz loading frequency gives a thermal diffusion length of $u = 0.25$mm, meaning that there will be difficulty resolving heat sources smaller than approximately 8px.

When using thermoelastic stress analysis to image a cracked specimen, assumptions 2 and 3 begin to break down. The crack acts as a stress raiser, causing large stress gradients in the vicinity of the crack tip. These in turn cause larger temperature gradients, which

increase the amount of conduction, as demonstrated by Fourier's Law:

$$q = k\nabla T \tag{4.3}$$

where: q heat flux density in Wm^{-2}, k is the thermal conductivity in $\mathrm{W(m.K)}^{-1}$, and ∇T is the temperature gradient in Km^{-1}.

Assumption 3 is further violated by the presence of the plastic zone. Dislocation motion within the plastic zone acts like an irreversible heat source. Diaz et al [64] first proposed that the phase shift observed in the thermoelastic phase image near the crack tip could be associated with this violation of adiabaticity, and the plastic zone therefore appears as a phase shift in the thermoelastic phase data.

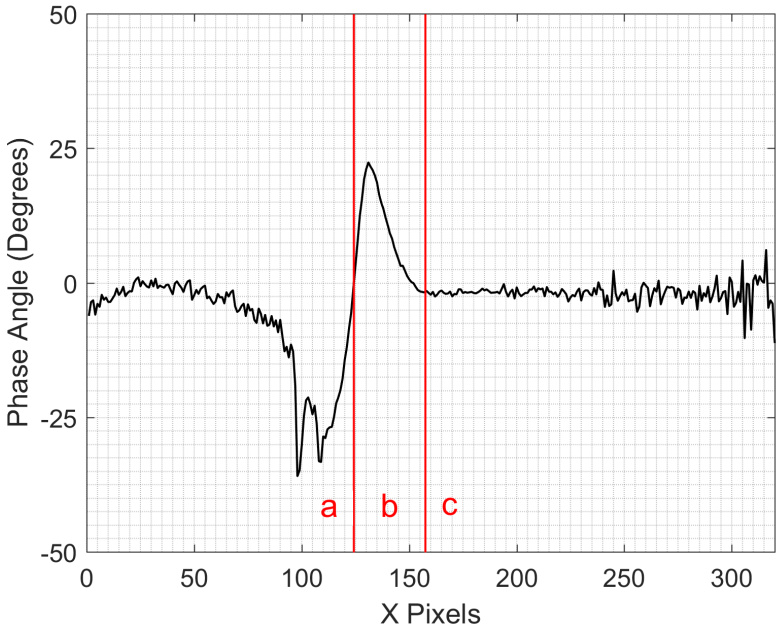

Figure 4.1: Typical phase data along a line parallel to the crack path for an austenitic stainless steel specimen containing a ≈ 7mm crack. Data obtained using DeltaTherm2 software, crack tip estimated to be at $x = 125$ pixels.

Figure 4.1 shows the different regions identified by Diaz at al. Region c is the far-field phase difference, which should be close to zero as it is free of non-adiabatic effects. Regions

a and b were identified with non-adiabatic effects from the crack flanks and plastic zone respectively. Note that the sign of the phase shift in regions a and b is arbitrary and depends on the TSA system used; however, they will always be opposite in sign to one another. The size of the plastic zone can then be obtained by thresholding the data and measuring the area of the phase shift, as originally demonstrated by Patki & Patterson [67].

4.1.1 Phase Difference in 304 Stainless Steel

Patki & Patterson [67] and Yang et al [103] demonstrated that the phase method could be used successfully in aluminium specimens and commercially pure titanium respectively. Austenitic stainless steel has markedly different thermal and mechanical properties that could impact the utility of the phase method.

Table 4.1: Relevant thermal and mechanical properties for aluminium 6061-T6, stainless steel 304 and grade 1 titanium, given by ASM Matweb [102].

Property	Al 6061-T6	Grade 1 Ti	SS 304	Unit
ρ	$2,700$	$4,500$	$8,000$	kgm^{-3}
C_p	896	528	500	$\mathrm{J(kg.K)}^{-1}$
α	2.36×10^{-5}	8.9×10^{-5}	1.73×10^{-5}	K^{-1}
k	167	17	16.2	$\mathrm{W(m.K)}^{-1}$
D	6.9×10^{-5}	7.15×10^{-6}	4.1×10^{-6}	$\mathrm{m}^2\mathrm{s}^{-1}$

Attempts to replicate the phase method using austenitic steel specimens encountered difficulty. The phase data showed the same deviation as observed by other authors, as seen in figure 4.1, but the behaviour over the course of a crack growth test was inconsistent. A threshold value of 2° was used in the method employed by Patki & Patterson as it was not possible to obtain a reasonable measure of area using a value closer to zero.

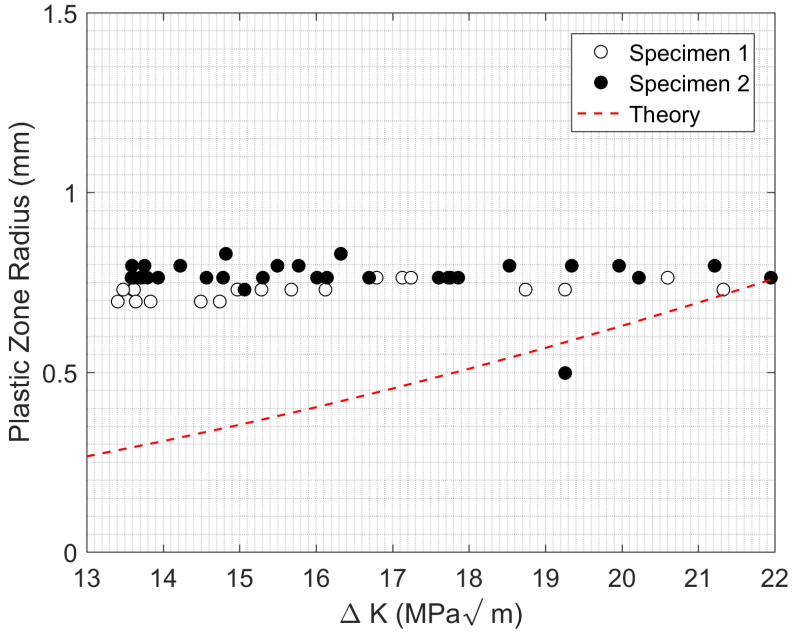

(a)

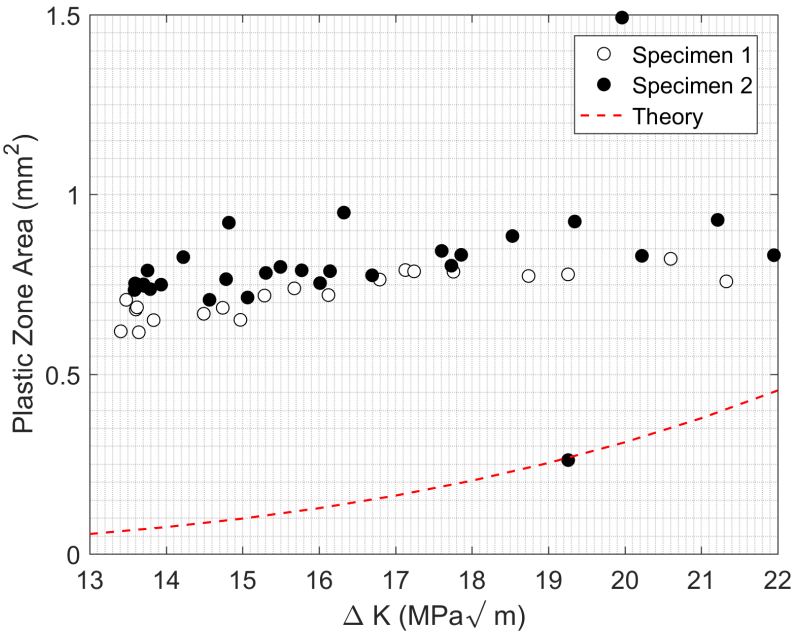

(b)

Figure 4.2: Change in plastic zone radius a) and area b) measured using the phase method against the stress intensity factor range. A threshold value of 2° was used to identify the positive phase region ahead of the crack tip. Specimens were loaded at $R = 0.5$ at a frequency of 20Hz. A theoretical prediction has been generated by assuming a circular plastic zone with a diameter equal to the plastic zone radius based on Irwin's approximation in equation (2.15).

The equations used to generate the theoretical prediction in figure 4.2 use Irwin's approximation for the cyclic plastic zone radius. This is obtained by taking $\alpha^c = \frac{1}{\pi}$ in equation (2.15) and are given by:

$$r_p = \frac{1}{\pi}\left(\frac{\Delta K}{2\sigma_{YS}}\right)^2 \tag{4.4}$$

$$a_p = \pi\left(\frac{r_p}{2}\right)^2 \tag{4.5}$$

where: r_p is the theoretical plastic zone radius, a_p is the theoretical plastic zone area if the plastic zone were circular and σ_{YS} is the yield stress of 225MPa.

It is clear in figure 4.2 a) that the radius does not show an increasing trend with ΔK as would be suggested by theory, and not as much as observed by Patki & Patterson [67] in their aluminium specimens. Whilst there is an increasing trend in the area data, the magnitude of the increase is not close to the theoretical values.

In addition to showing a reduced dependence on ΔK, the phase method demonstrated a strong dependence on loading frequency, as shown in figure 4.3.

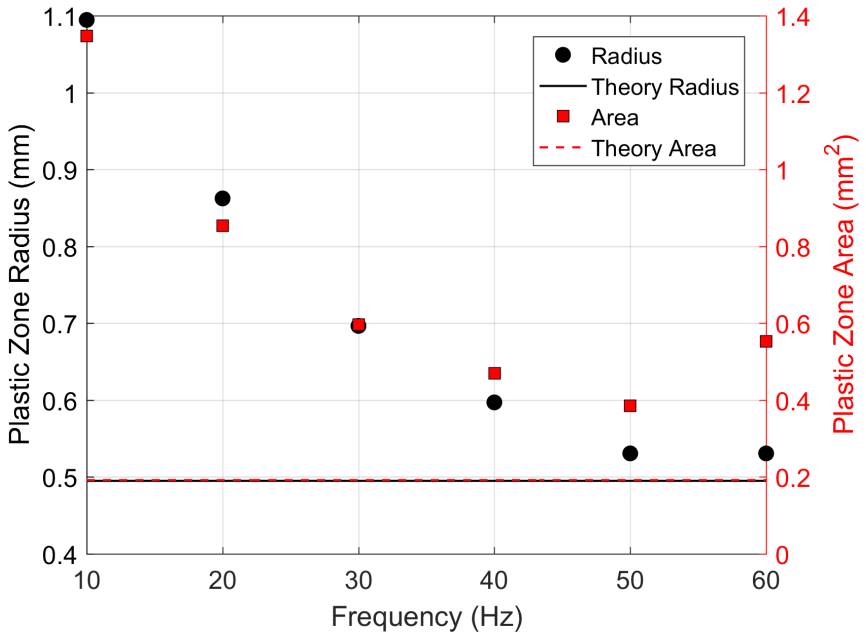

Figure 4.3: Plastic zone radius (left axis) and plastic zone area (right axis) obtained from the phase method due to Patki & Patterson [67] at different frequencies for an austenitic stainless steel specimen containing a $\approx$ 7mm crack.

This might be expected given equation (4.1), which predicts a $1/\sqrt{f}$ dependence on the thermal diffusion length, which would result in decreased blurring as the loading frequency was increased. It indeed appears as if the radius and area measurements are converging towards the theoretical value as frequency increases. However higher frequencies are not practical for testing purposes, due to the high crack propagation rate over time.

4.2 Thermal Finite Element Modelling

As shown above, in early testing it became apparent that the plastic zone size measured by the phase angle method was more strongly dependent on loading frequency than the increasing stress intensity factor. This observation has been previously made by Tomlinson & Patterson [104] who showed that a decrease in plastic zone size followed a similar trend to the thermal diffusion length given by equation (4.1). For the test conditions used, it was

found that above a loading frequency of 30Hz for Al-2024 and 20Hz for commercially pure titanium, the change in plastic zone size was negligible. Figure 4.3 demonstrates that if such a limiting frequency exists for 304 stainless steel, it is much higher than those reported by Tomlinson & Patterson.

To understand the effect of the thermal diffusion on the TSA outputs, a finite element model was created using LS-Dyna (*LSTC, Livermore, CA, USA*).

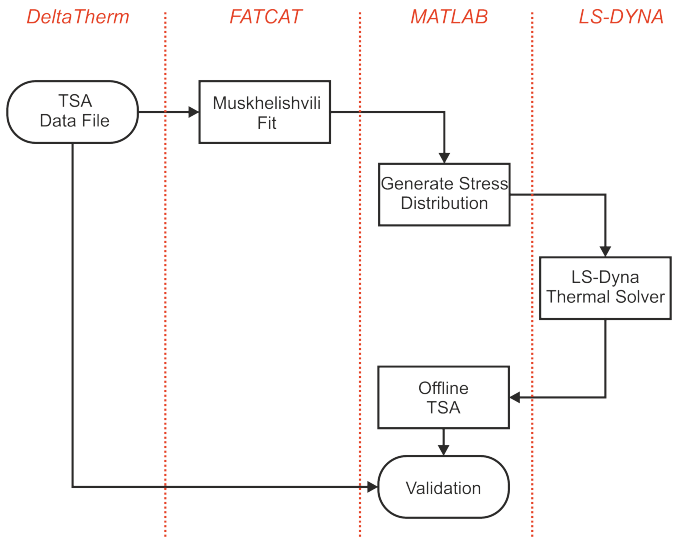

Figure 4.4: Flow chart showing the steps to generate model TSA data from the stress distribution determined from the fit to data given by FATCAT. Model TSA output is validated against the original file. The model assumed no plasticity effects.

The model consisted of an uncracked square plate of 6400 thermally isotropic solid elements with dimensions $8 \times 6 \times 0.8$ mm representing the section of the specimen inside the field of view of the infrared camera. The model was given an initial temperature of 22°C and heat was applied over time to the elements using to represent the thermoelastic effect. The magnitude of the heat input was determined by a Muskhelishvili-type stress distribution, varying sinusoidally over time.

As shown in figure 4.4, the input stress distribution for the model was determined by a FATCAT fit to data captured from a specimen. No plasticity effects were included in the

model.

Following the same approach as McKelvie [93], whereby a sinusoidal stress over time generates a sinusoidal heating over time due to the thermoelastic effect, the heat input into the model was:

$$Q(x, y, t) = K\sigma(x, y)\sin(2\pi f t) \tag{4.6}$$

where: $Q(x, y, t)$ is the heat input at point (x, y) in a coordinate system centred on the crack tip and time t, $K = 1 \times 10^5$ is a constant to convert stress to heat, $\sigma(x, y)$ is the stress at point (x, y) as determined by a fit to collected data and f is the loading frequency.

A loading frequency of 20Hz was used, so that comparisons between the model and collected data could be performed. The model was run for 0.1s with time steps of 0.001s, with the temperature at each node output at each time step, $T(x, y, t)$. MATLAB scripts were used to perform offline TSA on the model temperature output so a comparison between the magnitude and phase of the finite element model and real data could be performed to demonstrate the validity of the model.

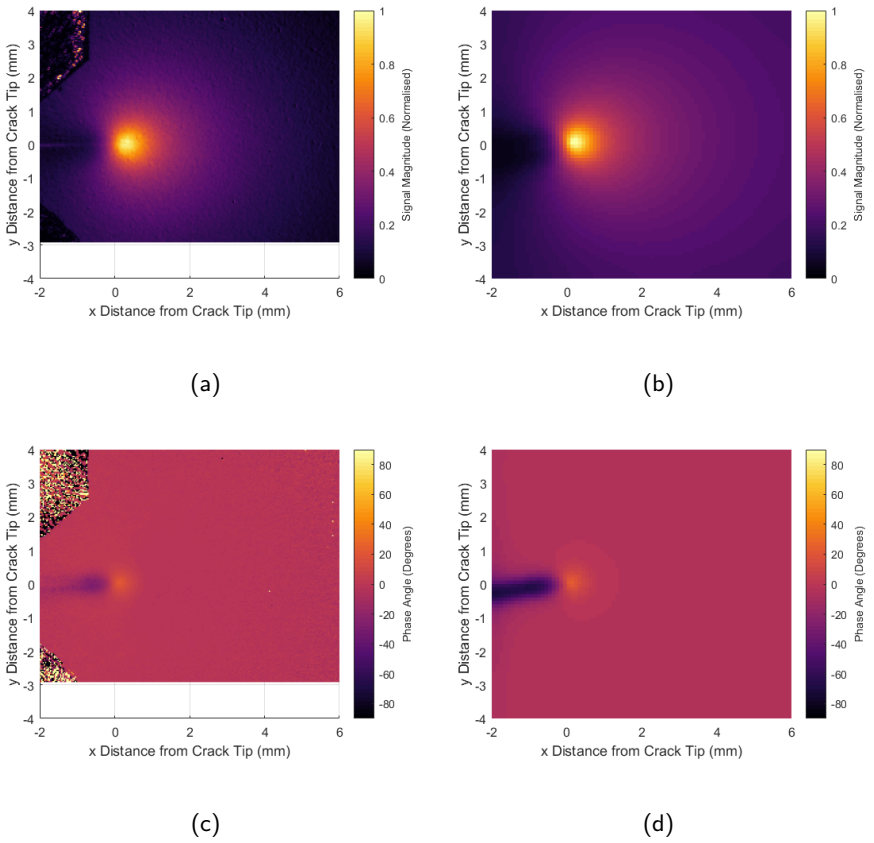

Figure 4.5: Comparison between measured (left) and predicted (right) TSA data for magnitude (top) and phase (bottom). The measured data was from a specimen with a 6.9mm crack loaded sinusoidally with 450 ± 150N at 20Hz. Noisy regions on the left of measured images are from the specimen grips.

Figure 4.5 shows the comparison between experimental data collected for a specimen with a 6.9mm crack loaded sinusoidally with 450 ± 150N at 20Hz and the model output using the calculated stress distribution from the data. Qualitatively, the outputs from the model and experiment are similar. This is not surprising for the magnitude images as these are strongly determined by the stress distribution and the measurement data was used as an input for the model. The phase images, however, are interesting. A phase change occurs in the model output, even in the absence of plasticity.

To quantitatively compare the two-dimensional data sets the methodolody employed by Sebastian et al [105] has been used. First the data sets are normalised and decomposed

into Chebyshev polynomials, a procedure equivalent to fitting a polynomial function to a one-dimensional data set. The data can then be expressed by a feature vector comprising the weights assigned to each kernel of the polynomials in the decomposition. The Euclid software [106] was used to perform the orthogonal decomposition and the first 50 Chebyshev polynomials were used to provide suitable reconstruction accuracy. Error bounds for the comparison are given by the vector addition of the reconstruction error and experimental error. Finally, the weights of the feature vectors for the experiment and model were plotted against one another and the bounds displayed. The model is regarded as a valid representation of reality if all points lie within the error bounds.

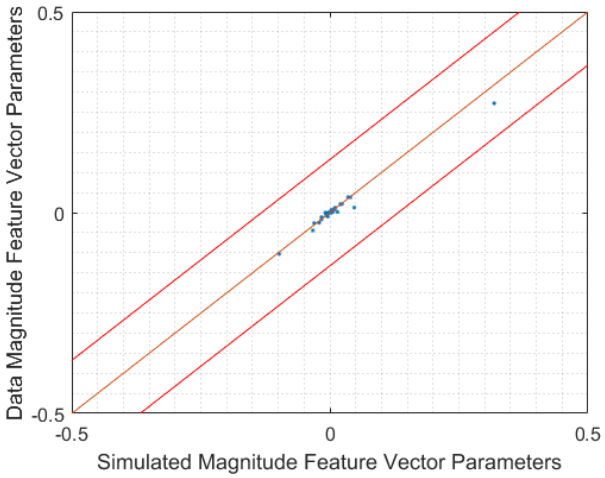

(a)

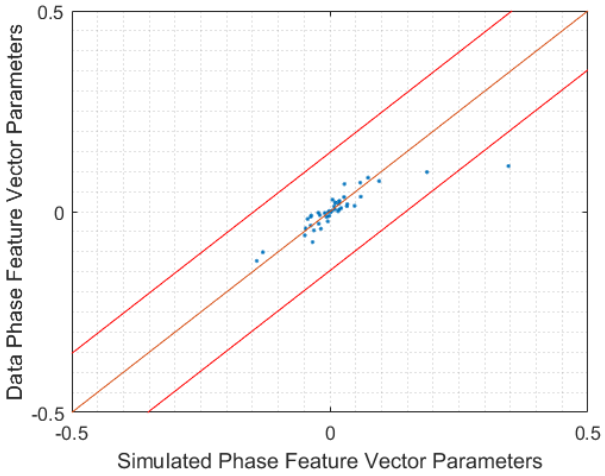

(b)

Figure 4.6: Validation of the model using Chebyshev decomposition and comparison of resulting feature vectors representing data from the experiment and model. Magnitude data (a) and phase data (b) have been separately validated. All data points except one lie within the error bounds. The point that is outside the bounds corresponds to the first Chebyshev polynomial, which is a constant offset. As the phase angle can be rotated freely within between $-\pi < \theta < \pi$, equivalent to an offset without changing the form or shape of the data, this does not make the model invalid.

Figure 4.6 demonstrates the validity in describing the phase image generated by a stress distribution. This somewhat contradicts the findings of Diaz et al [64] and Patki & Patterson

[67] as it suggests that a purely elastic stress distribution will generate a phase image similar to those that have been linked with plasticity.

Key differences between the specimens used could explain the difference in results. Diaz et al [64] used single edge notched (SEN) steel specimens, whereas Patki & Patterson [67] used aluminium CT specimens. In both cases, the specimens used were significantly larger and thicker than those used in this work.

The model demonstrates that conduction of a sinusoidal heat source produces a characteristic distribution of phase difference between the load and temperature signals. In the model, the elastic stress field was the source of heat, however plastic work could also be a heat source due to dislocation motion, as hypothesised by Diaz et al and Patki & Patterson.

It is reasonable to conclude that the model suggests that for small geometry, thin, stainless steel CT specimens used in this work that any plasticity effects on the phase data are being overwhelmed by the effect of thermal conduction.

4.3 Second Harmonic

If, as the finite element model outlined in section 4.2 suggests, the phase method does not produce reliable results for the plastic zone in austenitic stainless steels, a new method must be found to measure plasticity.

For some time there has been interest in the second harmonic of the thermal output of a cyclically loaded specimen for: residual stress measurement [107][108][109]; fatigue limit measurement [110]; energy dissipation [111][112] [113] [68]; and plasticity [69]. A theoretical basis for the appearance of plasticity effects in the second harmonic data has been attempted by Enke [111] and Palumbo [68].

Thermoelastic Effect

Wong et al [114] and Enke [111] both investigated the theoretical foundation of the thermoelastic equation, a simplified version of which is given by equation (3.1). Wong et al were motivated by observed variations in the thermoelastic constant at different loading conditions and Enke was attempting to capture non-linear temperature effects. Both authors derived an improved version of the equation by removing the assumptions that the mechanical and thermal properties, such as Young's modulus, E, are temperature independent. Both authors arrived at an equation of the same form, which had both first harmonic (loading frequency) and second harmonic (twice the loading frequency) components.

For example, Wong et al showed that the thermoelastic response of a material loaded uniaxially with an applied stress of the form $\sigma = \sigma_m + \sigma_a \sin \omega t$ is:

$$\rho_0 C_\epsilon \frac{\delta T}{T_0} = -\left(\alpha - \frac{1}{E^2}\frac{\partial E}{\partial T}\sigma_m\right)\sigma_a \sin \omega t - \frac{1}{4E^2}\frac{\partial E}{\partial T}\left(\sigma_a\right)^2 \cos 2\omega t \qquad (4.7)$$

where: ρ_0 is the density, C_ϵ is the specific heat at constant strain, δT is the thermoelastic temperature change, T_0 is the absolute temperature, α is the coefficient of thermal expansion, E is Young's modulus and $\frac{\partial E}{\partial T}$ is the change of Young's modulus with temperature.

In a later study, Wong et al [107] measured the first and second harmonic responses of a titanium alloy specimen at zero mean load and demonstrated that the stress dependence predicted by equation (4.7) was correct.

For this work, equation (4.7) has two important features that must be considered: firstly that the first harmonic component has a dependence on mean stress; and, secondly, that a second harmonic component exists. However, the magnitude of these effects is small, with the theoretical value of $\frac{1}{E^2}\frac{\partial E}{\partial T} = -1.58 \times 10^{-9}\mathrm{KMPa}^{-1}$, compared to the value of $\alpha = 17.3 \times 10^{-6}\mathrm{K}^{-1}$.

As an example of the difference in magnitude of these effects, consider the worst case

scenario where a specimen is cyclically loaded at zero mean load, with an amplitude equal to the yield stress. For the 304 stainless steel used in this project, this would give $\sigma_a = 225$MPa. Equation (4.7) gives the first harmonic (a) and second harmonic (b) components and their ratio as:

$$a = -\alpha\sigma_a \tag{4.8}$$

$$b = -\frac{1}{4E^2}\frac{\partial E}{\partial T}(\sigma_a)^2 \tag{4.9}$$

$$\frac{b}{a} = \frac{1}{\alpha 4E^2}\frac{\partial E}{\partial T}\sigma_a \tag{4.10}$$

and therefore, for $\sigma_a = 225$MPa, $\frac{b}{a} = 0.005$, two orders of magnitude smaller. The picture becomes somewhat more complicated for the two-dimensional case, when the load is no longer uniaxial. However, it is still not expected that the second harmonic thermoelastic effect will have a significant effect.

Plastic Effects

In addition to thermoelastic effects, the work by Enke [111] considered the effect of irreversible temperature changes due to plastic work. Enke considered the hysteresis loop of a cyclically loaded material and hypothesised that plastic work would appear as a second harmonic effect, due to the accumulation of plastic work during both loading and unloading during a single load cycle. Enke propose that plastic effects would generate a signal of the following form:

$$S_{\text{irrev}(t)} = S^a(2\omega)\sin(2\omega t + \phi_2) + S^a(4\omega)\sin(4\omega t + \phi_4) + ... \tag{4.11}$$

where: $S_{\text{irrev}(t)}$ is the detector output due to irreversible temperature changes, $S^a(n\omega)$ are coefficients determined by the amount of plastic work, ω is the angular frequency, t is time and ϕ_n are phase shifts.

Further, Enke demonstrated that the second harmonic component of equation (4.11), $S^a(2\omega)$, was proportional to the amount of plastic work occurring within the specimen.

Second Harmonic TSA Data

The second harmonic response of a specimen can be easily measured using a TSA system by altering the frequency of the reference signal to be twice that of the loading. All of the signal processing outlined in section 3.2.2 remains the same, but the output is the magnitude and phase of the thermal response at twice the loading frequency.

A short paper by Sakagami et al [69] noted that there is a localised increase in the second harmonic response of a specimen containing a hole that only occurs when the yield stress is exceeded. The authors associated this with plastic behaviour, similar to a crack tip plastic zone. Yet, until recently, little attention has been paid to the second harmonic response of specimens containing cracks. Palumbo et al [68] used the second harmonic response at the crack tip to calculate energy dissipation associated with plastic work, using a similar arguement to Enke [111].

Figure 4.7 shows data collected at both the first and second harmonic of the loading frequency for a 304 stainless steel specimen containing a 5.9mm crack. Using the insights given by Wong et al [114], Enke [111] and Sakagami et al [69], a physical interpretation of the second harmonic behaviour of cracked specimens has been attempted.

It is argued that the 'hot-spot' that can be seen in the second harmonic X-data, figure 4.7 (b) is the plastic zone as it exhibits a strong, localised signal in the vicinity of the crack tip. It is unlikely to be associated with the second harmonic thermoelastic response, given in equation (4.7) for several reasons: the size of the signal is large compared to the expected response; the spatial distribution of the signal is not equivalent to square of the first harmonic distribution, the maxima are also not coincident; and the signal appears in the X-image, not

the Y-image as would be expected. In addition to eliminating the thermoelastic explanation, the 'hot-spot' shows similarities with the behaviour predicted by Enke and observations of Sakagami et al: it appears in the X-image, which would be the case if ϕ_2 were small in equation (4.11); and, it is localised to the vicinity of the crack tip.

The above should not be taken to mean there is no second harmonic thermoelastic response observed. The second harmonic Y-image, figure 4.7 (d), has features which could tentatively be associated with thermoelastic behaviour. Excluding the negative region near the crack tip, which is assumed to be caused by conduction of the plastic zone heat source, there is a slight positive signal that potentially has a similar distribution to the first harmonic X-image figure 4.7 (a). The size of the this positive signal is very small; and, therefore likely within the noise limit of the TSA system.

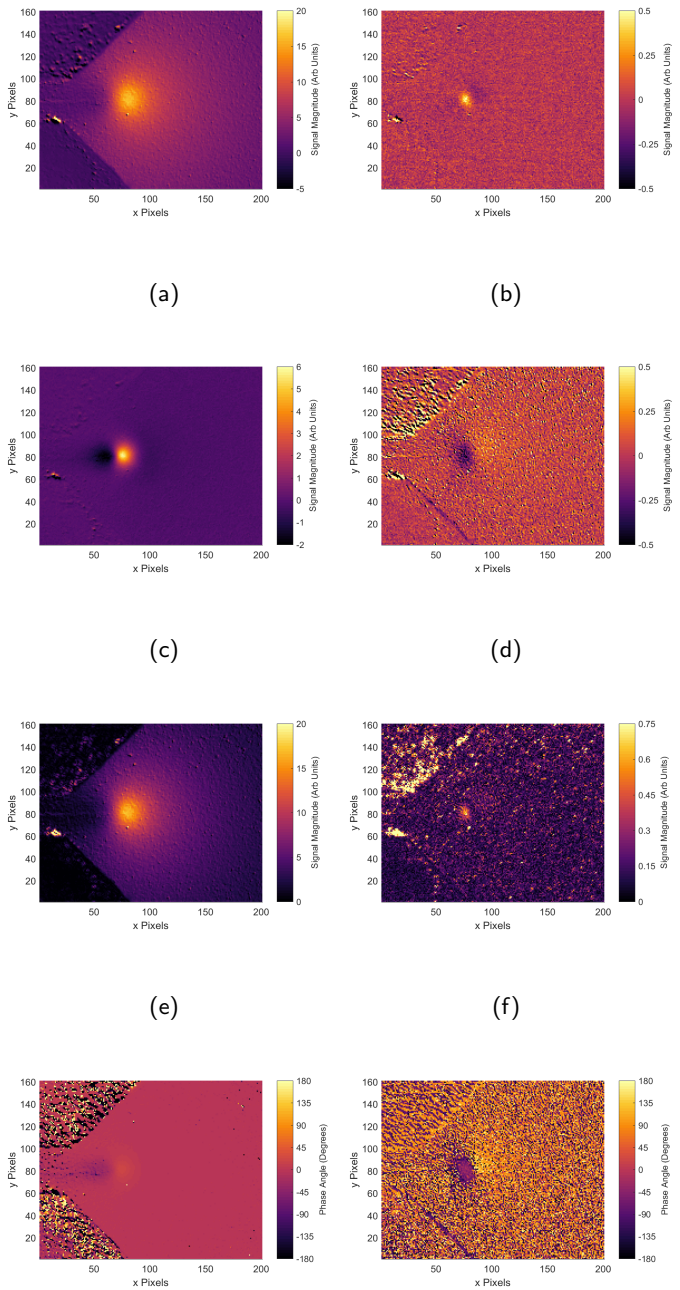

Figure 4.7: First harmonic (loading frequency) thermoelastic data (left) and second harmonic data (right) for a specimen with a 5.9mm crack, showing the X-images (a),(b); Y-images (c),(d); R-images (e),(f); and the θ-images (g),(h). Noisy regions in the left corners are the grips. The crack tip is located at $(76, 80)$.

4.3.1 Second Harmonic Method for Plastic Zone Measurement

In order to obtain the size of the plastic zone 'hot-spot' feature, post processing is necessary. Following the approach taken by Patki & Patterson [67] to identify the region of phase change, a threshold method was employed.

The threshold value was determined by the standard deviation of signal in the far-field region away from the crack tip. Initially, this was calculated for each data set during the post-processing procedure, but this was time consuming and varied as the crack tip approached the region used for the calculation. Ultimately, the standard deviation of the signal in the far-field for a specimen with a short crack (4mm) was used as a constant, resulting in a threshold of > 0.07 camera units.In order to reduce the noise on the thresholded data, a Gaussian filter was applied before the threshold.

Identification of the plastic zone was performed by applying a hole-filling algorithm to the thresholded data. This procedure eliminates any groups of pixels in the data that are away from the identified plastic zone, such as those caused by the noise signal associated with the grips.

Radius and area measurements were performed on the final binary image produced by the thresholding and hole-filling procedure. Plastic zone radius was measured by counting the number of pixels with a non-zero value along the pixel row that had been identified as containing the crack tip by FATCAT, see section 3.2.5. Area was measured by counting the number of non-zero valued pixels in the binary image. The pixel values were then scaled, using 0.0332mm/px and 0.0011mm^2/px for radius and area respectively.

4.3.2 Plastic Zone Observations

Using the second harmonic method outlined above, it was possible to assess the behaviour of the identified plastic zone throughout a crack growth test. Figure 4.8 shows a comparison

of both the phase method and the second harmonic method for measuring the plastic zone area on the data for a single specimen over the duration of a crack growth test. The specimen was loaded with 450 ± 150N at 20Hz. Over the test the crack length grew from 4mm to 8.3mm. The test was ended before the specimen failed. It can be seen that the plastic zone area measured using the second harmonic method behaved more similarly to the theoretical prediction of a circular plastic zone with a diameter equal to Irwin's plastic zone correction, also used in figure 4.2.

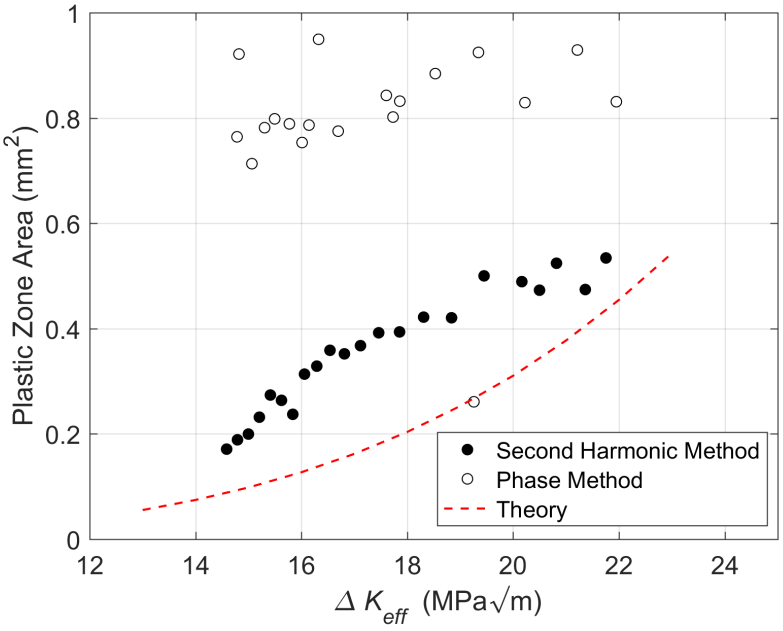

Figure 4.8: Plastic zone area obtained using the phase method (open symbols) and area of the second harmonic hot-spot (closed symbols) for a 304 stainless steel specimen loaded sinusoidally with 450 ± 150N at 20Hz.

In addition to the measured plastic zone behaviour over a period of crack growth, it was necessary to test the frequency dependence of the second harmonic method. A test was performed on a 304 stainless steel specimen containing a 4.7mm crack, loaded with 450 ± 150N at increasing loading frequencies. Figure 4.9 shows that there does not appear to be a strong frequency dependence to the second harmonic method. This is unlike the

phase method, which showed a decrease in the measured area as frequency increased, shown in figure 4.3. It is hypothesised that this is due to the reduced thermal diffusion length, u, of a higher frequency temperature source. For example, equation (4.1) predicts that u for a second harmonic temperature source will be a factor of $1/\sqrt{2}$ smaller than u for a temperature source at the loading frequency.

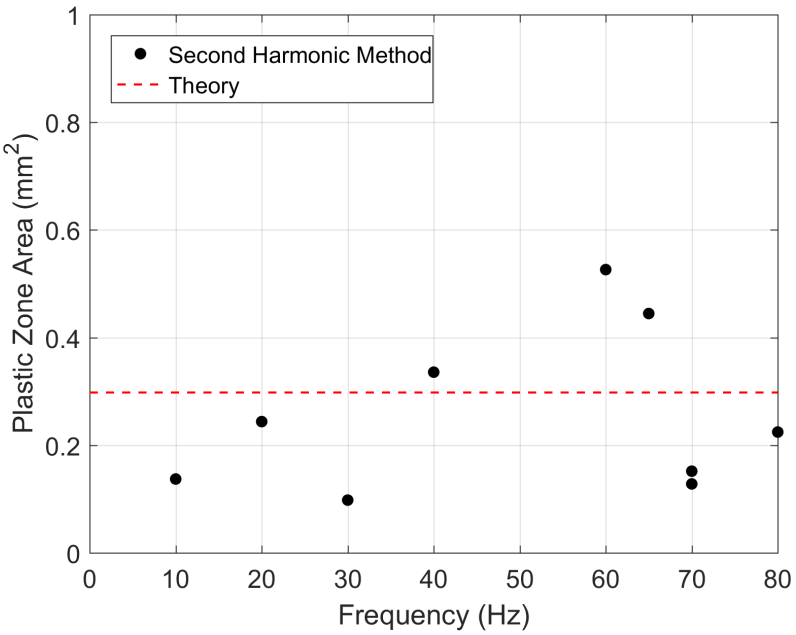

Figure 4.9: Plastic zone area obtained using the second harmonic for a specimen with a ≈ 4.7*mm crack at various frequencies.*

4.3.3 Crack Closure Observations

It has been established in the literature that the stress intensity factor calculated from TSA data collected at the loading frequency is the effective stress intensity factor range ΔK_{eff} and is therefore sensitive to closure effects. Early results suggested closure also caused changes in the data collected at the second harmonic of the loading frequency, as new features were apparent behind the crack tip, closer to the notch.

A test was performed to determine if these features were related to closure. A specimen was cyclically loaded, where the load amplitude was held constant at 150N and the mean

load decreased in steps from 450 to 175N, corresponding to a change in R-ratio from 0.5 to 0.07. Data captures at both the first and second harmonic were collected at each R-ratio step.

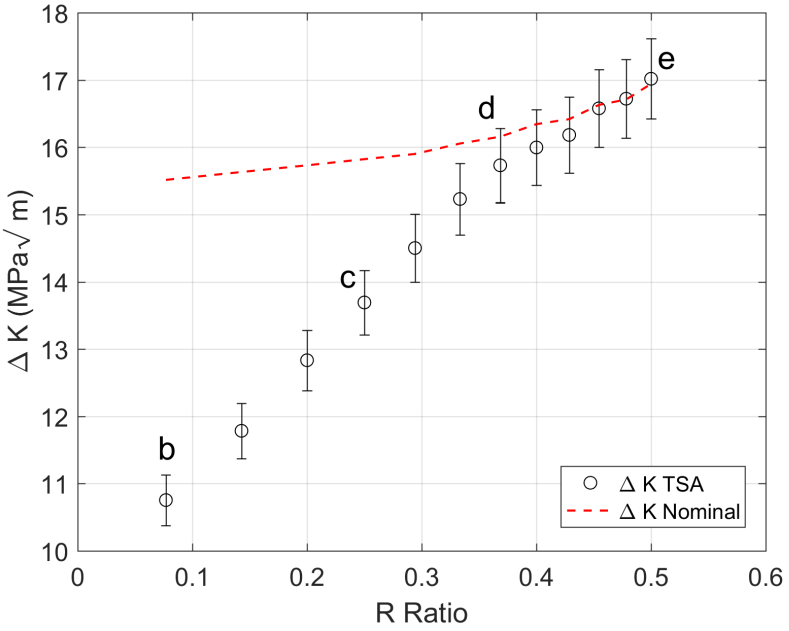

(a)

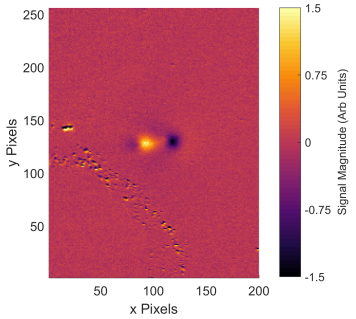

(b)

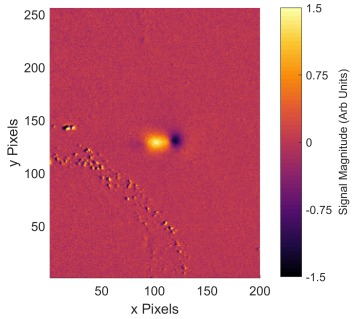

(c)

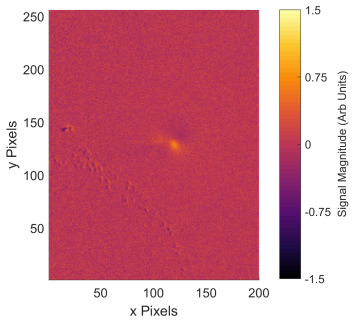

(d)

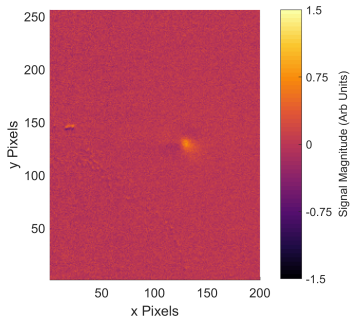

(e)

Figure 4.10: Change in stress intensity factor (a) and second harmonic X-image with R-ratio for: $R = 0.08$ *(b),* $R = 0.25$ *(c),* $R = 0.37$ *(d) and* $R = 0.50$ *(e). The crack tip is located at approximately pixel* $(130, 125)$

Figure 4.10 a) shows a reduction in effective stress intensity factor range, measured using FATCAT. Below $R = 0.45$ there is a change in the gradient and the measured ΔK_{eff} begins to diverge from the nominal value, broadly in agreement with the findings of Ohta et al [115] who found that closure occurs in 304 stainless steel when $R \leq 0.4$. Figure 4.10 b) to e) shows the second harmonic X-image for various R-values along the scale shown in a). A elongated bright region along the crack flanks appears in b) and c), which disappears at the same R-ratio that closure is seen to cease, i.e. (d).

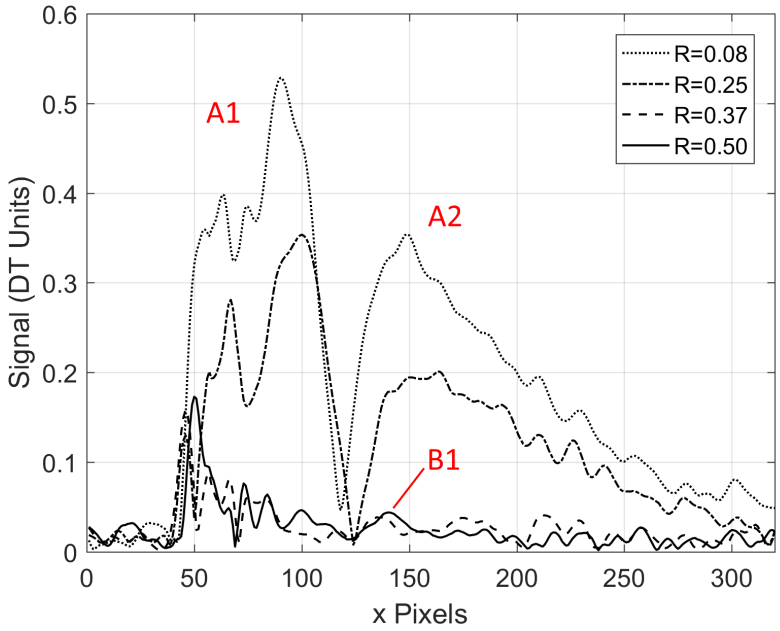

Figure 4.11: Second harmonic signal magnitude (R), in camera units, along the crack path, measured in pixels from the notch, corresponding to the R-ratios shown in figure 4.10 b) to e). Peaks A1 and A2 have been labelled as per Palumbo et al [68], peak B1 corresponds to the hot-spots in figure 4.10 d) and e).

Figure 4.11 shows the same features that Palumbo et al [68] identified. The authors argued, reasonably, in the absence of data to the contrary, that peak A1 corresponds to crack flank effects and peak A2 corresponds to plastic zone effects. However, as both figures 4.10 and 4.11 demonstrate, both peaks A1 and A2 arise as a consequence of closure. The

peak labelled B1 is the hot-spot that has been identified as the plastic zone from previous observations and is overwhelmed by the larger effect of closure.

In agreement with Palumbo et al, it is hypothesised that the peak A1 could be caused by either crack face friction caused by the rubbing of asperities during the crack opening and closing during the load cycle or a thermoelastic effect generated by the contact of the crack faces. These have not been demonstrated and both effects could be contributing depending on the crack path geometry.

It is unclear what the source of the peak A2 is. It does not appear, other than during closure, and its magnitude is large and related to the R-ratio. Peak A2 occurs 180° out-of-phase from peak A1, which would suggest it was related to an effect during loading, rather than crack flank contact during the unloading portion of the load cycle. Due to this behaviour, it is unlikely to be related to the plastic zone.

The presence of these features in the second harmonic appear to be caused by closure and provide a simple qualitative test to detect closure.

4.3.4 Method Demonstration

Figure 4.12 shows the results of both the phase method and the second harmonic method applied to data collected for five specimens. Each specimen was subjected to a fatigue crack growth test at 20Hz with a load of 450 ± 150N. Data was collected at the loading frequency and second harmonic for each specimen, meaning both methods were measuring the same plastic zone over the test duration.

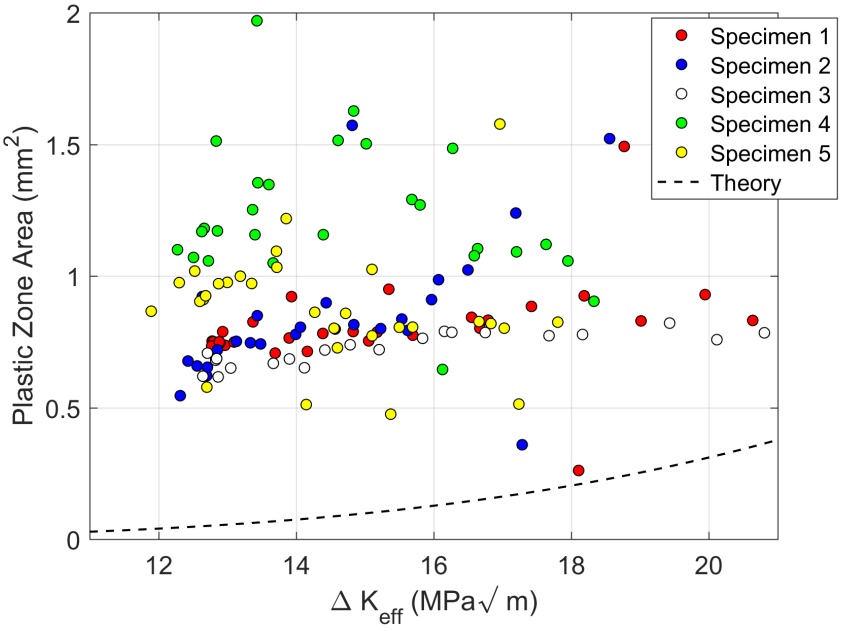

(a)

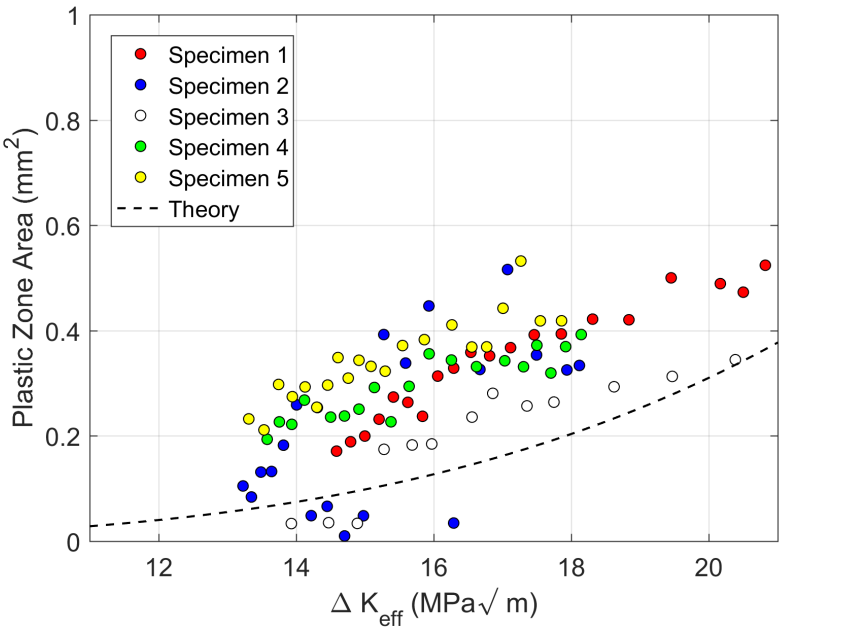

(b)

Figure 4.12: Plastic zone area obtained using the phase method (a) and second harmonic method (b). Data was collected at both the first and second harmonic for the five specimens, allowing both methods to be applied. Theoretical cyclic plastic zone area given by a circle with diameter equal to Irwin's plastic zone correction.

It is clear from figure 4.12 that the second harmonic method, outlined in section 4.3.1, gives results that agree more closely with theory. Additionally, the results of the second harmonic method shows less scatter and a much stronger increasing trend with stress intensity factor.

4.4 Dissipated Energy Analysis

Following a similar approach to Palumbo et al [68] and Shiozawa et al [116], it is possible to determine the change in internal energy in the plastic zone due to the second harmonic temperature changes using the following relation:

$$\Delta U = \rho V C_p \Delta T \tag{4.12}$$

where: ΔU is the increase in energy, ρ is the material density, V is the volume of material effected by the change in temperature ΔT,and C_p is the heat capacity at constant pressure.

Palumbo et al [68] used a version of this equation to calculate the dissipated energy per unit volume and used the maximum second harmonic temperature as ΔT. They assumed this temperature occurred over a volume equal to Irwin's plastic zone correction through the thickness of the specimen. This energy is considered dissipated, as, unlike the thermoelastic temperature changes associated with the elastic field, the temperature changes associated with plastic work are not thermodynamically reversible.

With the technique outlined in section 4.3.1, it is possible to obtain an estimate of the plastic zone area directly, and hence not rely on theory. Additionally, the second harmonic temperature change across the plastic zone is not uniform, an assumption which could introduce uncertainties.

Equation (4.12) can be modified to use the richness of data in the second harmonic as follows:

$$U = \sum \rho C_p V \Delta T \tag{4.13}$$

$$\Delta T = A_T \Delta S \tag{4.14}$$

$$V = l_{px}^2 B \tag{4.15}$$

where: U is the total change in internal energy in the plastic zone; equivalent to total dissipated energy, ΔT is the temperature change occurring at each pixel within the plastic zone, V is the volume of a one by one pixel element through the thickness of the specimen, ΔS is the raw second harmonic signal, A_T is a calibration factor to convert from camera units to Kelvin, l_{px} is the pixel resolution and B the specimen thickness. The equation calculates the dissipated energy at each pixel within the plastic zone and the summation gives the total dissipated energy for the entire plastic zone.

In the definition of V an assumption is made that the plastic zone is the same shape throughout the thickness, which is not strictly the case as a higher constraint inside the specimen will result in a smaller plastic zone, however due to the relatively small thickness of the specimens this effect is not likely to be large.

By dividing the result of (4.14) by the number of cycles in the accumulation time of each data capture it is possible to calculate the energy dissipated in the plastic zone per load cycle.

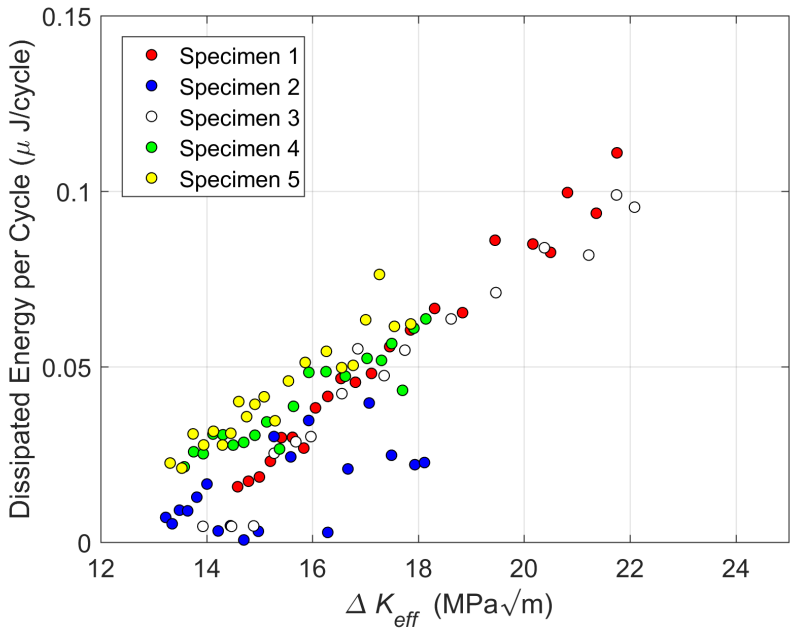

Figure 4.13: Dissipated energy from the plastic zone per cycle, calculated using (4.14) *for the same specimens used in figure 4.12.*

Note that the quantities shown in figure 4.13 are much lower than those calculated by Palumbo et al [68], however there are significant differences between the experiments that could explain this. Palumbo et al used CT specimens approximately four times larger in-plane and thirteen times thicker, which results in a larger volume of material at the crack tip. Additionally, the specimens were produced from high strength martensitic steel, in which dislocation motion is more difficult. However, it would be expected that when the dislocations do move, as in the plastic zone, the amount of energy dissipated would be larger due to this difficulty. The load range used was also seventy times larger, putting more energy into the specimen in general.

4.5 Discussion

It is clear from figures 4.12 that the second harmonic method gives results that are closer to the theoretical plastic zone behaviour.

Despite the apparent improvement relative to the phase method, there is still substantial variation between specimens. Due to the small magnitude of the second harmonic effects, they are more sensitive to the noise level in the experiment. This could be influenced by surface finish, surface emissivity, experimental temperature, specimen motion or out-of-plane motion.

A further important caveat relates to the effects of closure on the second harmonic signal. Figure 4.10 demonstrates that the signal that is suspected to be generated by crack face contact or crack face friction is a much larger effect than plasticity and in effect overwhelms the signal from the plastic zone. This would represent a potentially significant drawback in the applicability of this method to certain materials and R-ratios where closure is likely.

The dissipated energy per cycle shown in figure 4.13 agrees more closely between specimens than the area shown in figure 4.12. The data for all specimens can be fitted with a linear model ($R^2 = 0.769$). It is well attested in the literature [68] [117] [118] that the the energy dissipated per cycle has the form:

$$q = n\Delta K^4 \tag{4.16}$$

which fits the data shown equally well ($R^2 = 0.755$).

Despite the relative success, a complete understanding of the second harmonic is not claimed, this is currently an open question in the literature with work by Bär and Urbanek [119], Palumbo et al [68] and Shiozawi et al [116] attempting to understand and utilise the second harmonic effect.

4.6 Conclusions

The phase method, when applied to the 304 stainless steel specimens used in this research, produced inconsistent results that did not agree with theory. Finite element modelling

suggested that the main source of the thermoelastic phase shift is conduction caused by the large gradients of the elastic stress field near to the crack tip.

Measurement of the hot-spot that appears near the crack tip in the second harmonic X-data provides a more reasonable approximation of plastic zone area and behaviour as ΔK_{eff} increases. However, when closure occurs, the larger signal generated from crack flank contact overwhelms and effectively obscures the plastic zone signal, somewhat restricting the applicability of the technique.

The features that that arise behind the crack tip in the second harmonic X-image are useful for providing a simple binary test for closure, without the difficulty of performing a test at a range of R-ratios.

Importantly, the second harmonic does not require any additional hardware or necessitate a change in measurement technique. A change in software settings is all that is required to change between regular TSA, using the data associated with the first harmonic frequency, and data capture at the second harmonic frequency. This allows the retention of benefits of TSA for this study: direct measurement of surface stress, ease of surface preparation and measurement without having to pause testing.

Chapter 5

Results & Discussion

This chapter presents the design, procedure and results of the main fatigue crack growth testing program. ANCOVA is used to determine if the effects of irradiation on the crack growth rate behaviour are significant. Analysis of the change in hardness, plastic zone area and plastic zone dissipated energy are performed. The results of a smaller follow up test are also presented, demonstrating qualitatively some of the effects observed in the main tests.

5.1 Effect of Proton Irradiation on Fatigue Crack Behaviour

5.1.1 Objectives

The main objective of this experimental program was to determine if there is a measurable effect of proton irradiation on the fatigue crack growth behaviour of 304 stainless steel compact tension specimens. This was achieved by testing several unirradiated specimens and comparing their behaviour to specimens irradiated to increasingly high levels of damage. A number of temperature control specimens were also tested as controls for the effects of mounting and heating the specimens in the irradiation target stage.

Fatigue crack growth behaviour was quantified by fitting the crack growth rate against

stress intensity factor data with the Paris Law for each damage level and performing statistical tests to determine the significance of the difference between damage levels.

Previous studies have used thin specimens (≈ 0.15mm), with high proton energies of 18MeV, achieving full thickness irradiation. This study however, tested thicker specimens, at 0.8mm, with lower proton energies. This allows specimens to be closer to the size requirements for standards such as ASTM E-647 [20], but meant the irradiation damage was only a surface effect. Lower beam energies also reduced activation from proton capture reactions, allowing for testing in a standard mechanical testing laboratory after only a short cooling period.

Measurements of the irradiated specimens using thermoelastic stress analysis has not been previously attempted and allowed for direct measurement of the surface stresses, calculation of the effective stress intensity factor, plastic zone size, and crack tip position. TSA captures data live during a test and does not require any pauses, holds or unloading which could introduce additional uncertainty.

The increase in hardness caused by radiation damage has been implicated in the change of fatigue crack growth behaviour in the literature. Microhardness testing was performed to locate the irradiation damage and assess the relative hardness increase. Plastic zone size is dependent on the yield stress which was expected to increase as hardness increased. This was tested by measuring the plastic zone size over the course of crack growth.

5.1.2 Experiment Design

CT specimens for testing were prepared following the procedure outlined in section 3.1. The main method of the tests was as follows:

1. Specimens were prepared and then precracked.

2. (Optional) Specimens were subjected to irradiation damage.

3. Fatigue crack growth tests were performed, observed by a TSA system.

4. Stress intensity factors were calculated from TSA data and a fit to the Paris law was performed.

5. Plastic zone size was determined using the second harmonic method.

6. Total dissipated energy per cycle from the plastic zone was calculated.

7. Microhardness tests were performed to locate the edge of the irradiated area.

8. A comparison of the behaviour of unirradiated and irradiated specimens was performed.

Irradiated Specimens

Specimens were irradiated using the BABY accelerator at DCF, following the procedure outlined in section 3. Damage levels were chosen based on two considerations: firstly, reasonable end-of-life damage, such as those given by Little [2] for austenitic stainless steel components of the core internals, which range from $\approx 1-10$ DPA depending on the location of the component. Secondly, what damage levels were achievable in a single shift, given that overnight operation was not possible.

Another consideration was damage rate: increasing the beam current increased the damage rate, allowing for more damage during a given time, but generated more heating in the specimen and deviated further from neutron-like conditions. Previous work by Was et al [86] found that the end-state of proton damage rates of 7×10^{-6}DPA/s still compared favourably to neutron damage when considering segregation behaviour, microstructure and hardness changes.

Following the work of Was et al [86], an irradiation temperature of 360°C was chosen as this resulted in a damage end-state that closely matched neutron irradiation at reactor temperatures.

The choice of beam energy was also important. A higher beam energy generated a deeper damage profile in the target, which would be preferable. However, the cross section for the production of Co^{57} via proton capture of Fe^{56} increased around 2MeV [120]. Co^{57} has a 272 day half-life, which would have made the specimens active for a long time, resulting in a delay in mechanical testing. After a trial run at 2MeV, which resulted in a relatively long cooling time, an energy of 1.6MeV was chosen for all future experiments. This gave a cooling time of approximately 6 weeks for the specimens to return to the background radiation levels.

Table 5.1: Planned parameters used for the accelerator and end-station during irradiation experiments.

Parameter	Chosen Value
Beam Energy	1.6MeV
Beam Current	30μA
Temperature	360°C

Due to the time consuming task of specimen changeover, irradiation experiments were planned to alternate between shorter and longer runs. For example, a short day would consist of specimen mounting, a short run ≤ 4hours, specimen removal and remounting of the next specimen, in preparation for the next day. This meant that every other day a long run could be performed with the most time possible, typically up to 8 hours.

The fatigue crack growth behaviour of even nominally identical specimens can differ, it was therefore important to test enough specimens to acquire robust data. 6 specimens were planned at each irradiation damage level.

Table 5.2: Monitoring data obtained from the end-station control computer for each irradiated specimen.

Specimen	Accumulated Charge (C)	Irradiation Time (hours)	Ion Fluence ($\times 10^{18}$ions/cm^2)	Beam Current (μA, average)	DPA Bragg Peak (DPA at $13.2\mu m$)	Temperature (°C, average)	Temperature (°C, maximum)
R5	0.216	3.50	1.35	27.3	0.94	353.01	613.97
T5	0.216	3.03	1.35	26.9	0.94	349.54	384.54
V5	0.216	2.65	1.35	28.2	0.94	354.48	364.88
AO5	0.216	2.97	1.35	26.7	0.94	358.70	395.65
S	0.22	5.28	1.38	12.3	0.94	347.66	481.15
U	0.279	2.86	1.74	27.1	0.94	334.07	368.24
AB5	0.431	4.11	2.69	29.6	1.87	360.25	373.92
Y5	0.432	6.81	2.70	26.1	1.87	351.07	367.75
AS5	0.432	4.56	2.70	29.2	1.87	360.50	367.85
AU5	0.432	4.5	2.70	29.8	1.87	361.20	372.92

Table 5.3: Monitoring data obtained from the end-station control computer for each irradiated specimen.

Specimen	Accumulated Charge (C)	Irradiation Time (hours)	Ion Fluence ($\times 10^{18}$ions/cm^2)	Beam Current (μA, average)	DPA Bragg Peak (DPA at $13.2\mu m$)	Temperature (°C, average)	Temperature (°C, maximum)
T	0.648	6.31	4.05	28.6	2.81	350.44	448.83
V	0.648	7.14	4.05	29.4	2.81	356.07	365.85
M5	0.648	7.28	4.05	29.0	2.81	358.42	383.40
N5	0.648	7.75	4.05	29.9	2.81	356.71	494.62
P5	0.648	7.17	4.05	25.6	2.81	364.18	386.31
Q5	0.648	7.11	4.05	29.2	2.81	357.93	368.63
S5	0.864	8.86	5.40	30.1	3.76	357.26	365.82
W5	0.864	8.69	5.40	29.8	3.76	358.41	389.29
Z5	0.864	9.03	5.40	29.3	3.76	359.55	399.85
AC5	0.864	8.14	5.40	30.0	3.76	359.81	372.20
AR5	0.864	8.75	5.40	30.2	3.76	360.37	371.26
AT5	0.864	8.72	5.40	30.1	3.76	360.55	373.20

Note that some specimens saw a very high maximum temperature for a short period of time. This was caused by the indium used in the lower shim re-solidifying during the experiment. When this happened, the thermal contact between the specimen and cooling loop was severed, causing a rapid rise in specimen temperature. In experiments where this occurred, the beam current had to be reduced from the planned 30μA to prevent overheating. In later experiments, the lower shim was replaced with a eutectic paste, which eliminated this problem. Possible effects of these temperature transients are discussed further in section 5.1.3.

Due to the difficulties encountered in operation of the accelerator it was not always possible to complete some irradiations. Hence, the reduced number of specimens irradiated at 2.70×10^{18}protons/cm^2 compared to the other damage levels.

Control Specimens

In addition to the radiation damage, the irradiated specimens were also held at 360°C for a number of hours and are in contact with liquid indium during this time. Theoretically, this should not cause any issues as the temperature needs to be higher (550°C), and for much longer, to generate any changes in the austenitic steel. Indium can potentially cause liquid metal embrittlement when part of a eutectic is applied to stainless steel; however, little evidence exists for an effect with pure liquid indium.

To mitigate against these effects, 2 control specimens have been utilised. These were mounted following an identical procedure to the irradiated specimens and heated in the end-station under vacuum to 360°C and held for 2 hours and 8 hours. These times correspond to the shortest and longest irradiation times respectively.

5.1.3 Closure Observations

When fatigue crack growth testing some of the specimens that had seen the high temperature excursions, there were instances of closure noted. The closure occurred as the crack traversed the boundary between the unirradiated and irradiated material $4-5$mm from the notch. This appeared in both the stress intensity factor data and as an increase in the crack flank signal in the second harmonic images.

In particular, specimens S and T exhibited closure for a long duration into the test. Crack flank signals were observed in the second harmonic and a reduction in ΔK_{eff} was seen in the standard TSA data, shown in figures 5.1 and 5.2.

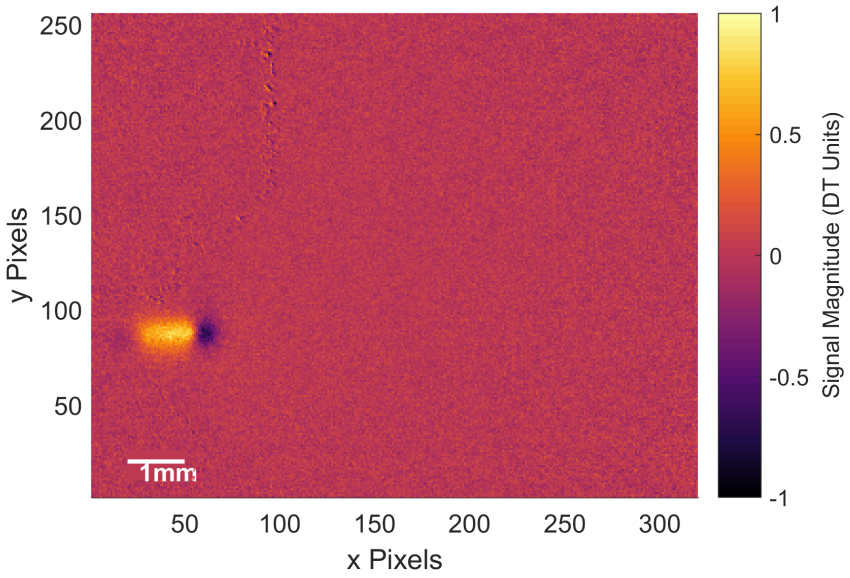

Figure 5.1: Second harmonic X-image of specimen S, irradiated to 1.38×10^{18}protons/cm^2. *The crack length is approximately* 4.7*mm, with the crack tip located at pixel (53,88). The crack flanks show the same positive signal that was found to be associated with closure in section 4.3.3.*

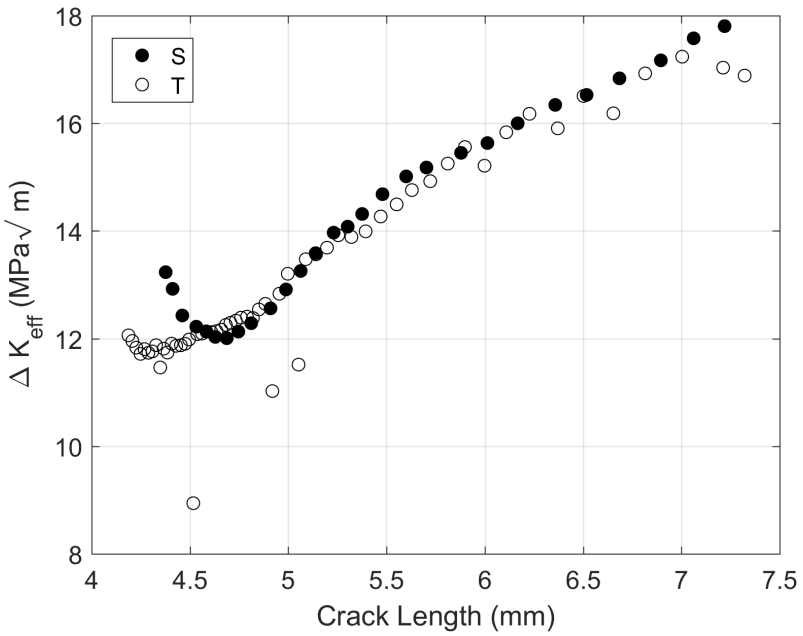

Figure 5.2: Effective stress intensity factor for S (filled symbols) and T (empty symbols). A change in gradient of ΔK_{eff} is observed around ≈ 5.1mm in both specimens.

Figure 5.1 shows an example of the strong crack flank signal that appeared in the second harmonic data. These signals were observed up until ≈ 5.3mm in S and ≈ 5.1mm in T. The stress intensity factor data shown in figure 5.2 also indicates closure, with a distinct change in gradient of the effective stress intensity factor below the above crack lengths. As this was in the window in which the analysis of the Paris Law was to be conducted, these specimens were omitted from the analysis.

The closure effect seems to correlate with the temperature transients, as specimens S and T both experienced high temperatures at the start of the irradiation experiment due to indium re-solidification. This may not be the full explanation as specimen R5 experienced a particularly large transient, but did not experience closure. Due to the complexity of the mounting procedure, it is possible that S and T were clamped tighter and thus caused a high thermal stress as their expansion was more constrained.

5.1.4 Microhardness Tests

The microhardness procedure outlined in section 3.4 was performed for the irradiated specimens.

An example of the data and fits for two specimens, S and AB5 irradiated to a proton fluence of $1.35 \times 10^{18}\mathrm{cm}^{-2}$ and $2.70 \times 10^{18}\mathrm{cm}^{-2}$ respectively are given in figure 5.3.

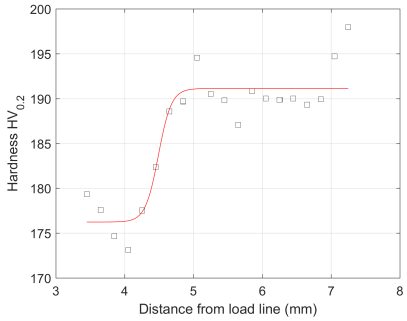

(a)

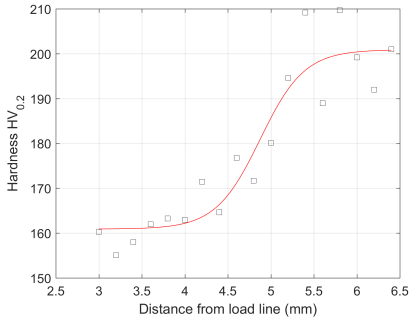

(b)

Figure 5.3: Hardness data increase for a specimen irradiated to a fluence of $1.35 \times 10^{18}\mathrm{cm}^{-2}$ *(a) and* $2.70 \times 10^{18}\mathrm{cm}^{-2}$ *(b). Fit parameters are given in table 5.4.*

Table 5.4: Fit parameters of the microhardness profile data fits with equation (3.16).

Specimen	Ion Fluence ($\times 10^{18}$ions/cm^2)	H_0 (HV$_{0.2}$)	H_I (HV$_{0.2}$)	s	x_I (mm)	R^2	RMSE (HV$_{0.2}$)
S	1.35	176.2	14.9	10.57	4.49	0.8646	2.80
U	1.35	178.7	17.2	63.3	4.70	0.7036	6.31
R5	1.35	162.2	18.5	6.922	4.68	0.8228	4.43
T5	1.35	157.1	25.2	4.907	3.73	0.8772	3.92
V5	1.35	151.7	39.6	0.5012	4.52	0.9015	1.96
AO5	1.35	171.1	25.6	2.231	4.55	0.8264	4.78
AB5	2.70	160.9	40.0	3.882	4.88	0.8855	6.85
Y5	2.70	163.9	33.3	110.2	4.40	0.8762	6.96
AS5	2.70	164.1	34.7	8.143	4.76	0.6837	12.38
AU5	2.70	165.1	30.7	5.998	4.32	0.7359	9.01
T	4.05	179.1	47.5	11.95	4.86	0.9508	5.82
V	4.05	180.1	51.4	77.04	3.58	0.9146	6.41
M5	4.05	170.3	35.7	3.592	4.72	0.7382	10.58
P5	4.05	168.7	49.1	7.005	3.93	0.885	7.98
Q5	4.05	172.4	38.1	13.3	4.78	0.8942	7.16
S5	5.40	167.0	53.7	10.58	5.14	0.8962	9.59
W5	5.40	161.4	16.8	5.59	5.22	0.6558	5.97
Z5	5.40	167.4	61.4	1.938	5.22	0.912	7.18
AC5	5.40	160.4	41.8	4.059	4.86	0.9255	5.90
AR5	5.40	164.2	50.5	3.797	4.77	0.9270	6.78
AT5	5.40	165.1	51.8	6.363	3.87	0.8979	7.59

Based on the microhardness testing, specimen W5 will be excluded from further analysis. Table 5.4 shows that the hardness increase for W5 was much smaller than other specimens irradiated to 5.40×10^{18}protons/cm^2 and the sigmoid fit was particularly bad ($R = 0.6558$). It is suspected that there was a misalignment of the vanes during the irradiation experiment, resulting in the beam rastering over a larger area, which produced a more diffuse irradiation, with a lower peak damage.

The fiducial marks made on the specimens were designed to produced an irradiated region that began at a crack length of 4.5mm. The results of the microhardness testing suggest that the increase in hardness due to the radiation damage occurs on average at 4.57 ± 0.46mm; hence, for most specimens, except S5, W5 and Z5, a crack length of 5mm is within the irradiated region.

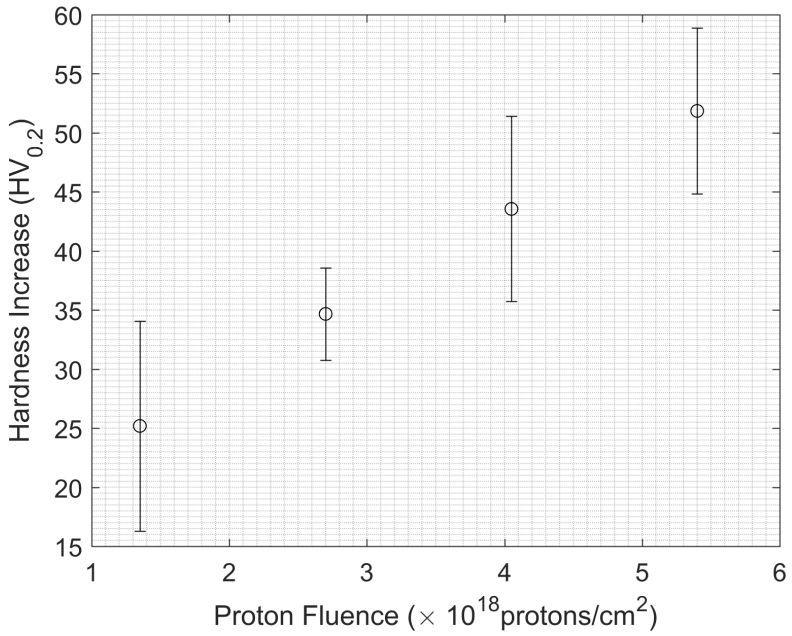

Figure 5.4: Average hardness increase H_I for each fluence level. Error bars are given by the standard deviation. Specimens S & T have been excluded due to closure and W5 has excluded due to an error in the irradiation experiment.

Figure 5.4 shows the average hardness increase observed for each level of radiation

damage. The hardness increase is linear ($R^2 = 0.9991$) with proton fluence, and does not plateau, which suggests the damage is below the saturation level of defects that was observed by Jin et al [76].

Unless otherwise stated, the following analyses will consider only crack lengths from 5mm onwards, which is considered to be within the irradiated region.

Table 5.5: Specimens excluded from further analysis.

Specimen	Exclusion Reason
S	Closure observed into irradiated region.
T	Closure observed into irradiated region.
W5	Incorrect location of irradiated region.

5.1.5 Crack Growth Rate Behaviour

The temperature of the laboratory in which the fatigue crack growth tests were performed could not be controlled. This meant that tests were conducted over a temperature range of $18 - 28$°C. As discussed previously in section 3.2.3, the radiant flux emitted from a surface is proportional to T^4. This means that even relatively small changes in temperature can give large changes in the detected signal for a given stress.

To control for this, a calibration procedure was performed for each experiment. Six data captures of the MT calibration specimen were taken before and six data captures taken after the crack growth test for each specimen. The final calibration factor used was the mean of those calculated from each data capture.

The result of the calibration procedure is a single factor A in MPa/camera unit, which is then passed to FATCAT to perform the stress intensity factor measurements. The uncertainty on the FATCAT outputs is dominated by the uncertainty on the calibration value. This was

estimated by the standard deviation of the twelve measurements taken for each specimen and found to be $\approx 3.5\%$ overall.

To quantify the effect of the proton irradiation on the crack growth rate, the Paris Law equation:

$$\frac{da}{dn} = C\Delta K^m \tag{5.1}$$

was fitted to the data of the specimens at each damage level as a group.

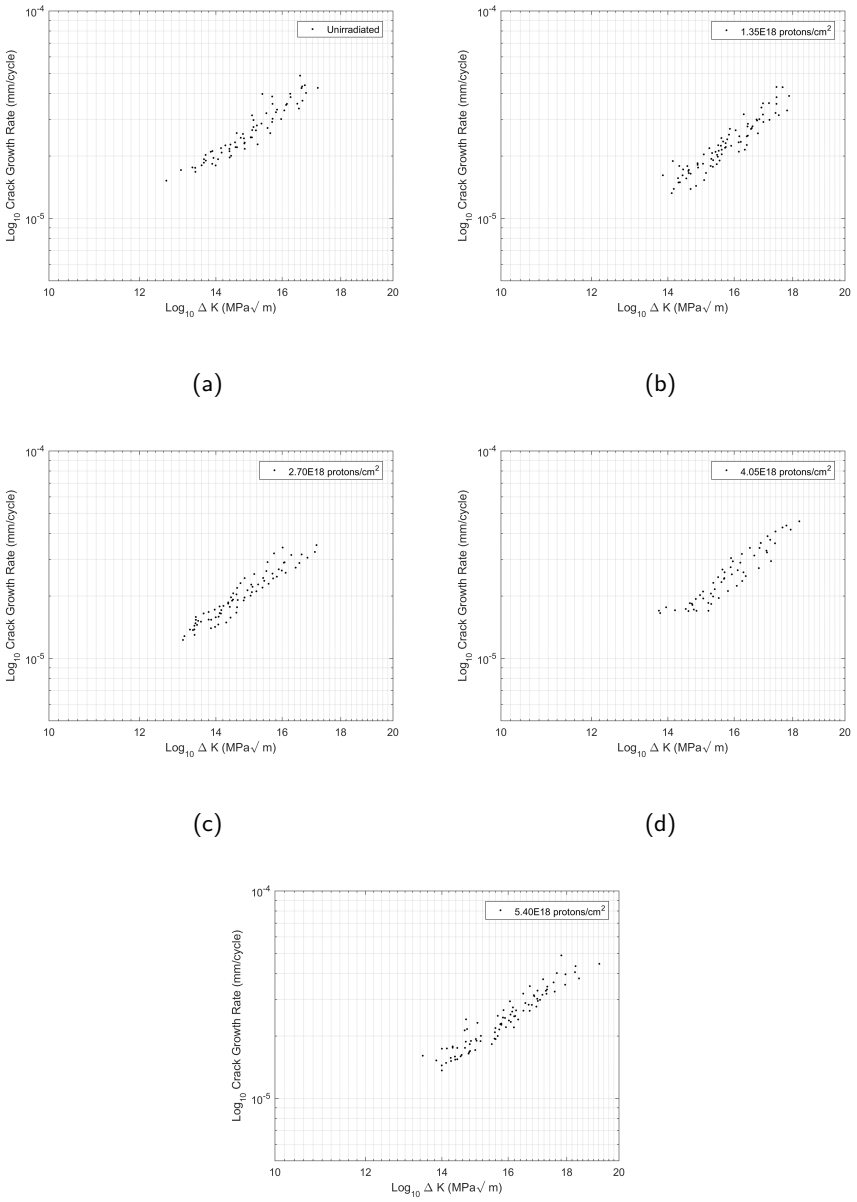

Figure 5.5: Paris Law log-log plots of crack growth rate against stress intensity factor range for all specimens with proton fluences from 0 to 5.40×10^{18}protons/cm^2.

Statistical Analysis

The significance of the results was tested using analysis of covariance (ANCOVA) with F-tests, using a significance value of $p \leq 0.05$. This determined whether the difference between the groups was greater than the difference within a group. ANCOVA requires that

the slopes of the regression lines are parallel. Therefore, the initial step of the analysis tested this assumption.

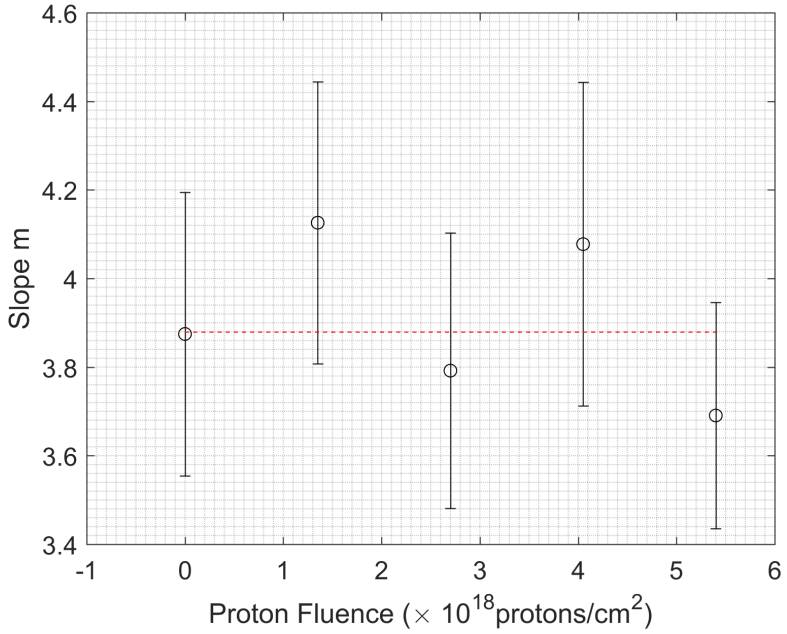

Figure 5.6: Calculated slopes and confidence intervals for the data from each proton fluence group in figure 5.5. The red line shows the mean slope of 3.879 that will be used in the further ANCOVA. p-Values for comparisons between each group are given in table 5.6.

Table 5.6: Results of multiple comparisons between each group for the measured slopes of the Paris Law plots. There are no significant differences between the slopes of any pair of groups.

Group 1	Group 2	Difference	p	$p \leq 0.05$?
Unir	1.35E18	-0.2512	0.8213	No
Unir	2.70E18	0.0828	0.9965	No
Unir	4.05E18	-0.2028	0.9282	No
Unir	5.40E18	0.1841	0.9071	No
1.35E18	2.70E18	0.3339	0.5975	No
1.35E18	4.05E18	0.0484	0.9997	No
1.35E18	5.40E18	0.4352	0.2327	No
2.70E18	4.05E18	-0.2855	0.7780	No
2.70E18	5.40E18	0.1013	0.9884	No
4.05E18	5.40E18	0.3868	0.4378	No

The results shown in figure 5.6 and table 5.6 show that the difference between the measured slopes was not significant, and therefore the ANCOVA could proceed. The mean slope value of 3.879 was used as the gradient of the lines and the significance of the intercepts was analysed.

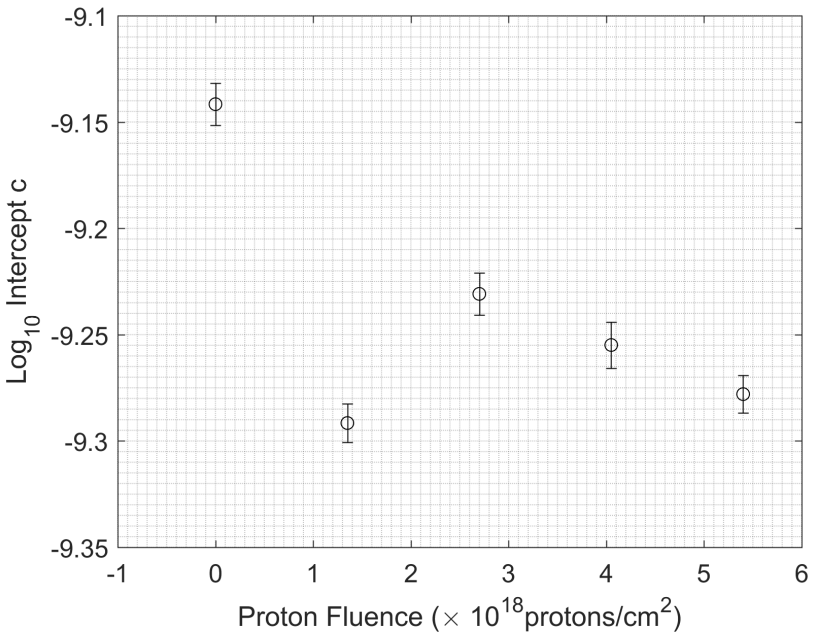

Figure 5.7: Calculated intercepts for regressions with a slope of 3.879 and confidence intervals for each proton fluence group for the data in figure 5.5. p-Values for comparisons between each group are given in table 5.7.

Table 5.7: Results of multiple comparisons between each group for the measured intercepts of the Paris Law plots. The only overlap between groups is for the groups $1.35\text{E}18$ *and* $5.40\text{E}18$.

Group 1	Group 2	Difference	p	$p \leq 0.05$?
Unir	$1.35\text{E}18$	0.1500	0.0000	Yes
Unir	$2.70\text{E}18$	0.0892	0.0000	Yes
Unir	$4.05\text{E}18$	0.1133	0.0000	Yes
Unir	$5.40\text{E}18$	0.1364	0.0000	Yes
$1.35\text{E}18$	$2.70\text{E}18$	-0.0607	0.0000	Yes
$1.35\text{E}18$	$4.05\text{E}18$	-0.0367	0.0000	Yes
$1.35\text{E}18$	$5.40\text{E}18$	-0.0136	0.2148	No
$2.70\text{E}18$	$4.05\text{E}18$	0.0241	0.0148	Yes
$2.70\text{E}18$	$5.40\text{E}18$	0.0471	0.0000	Yes
$4.05\text{E}18$	$5.40\text{E}18$	0.0231	0.0103	Yes

The difference in intercept position was small in magnitude between each group, but is significant. The result for the 1.35×10^{18}protons/cm^2 proton fluence required further investigation as it appeared to be far outside the others.

The same analysis as above has also been performed between the unirradiated group and the two individual heated specimens. Again, there was found to be no significant difference in the gradients of the Paris plot, the mean of which was 3.6372, however there were significant differences in the intercepts. This was not expected, as it was thought that the 360°C temperature was not high enough to result in any changes to the specimen behaviour.

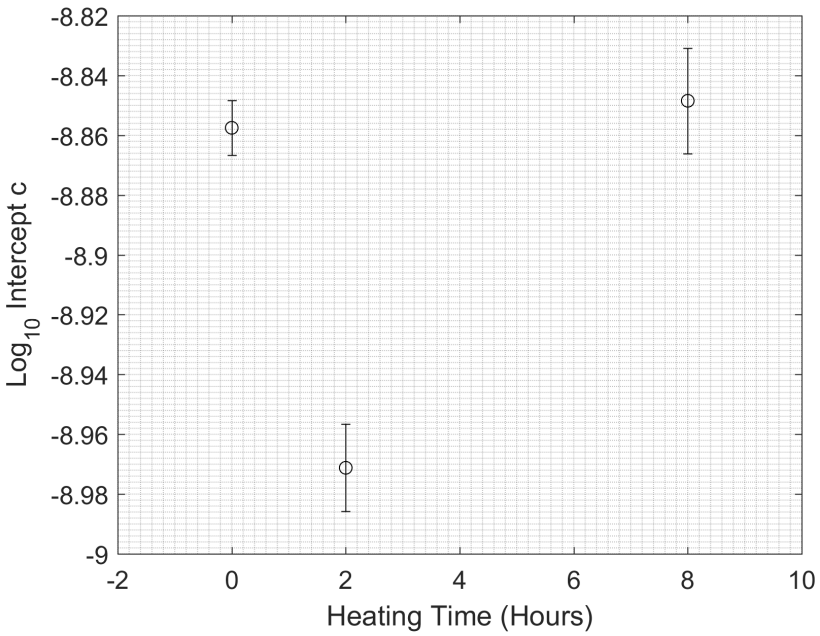

Figure 5.8: Calculated intercepts for regressions with a slope of 3.6372 and confidence intervals for each of the heating conditions. p-Values for comparisons between each group are given in table 5.8.

Table 5.8: Results of multiple comparisons between each group for the measured intercepts of the Paris Law plots. No significant difference in intercept was found between 0 and 8 hours of heating, however 2 hours of heating is significantly different to both 0 and 8 hours.

Group 1	Group 2	Difference	p	$p \leq 0.05$?
0	2	0.1137	0.0000	Yes
0	8	0.0090	0.7016	No
2	8	-1.228	0.0000	Yes

The effect of a heating time of two hours is significantly different to both no heating at all and eight hours of heating. This could help to explain the anomalous results for the 1.35×10^{18}protons/cm^2 fluence specimens, which also saw a reduction in the intercept value, and were irradiated for two hours.

Correlation with Hardness Increase

Excluding the 1.35×10^{18}protons/cm^2 specimens, which appeared to be heat-affected, the behaviour of the remaining specimens correlated linearly with proton fluence as shown in figure 5.9.

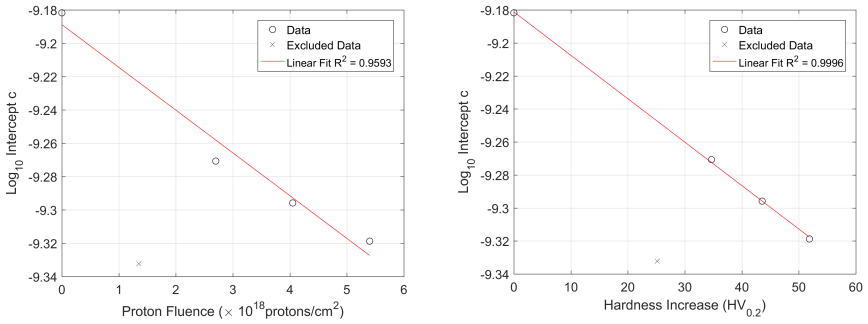

(a) (b)

Figure 5.9: Plots of fluence (a) and hardness increase (b) against log_{10} Paris Law intercept, with associated linear fits. The change in intercept correlated linearly with both hardness increase and proton fluence, but hardness increase had a slightly better R^2 value.

5.1.6 Plastic Zone Size

Concurrent with the stress intensity factor measurements made using the first harmonic thermoelastic data, plastic zone measurements were made using the second harmonic data.

Obtaining an accurate measure of the plastic zone radius proved difficult as the plastic zone appeared tilted in some specimens, despite the use of self-aligning grips. Therefore all results were provided using the areas obtained from the thresholding procedure of the second harmonic X-images outlined in section 4.3.1.

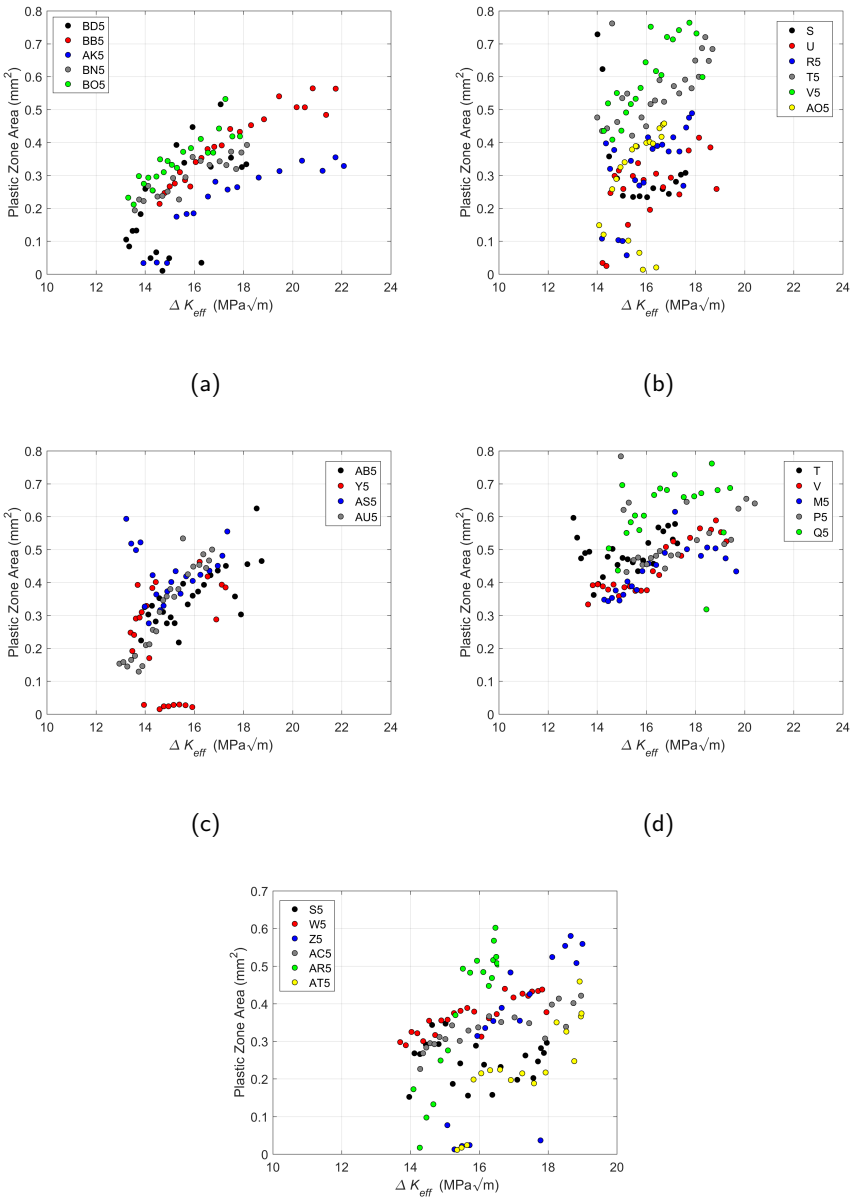

Figure 5.10: Plots of measured plastic zone area using the second harmonic method for unirradiated (a), 1.35×10^{18}protons/cm^2 *(b),* 2.7×10^{18}protons/cm^2 *(c),* 4.05×10^{18}protons/cm^2 *(d), and* 5.40×10^{18}protons/cm^2 *specimens.*

In contrast to the prior assumption that the plastic zone area would be proportional to ΔK^4, this proved a poor fit, whereas a model of ΔK^2 provided a better fit. Therefore the plastic zone data for each specimen was fitted with a function of the form:

$$A_{pz} = a\Delta K^2 \tag{5.2}$$

where: A_{pz} is the measured plastic zone area, a is the fit parameter, and ΔK^2 is the calculated stress intensity factor.

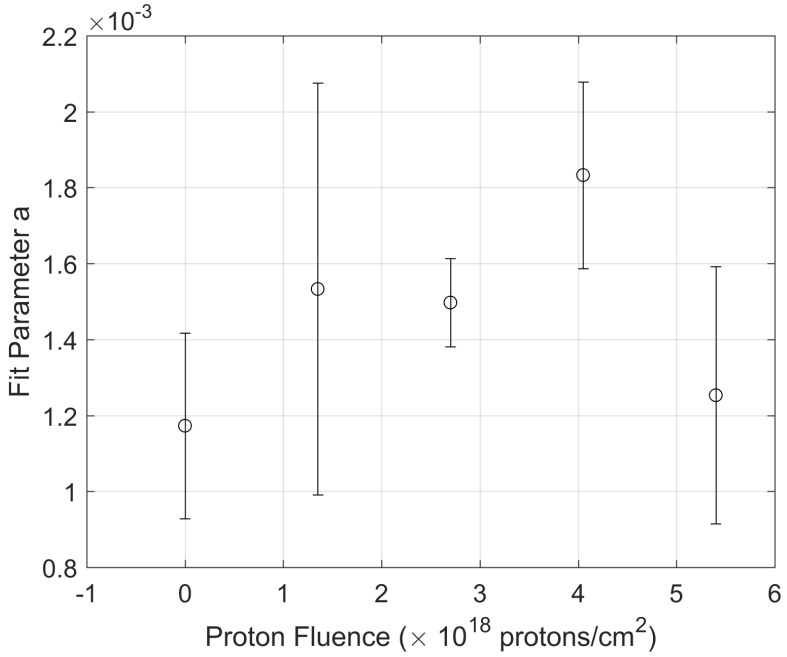

Figure 5.11: Average values of a from the fit of equation (5.2) *to the the plastic zone area measurements for each specimen. Error bars are given by the standard deviations of the a values.*

5.1.7 Dissipated Energy

Following the procedure outlined in section 4.4, the total dissipated energy per cycle from the plastic zone has been calculated for the specimens.

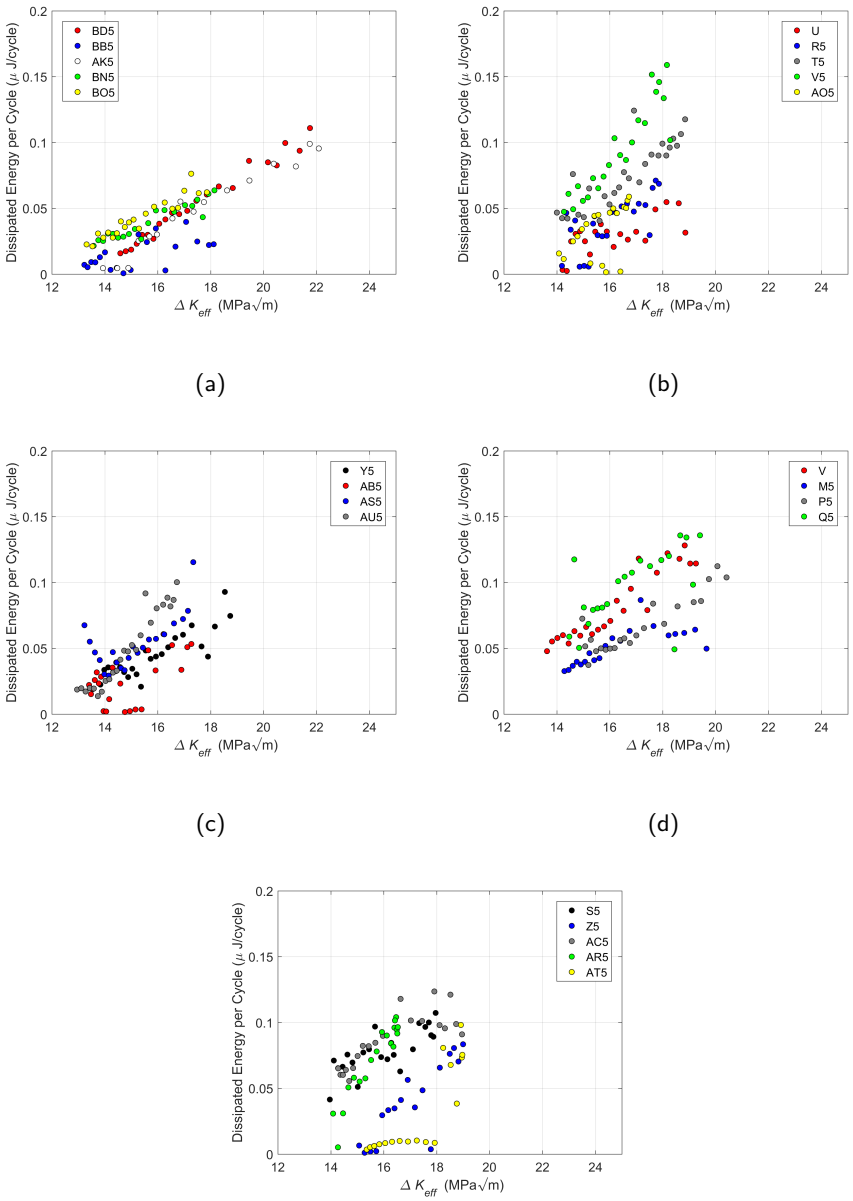

(a) (b)

(c) (d)

(e)

Figure 5.12: Plots of total dissipated energy per cycle from the plastic zone against stress intensity factor for unirradiated (a), 1.35×10^{18}protons/cm^2 *(b),* 2.7×10^{18}protons/cm^2 *(c),* 4.05×10^{18}protons/cm^2 *(d), and* 5.40×10^{18}protons/cm^2 *specimens*

Compared to the plastic zone area results given in figure 5.10, there is qualitatively less scatter in the dissipated energy measurements. Irradiation damage appears to generate a lot of scatter between specimens compared to the unirradiated case.

Using a similar procedure to the plastic zone results, the data for each specimen has been fitted using an equation, based on the literature discussed in section 4.5, of the form:

$$U = a\Delta K^4 \tag{5.3}$$

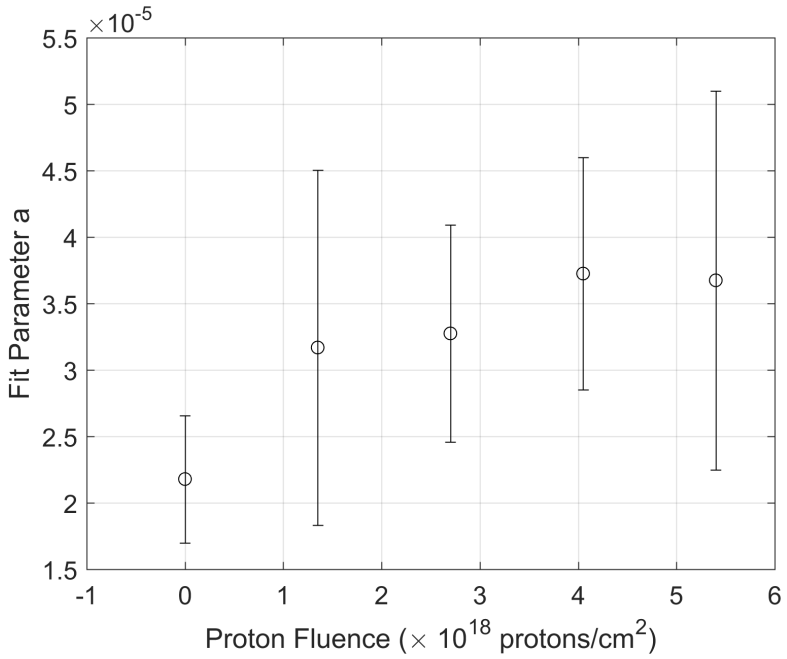

Figure 5.13: Average values of U given by the fit of equation (5.3) *to the dissipated energy measurements for each specimen. Error bars are given by the standard deviation of the U values. A linear model can be fitted with $R^2 = 0.8119$.*

5.2 Stripe Irradiations

5.2.1 Experiment Design

In early results of the main experimental program crack closure was observed in irradiated specimens, resulting in a decreased crack growth rate as the crack tip traversed the boundary between the virgin and irradiated material.

An experiment was devised to investigate crack growth through the reverse damage gradient, i.e. from irradiated to unirradiated. To achieve this a thin strip of material was

irradiated, rather than the large area used for the main experiments.

The planned edge of the irradiated area for the stripe specimens was located in the same place as for the previous specimens (4.5mm from the load line), and extended parallel to the load line the same distance (5mm either side of the mid-plane, but would only extend 1mm in the crack growth direction. This gives an area ten times smaller than for the main specimens. In order to give an approximately similar irradiation effects, the proton fluence was kept the same and current reduced to keep the damage rate similar.

Table 5.9: Monitoring data obtained from the end-station control computer for each stripe irradiated specimen.

Specimen	Accumulated Charge (C)	Irradiation Time (hours)	Ion Fluence ($\times 10^{18}$ions/cm^2)	Beam Current (μA, average)	DPA Bragg Peak (DPA at $13.2\mu m$)	Temperature (°C, average)	Temperature (°C, maximum)
AX5	0.0216	3.72	1.35	2.9	0.94	360.43	368.70
AZ5	0.0216	1.65	1.35	3.1	0.94	361.64	365.35
AY5	0.0432	4.72	2.70	5.4	1.87	364.86	703.66
BA5	0.0648	4.00	4.05	5.8	2.81	354.77	381.06
BE5	0.0864	4.53	5.40	5.8	3.76	356.25	371.98
BF5	0.108	5.14	6.75	5.9	4.70	357.23	371.47

Table 5.10: Fit parameters of the microhardness profile data fit with equation (3.16).

Specimen	Ion Fluence ($\times 10^{18}$ions/cm^2)	LHS H_0 (HV$_{0.2}$)	LHS H_I (HV$_{0.2}$)	LHS s	LHS x_I (mm)	LHS R^2	RHS H_0 (HV$_{0.2}$)	RHS H_I (HV$_{0.2}$)	RHS s (HV$_{0.2}$)	RHS x_I (mm)	RHS R^2	Width (mm)
AX5	1.35	167.0	17.2	3.092	4.0	0.7562						
AZ5	1.35											
AY5	2.70	176.7	13.4	5.92	5.0	0.7844	187.3	−17.0	10.2	6.3	0.8404	1.3
BA5	4.05	175.8	19.1	128.6	3.8	0.8819	195.6	−18.5	10.3	5.8	0.8841	2.0
BE5	5.40	168.1	39.7	8.948	3.9	0.9402	203.7	−26.8	10.2	5.0	0.926	1.1
BF5	6.75	181.8	36.9	6.037	4.6	0.9702	215.6	−28.5	5.8	5.7	0.7815	1.1

Table 5.10 shows the results of the fitting procedure for the hardness profiles. The edges of the irradiated area were located by applying the sigmoid fit to each side of the hardness change. LHS and RHS refer to the increasing and decreasing side of the hardness change, with the increase occurring closer to the load line and the decrease occurring further away. It was not possible to obtain a fit to the right hand side of specimen AX5 or fit any part of the hardness information for AZ5 at all, as no increase was observed. Specimens BA5 and BE5 were irradiated too close to the notch, resulting in the precrack itself being irradiated.

Only two specimens were irradiated close to the original planned conditions, AY5 and BF5.

It is likely that beam misalignment caused these problems. Initial alignment of such a narrow beam was difficult and small variations in beam position relative to the tantalum vanes could have caused a relatively large variation in position of the beam on the specimen compared to the area that was intended to be irradiated. It was noted in specimens BA5 and BE5 that the scintillator slides used for alignment started to scintillate faintly during the experiment, suggesting that beam alignment had shifted closer to the notch. However, this could not be adjusted whilst the experiment was running without switching off the beam and interrupting the irradiation, which would have resulted in an unknown amount of recovery of the damage caused.

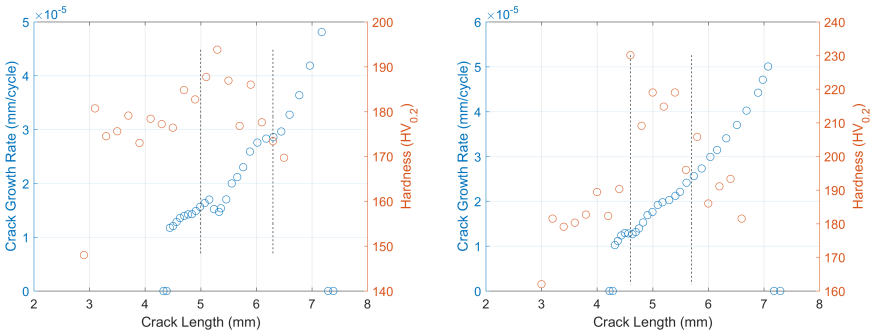

(a) (b)

Figure 5.14: Plots of crack growth rate (left axis) and microhardness (right axis) for the two specimens that were irradiated in the correct location, AY5 (a) and BF5 (b). Dashed black lines indicate the boundaries of the irradiated region give in table 5.10.

It can be seen from figure 5.14 that qualitatively there is a change in the crack growth rate associated with the crack entering the irradiated region. No similar changes in crack growth rate were observed in the other specimens where the irradiation boundary was not located where it was planned.

No signals associated with closure were observed in any of the stripe irradiated specimens.

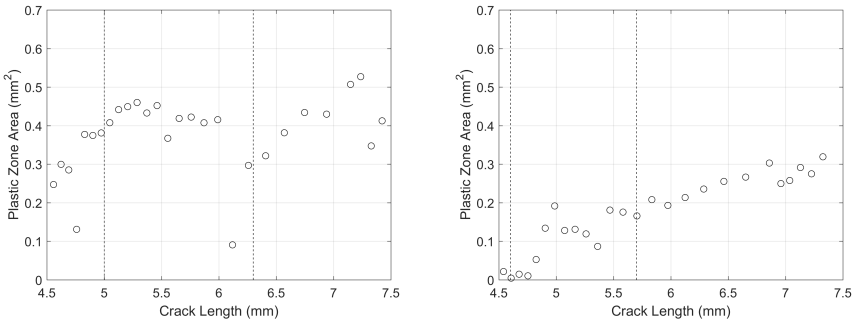

(a) (b)

Figure 5.15: Plots of plastic zone area against crack length for AY5 (a) and BF5 (b). Dashed lines indicate the boundaries of the irradiated region give in table 5.10.

The plastic zone area data presented in figure 5.15 do not show the same trend as

one another. AY5 shows an increase in apparent plastic zone area in the irradiated region, whereas BF5 shows no obvious difference in area inside or outside the area.

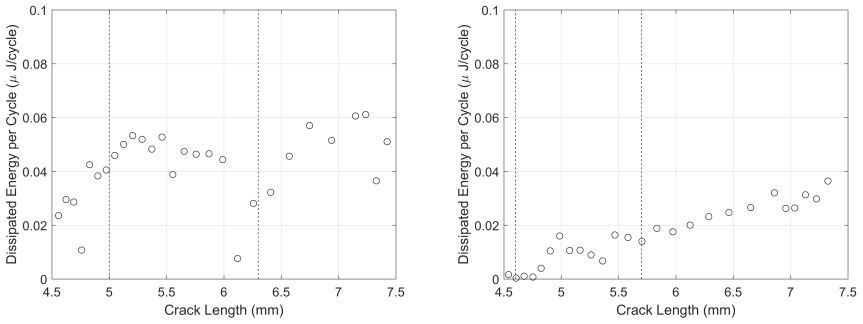

(a) (b)

Figure 5.16: Plots of dissipated energy per cycle against crack length for AY5 (a) and BF5 (b). Dashed lines indicate the boundaries of the irradiated region give in table 5.10.

Dissipated energy follows the same trends as plastic zone area. Again, the specimens are not following the same behaviour as one another.

5.3 Discussion

Despite some challenges with the accelerator and end-station during some irradiation experiments, the majority of the planned irradiation runs were achieved.Some specimens experienced temperature transients caused by the indium in the lower shim of the target stage re-solidifying, which appears to have caused a closure effect. Crack closure was observed in specimens S and T as both a reduction in the effective stress intensity factor and by the generation of crack flank signals in the second harmonic TSA data. It is suspected that the temperature transients combined by the constraint of the clamping process caused the generation of stresses that remained even after several more hours at temperature.

Statistical analysis of the fatigue crack growth rate data presented in figure 5.5 using the ANCOVA technique showed that the radiation damage had no significant effect on the

Paris Law constant, m, the gradient of the graph of crack growth rate with stress intensity factor, figure 5.6. However, a small, but significant, effect was found on the Paris Law constant c, the intercept with the Y-axis, shown in figure 5.7. This suggests that the proton irradiation is shifting the Paris Law relationship lower, such that equivalent ΔK_{eff} values correspond to lower crack growth rates. The difference in effect is small compared to the post-irradiation results of Murase et al [92], with the difference between no irradiation and the maximum 5.4×10^{18}protons/cm^2 being 36% rather than 100%, despite the increased damage achieved in this study. It is possible that the relative thickness of the specimen compared to the damage layer is responsible for this difference as Murase et al [92] managed a full-thickness irradiation of a 0.15mm thick specimen, whereas this study irradiated a surface layer of $\approx 15\mu$m of a 0.8mm thick specimen.

A discrepancy was found in the behaviour of the specimens with the lowest level of damage as they exhibited a much lower crack growth rate than would be expected from the trend of the other specimens. Tests were conducted on the temperature control specimens, which were mounted and heated in the target stage identically to the irradiated specimens, but without switching on the proton beam. The results of which suggested that the short heating times associated with the lowest irradiation damage also cause a significant reduction in crack growth rate compared to specimens heated for longer, or not heated at all. It is likely that this is caused by residual stresses generated during the initial period of heating of the specimen between room temperature and 360°C, which are eventually annealed out after a longer time in the beam. A larger number of heated specimens would give more insight into this effect, but the considerations of using beam-time for irradiation experiments rather than pure heating resulted in less specimens. Future experiments should take this into account, and potentially modify the heating procedure or the target stage mounting to reduce this effect.

The observed reduction in crack growth rate demonstrates that it is not necessary to perform full thickness irradiations to produce a detectable effect of the damage, and suggests that fatigue cracking behaviour in 304 stainless steel can be modified by surface level effects. This could allow testing of thicker specimens, compliant with standards, or allow for direct testing of small regions of actual components. This will give more confidence in the irradiated fatigue cracking performance, and help to inform end-of-life component analysis.

Microhardness testing was successfully used to locate the irradiation boundary in all but one specimen. The increase in hardness was linear with increasing proton fluence ($R = 0.9991$) suggesting that the levels of damage achieved are below the hardness saturation limit discussed by Jin et al [76].

Figure 5.9 suggests that the change in Paris Law c correlates slightly better with the increase in hardness caused by the irradiation than the proton fluence ($R^2 = 0.9996$ v $R^2 = 0.9593$). This would tend to agree with the conclusions drawn by Fenici & Suolang [90] that the effect on crack growth rates is caused mainly by the hardening effect of the irradiation damage.

The plastic zone area measurements shown in figure 5.10 show considerable variability between specimens, even for the unirradiated specimens. As discussed in chapter 4, there is some difficulty in interpreting the second harmonic data, as there are a number of unknowns. Despite this, the plastic zone data is potentially commensurate with the reduction in crack growth rate observed. A larger plastic zone is known to cause a reduction in crack growth rate, as is the case in overloads [67]. Figure 5.11 shows that the plastic zone area appears to increase with proton fluence, except for the highest fluence specimens. There does not seem to be any effect in the 1.35×10^{18}protons/cm^2 specimens that would correspond to the anomalous observed reduction in crack growth rate.

The large plastic zone size, would disagree with the plastic zone models outlined by Irwin

& Dugdale, discussed in section 2.1.2. The increase in hardness caused by the irradiation damage should result in a smaller plastic zone, not larger. The dissipated energy results offer a potential explanation for this effect. Figure 5.13, in contrast to figure 5.11, suggests that the dissipated energy continues to rise with increasing proton fluence, and potentially plateaus rather than reducing for the highest fluence specimens, although the large uncertainties make a definitive interpretation difficult. It could be that the plastic zone area does decrease in size with high levels of irradiation, but the amount of heat being generated by dislocation movement is increased, as indicated by the dissipated energy. The introduction of defects from the radiation damage increases the resistance to dislocation movement in the plastic zone, which could result in more of the plastic work energy being converted to heat. This increased heat generation would manifest as an apparently larger plastic zone as it would lead to increased thermal diffusion.

In order to verify this assumption, a second experimental method would have to be implemented alongside TSA, such as DIC. Care would have to be taken to ensure that the plastic zone area being compared across techniques were arising from the same source, some work in this regard has been performed by Zhang & Liu [58] to measure the cyclic plastic zone using DIC techniques with an optical microscope. This would also help to answer some of the questions with regards to origin of the heat sources in the second harmonic data.

The tests of the stripe irradiated specimens highlighted the difficulty in irradiating small areas using the current target stage set up. For the two specimens that were irradiated correctly, a qualitative change in crack growth rate was observed that spatially correlated with the change in measured hardness, shown in figure 5.14. As with the large area irradiations, there was difficulty correlating the crack growth rate with a change in the plastic zone size. Specimen AY5, irradiated to a fluence of 2.7×10^{18}protons/cm^2 shows an increase in apparent plastic zone size, whereas BF5, irradiated to a fluence of 6.75×10^{18}protons/cm^2

shows no apparent difference in plastic zone area when the crack is within the hardened region. This concurs with the data presented for the larger irradiated area specimens shown in figure 5.11. The same trends are seen in the dissipated energy measurements.

The initial hypothesis that the irradiation boundary induced closure effects was further disproved by the stripe specimens. The effects of closure observed in specimens S and T were not replicated in any of the stripe irradiated specimens. This suggests that the closure effects are more likely to have been caused by the temperature transients or mounting and are unrelated to the irradiation boundary.

The presence of temperature-related closure effects may not have been an issue in the latter experiments as these appeared to have been the result of temperature transients caused by indium shim solidification, which was rectified for the later experiments. However, the apparent temperature-related reduction in crack growth rate for short times subjected to heating indicate a potential problem with the target stage mounting or methodology. It may be that the heating must be performed at a much slower rate to reduce the potential for generating residual stress, which has implications for the amount of experimental time available for irradiations.

The results suggest that fatigue behaviour is influenced by radiation damage, even with a surface level of damage. For the range of damage levels investigated, it appears that radiation damage has a somewhat protective effect, reducing the fatigue crack growth rate. This potentially means crack size limits for irradiated material could be overly conservative, and components lifetime could be extended safely. Of course, careful consideration of the other properties affected by the irradiation must also be considered. The increased hardness and decreased ductility will have change the static load bearing behaviour of the components.

Providing the results of the small-scale specimens irradiated with protons show similar fatigue crack growth behaviour to neutrons, research time and cost could be reduced. Ion

irradiation damage can be accelerated, resulting in high damage in a short period of time and can be performed at a lower cost. With care, this approach could allow the expected fatigue crack performance of new materials at end-of-life neutron irradiation levels to be quickly assessed.

Chapter 6

Conclusions

Safe extension of nuclear plant lifetime can be achieved by increasing the available knowledge on the effects of radiation damage on fatigue crack behaviour. Proton damage can be used as a way to achieve end-of-life damage states similar to neutrons, in a faster time and can therefore be used to probe the likely effects to reactor components. This chapter summarises the conclusions drawn from the development of the new TSA technique and results presented in the previous chapter.

A journal paper was published describing the early results of the effect of proton irradiation on crack growth rate [121]. A further paper is in preparation on the plastic zone and closure observations discussed in chapter 4.

6.1 Conclusions

1. Fatigue crack growth rate is reduced by proton irradiation Proton irradiation resulted in a statistically significant decrease in the crack growth rate of 304 stainless steel specimens, with increasing proton damage. This occurred despite the relatively shallow penetration depth of the radiation damage, $15\mu m$, compared to the specimen thickness, $800\mu m$. This is, of course, an unrealistic scenario compared to the full thickness irradiations

experienced by real components. However, it demonstrates there is potential for obtaining data for radiation damage effects without costly and time consuming irradiations.

2. Target stage heating It appears that the heating regime of the target stage has the potential to alter the crack growth rate. Specimens heated or irradiated for 2 hours have a significantly lower crack growth rate than would be expected from the trend seen across the other irradiation damage levels. After 4 hours this effect was not apparent.

3. Plastic zone area and closure detection A novel method has been presented using the second harmonic of the thermal signal to measure plastic zone area. The feature identified as the plastic zone was demonstrated to behave closer to the theoretically expected behaviour, though it did display a large variability between specimens. Despite this, it provided a more robust measure than previous phase-based methods. In addition to plastic zone heating effects, the technique is sensitive to closure. Signals arise on the crack flanks when closure is occurring, providing a simple binary test for crack flank closure. Closure signals are larger in magnitude than the plastic zone signal and overwhelm the smaller signal, limiting the applicability of the technique where closure is occurring.

4. Dissipated Energy By measuring the second harmonic temperature variations in the plastic zone identified using the second harmonic method it has been possible to calculate the energy dissipated per cycle in the plastic zone. This has been performed without assuming the shape of the plastic zone, or knowledge of the yield strength. The results show the same ΔK^4 dependence described in the literature.

5. Irradiation Modifies Plastic Zone Behaviour Given the caveats mentioned above, there was no consistent effect of irradiation found on the plastic zone area. A trend of an increase in plastic zone area with increasing radiation damage was observed until the

highest fluence, which exhibited a smaller area on average. However, the dissipated energy analysis suggests that the amount of energy dissipated in the plastic zone is increasing with increasing fluence. It is proposed that a reduction in area of the plastic zone is competing with the increase in dissipated energy, which manifests as an apparently larger plastic zone due to increased conduction influencing the thermal data.

6.1.1 Future Work

There are a number of questions that have arisen during the course of this project that could not be completely addressed and that could form the basis of a future research project:

Plastic Zone Measurements Obtaining a more thorough understanding of the effects at the second harmonic frequency will help with future investigations of plasticity in materials that do not exhibit a strong effect in the phase image of standard TSA.

End-Station Development A conclusion of this work is that there is an effect of short-term heating in the end-station. This was discovered after the experimental program was completed. Future research using this equipment should perform a more thorough investigation of the effect and recommend updates to the operation or construction of the target stage and end-station to mitigate these effects.

Retained Hydrogen One of the fundamental differences between neutron and proton irradiation is the potential for hydrogen retention. Following the damage cascade, the incident protons will come to rest as an interstitial in the metal. At the irradiation temperature used, 360°C, the hydrogen atoms will readily diffuse through the austenite. However, the damage introduced by the proton beam will trap some hydrogen. Hence, it would be interesting to determine how much hydrogen is retained and if it could have a potential effect on results.

A further effect of hydrogen that occurs in real components is hydrogen or helium embrittlement due to transmutation reactions or absorption. The test material could be taken closer to the likely in-service condition by the addition of hydrogen or helium after radiation damage.

References

1. NEA. *Technical and Economic Aspects of Load Following with Nuclear Power Plants* tech. rep. June (2011).

2. Little, E. A. Development of radiation resistant materials for advanced nuclear power plant. *Materials Science and Technology* **22,** 491–518. ISSN: 0267-0836. `http://www.tandfonline.com/doi/full/10.1179/174328406X90998` (May 2006).

3. ASME. *ASME Boiler and Pressure Vessel Code Section XI* tech. rep. (2010).

4. Inglis, C. E. Stresses in a plate due to the presnce of cracks and sharp corners. *Trans. Inst. Naval Arch.* **55,** 219–239. ISSN: 1050-0529 (1913).

5. Griffith, A. A. The Phenomena of Rupture and Flow in Solids. *Philosophical Transactions* **221,** 163–198 (1920).

6. Irwin, G. R. *Onset of fast crack propagation in high strength steel and aluminium alloys* in *Sagamore Research Conference Proceedings* (1956), 1–23.

7. Westergaard, H. M. Bearing pressures and cracks. *Journal of Applied Mechanics* **61,** A49–A53 (1939).

8. Irwin, G. R. Analysis of Stresses and Strains near the End of a Crack Traversing a Plate. *Journal of Applied Mechanics* **24,** 361–364 (1957).

9. Rice, J. R. Mechanics of Derformation and Extension by Fatigue. *Fatigue Crack Propagation, STP 415,* 247–309 (1967).

10. Irwin, G. R. *Plastic Zone Near a Crack and Fracture Toughness* in *Proceedings of the Seventh Sagamore Ordnance Materials Research Conference* (1960), IV 63 –78.

11. Dugdale, D. Yielding of steel sheets containing slits. *Journal of the Mechanics and Physics of Solids* **8,** 100–104. ISSN: 00225096. http://linkinghub.elsevier.com/retrieve/pii/0022509660900132 (May 1960).

12. Barenblatt, G. The Mathematical Theory of Equilibrium Cracks in Brittle Fracture. *Advances in Applied Mechanics* **7,** 55–129. ISSN: 0065-2156. https://www.sciencedirect.com/science/article/pii/S0065215608701212 (Jan. 1962).

13. Paris, P. C., Gomez, M. P. & Anderson, W. E. A rational analytic theory of fatiuge. *The Trend in Engineering* **13,** 9–14. ISSN: 0742-4795. http://gasturbinespower.asmedigitalcollection.asme.org/article.aspx?doi=10.1115/1.4028568 (1961).

14. Paris, P. & Erdogan, F. A Critical Analysis of Crack Propagation Laws. *Journal of Basic Engineering* **85,** 528. ISSN: 00219223. http://fluidsengineering.asmedigitalcollection.asme.org/article.aspx?articleid=1431537 (1963).

15. Broek, D. & Schijve, J. *The Influence of the Mean Stress on the Propagation of Fatigue Cracks in Light Alloy Sheet* tech. rep. (National Aero-Research Institute, Amsterdam, 1963).

16. Forman, R. G., Kearney, V. E. & Engle, R. M. Numerical Analysis of Crack Propagation in Cyclic-Loaded Structures. *Journal of Basic Engineering* **89,** 459–463. ISSN: 00219223 (1967).

17. Elber, W. The Significance of Fatigue Crack Closure. *American Society for Testing and Materials* **486,** 230–242. ISSN: 10403094. http://www.astm.org/doiLink.cgi?STP26680S (1971).

18. Elber, W. Equivalent constant-amplitude concept for crack growth under spectrum loading. *Fatigue crack growth under spectrum loads - ASTM STP 595,* 236–250. http://books.google.ch/books?hl=en%7B%5C&%7Dlr=%7B%5C&%7Did=aq4by6wmg7YC%7B%5C&%7Doi=fnd%7B%5C&%7Dpg=PA236%7B%5C&%7Ddq=Equivalent+Constant-Amplitude+Concept+for+Crack+Growth+Under+Spectrum+Loading%7B%5C&%7Dots=hz7PDp38c%7B%5C_%7D%7B%5C&%7Dsig=l6HCZ9%7B%5C_%7DVYdu9Zk7F39vcrv5%7B%5C_%7DDJU (1976).

19. James, M. *Some unresolved issues with fatigue crack closure: measurement, mechanism and interpretation problems* in *Proc. of the 9th Int. Conf. on Fracture, Sydney, 1–5 April 1997, vol. 5* (eds Karihaloo, B. L., Mai, Y.-M., Ripley, N. I. & Ritchie, R. O.) (Sydney, 1997), 2403–2414.

20. ASTM. E-647 Standard Test Method for Measurement of Fatigue Crack Growth Rates, 1–43 (1999).

21. Brinell, J. II.Cong. Int. Methodes d'Essai. *Journal of the Iron and Steel Institute* **59,** 243 (1901).

22. Smith, R. L. & Sandly, G. E. An Accurate Method of Determining the Hardness of Metals, with Particular Reference to Those of a High Degree of Hardness. *Proceedings of the Institution of Mechanical Engineers* **102,** 623–641. ISSN: 0020-3483. http://journals.sagepub.com/doi/10.1243/PIME%7B%5C_%7DPROC%7B%5C_%7D1922%7B%5C_%7D102%7B%5C_%7D033%7B%5C_%7D02 (June 1922).

23. Dolins, S. Work-hardening in the drilling of austenitic stainless steels. *Journal of Materials Processing Technology* **133,** 63–70 (2003).

24. Bathias, C. & Pelloux, R. M. Fatigue crack propagation in martensitic and austenitic steels. *Metallurgical Transactions* **4,** 1265–1273. ISSN: 0360-2133. http://link.springer.com/10.1007/BF02644521 (May 1973).

25. Purcell, A. H. & Weertman, J. Crack tip area in fatigued copper single crystals. *Metallurgical Transactions* **5,** 1805–1809. ISSN: 0360-2133. http://link.springer.com/10.1007/BF02644144 (Aug. 1974).

26. Levy, N., Marcal, P. V., Ostergren, W. J. & Rice, J. R. Small scale yielding near a crack in plane strain: A finite element analysis. *International Journal of Fracture Mechanics* **7,** 143–156. ISSN: 00207268 (1971).

27. Loye, C., Bathias, C., Retali, D. & Devaux, J. in *Fatigue Mechanisms: Advances in Quantitative Measurement of Physical Damage* 427–427–18 (ASTM International, 100 Barr Harbor Drive, PO Box C700, West Conshohocken, PA 19428-2959, 1983). http://www.astm.org/doiLink.cgi?STP30568S.

28. Guerra-Rosa, L., Moura Branco, C. & Radon, J. C. Monotonic and cyclic crack tip plasticity. *International Journal of Fatigue* **6,** 17–24. ISSN: 01421123 (1984).

29. Doerner, M. & Nix, W. A method for interpreting the data from depth-sensing indentation instruments. *Journal of Materials Research* **1,** 601–609. ISSN: 0884-2914. https://www.cambridge.org/core/product/identifier/S0884291400000662/type/journal%7B%5C_%7Darticle (Aug. 1986).

30. Nyström, M., Soderlund, E. & Karlsson, B. Plastic zones around fatigue cracks studied by ultra-low-load indentation technique. *International Journal of Fatigue* **17,** 141–147. ISSN: 0142-1123. https://www.sciencedirect.com/science/article/pii/014211239595894M?via%7B%5C%%7D3Dihub (Feb. 1995).

31. Yang, F., Saxena, A. & Riester, L. Use of the Nanoindentation Technique for Studying Microstructure/Crack Interactions in the Fatigue of 4340 Steel. *Metallurgical and Materials Transactions A: Physical Metallurgy and Materials Science* **29,** 3029–3036. ISSN: 10735623 (1998).

32. Tao, H. *et al.* Hydrogen Effect on the Fatigue Crack Growth in Austenitic Stainless Steel Investigated by a New Method Based on Nanohardness Distribution. *Journal of Materials Engineering and Performance* **27,** 6485–6492. ISSN: 15441024. https://link.springer.com/article/10.1007/s11665-018-3764-1?utm%7B%5C_%7Dsource=researcher%7B%5C_%7Dapp%7B%5C&%7Dutm%7B%5C_%7Dmedium=referral%7B%5C&%7Dutm%7B%5C_%7Dcampaign=MKEF%7B%5C_%7DUSG%7B%5C_%7DResearcher%7B%5C_%7Dinbound (2018).

33. Kikukawa, M., Jono, M., Tanaka, K. & Takatani, M. Measurement of Fatigue Crack Propagation and Crack Closure at Low Stress Intensity Level by Unloading Elastic Compliance Method. *Journal of the Society of Materials Science, Japan* **25,** 899–903. ISSN: 1880-7488. http://joi.jlc.jst.go.jp/JST.Journalarchive/jsms1963/25.899?from=CrossRef (1976).

34. De Matos, P. F. P. & Nowell, D. Experimental and numerical investigation of thickness effects in plasticity-induced fatigue crack closure. *International Journal of Fatigue* **31,** 1795–1804. ISSN: 01421123. http://dx.doi.org/10.1016/j.ijfatigue.2008.12.003 (2009).

35. Pacey, M. N., James, M. N. & Patterson, E. A. A new photoelastic model for studying fatigue crack closure. *Experimental Mechanics* **45,** 42–52. ISSN: 00144851 (2005).

36. Diaz, F. A., Patterson, E. A. & Yates, J. R. *Fatigue damage assessment using thermoelastic stress analysis* in *ECF15* (2004).

37. Chai, M., Zhang, Z., Duan, Q. & Song, Y. Assessment of fatigue crack growth in 316LN stainless steel based on acoustic emission entropy. *International Journal of Fatigue* **109,** 145–156. ISSN: 01421123. https://doi.org/10.1016/j.ijfatigue.2017.12.017 (2018).

38. Bhuiyan, M. Y. & Giurgiutiu, V. The signatures of acoustic emission waveforms from fatigue crack advancing in thin metallic plates. *Smart Materials and Structures* **27.** ISSN: 1361665X (2018).

39. Irwin, G. R. *Discussion of the paper: The dynamic stress distribution surrounding a running crack— Photoelastic analysis* in *Proc. Soc. Exp. Stress Anal.* (1958), 93–96.

40. Sanford, R. J. & Dally, J. W. A general method for determining mixed-mode stress intensity factors from isochromatic fringe patterns. *Engineering Fracture Mechanics* **11,** 621–633. ISSN: 00137944 (1979).

41. James, M. N., Pacey, M. N., Wei, L. W. & Patterson, E. A. Characterisation of plasticity-induced closure - crack flank contact force versus plastic enclave. *Engineering Fracture Mechanics* **70,** 2473–2487. ISSN: 00137944 (2003).

42. Christopher, C. J., James, M. N., Patterson, E. A. & Tee, K. F. A quantitative evaluation of fatigue crack shielding forces using photoelasticity. *Engineering Fracture Mechanics* **75,** 4190–4199. ISSN: 00137944 (2008).

43. Post, D. Developments In Moire Interferometry. *Optical Engineering* **21.** ISSN: 0091-3286 (1982).

44. McDonach, A., McKelvie, J., MacKenzie, P. & Walker, C. A. Improved Moiré Interferometry and Applications in Fracture Mechanics, Residual Stress and Damaged Composites. *Experimental Techniques* **7,** 20–24. ISSN: 17471567 (1983).

45. Nicoletto, G. Fatigue Crack Tip Strains in 7075-T6 Aluminum Alloy. *Fatigue & Fracture of Engineering Materials & Structures* **10,** 37–49. ISSN: 14602695 (1987).

46. Smith, C. W., Post, D. & Nicoletto, G. Experimental stress-intensity distributions in three-dimensional cracked-body problems. *Experimental Mechanics* **23,** 378–382. ISSN: 0014-4851. http://link.springer.com/10.1007/BF02330051 (Dec. 1983).

47. Gray, T. G. & MacKenzie, P. M. Fatigue crack closure investigation using Moiré interferometry. *International Journal of Fatigue* **12,** 417–423. ISSN: 01421123 (1990).

48. Patterson, E. A. & Olden, E. J. Optical analysis of crack tip stress fields: a comparative study. *Fatigue & Fracture of Engineering Materials & Structures* **27,** 623–635. http://onlinelibrary.wiley.com/doi/10.1111/j.1460-2695.2004.00774.x/full (2004).

49. Rosakis, A. J. & Freund, L. B. The Effect of Crack-Tip Plasticity on the Determination of Dynamic Stress-Intensity Factors by the Optical Method of Caustics. *Journal of Applied Mechanics* **48,** 302. ISSN: 00218936. http://appliedmechanics.asmedigitalcollection.asme.org/article.aspx?articleid=1405772 (1981).

50. Rosakis, A. J., Zehnder, A. T. & Narasimhan, R. Caustics By Reflection And Their Application To Elastic-Plastic And Dynamic Fracture Mechanics. *Optical Engineering* **27.** ISSN: 0091-3286. http://opticalengineering.spiedigitallibrary.org/article.aspx?doi=10.1117/12.7976730 (Aug. 1988).

51. Bull, C. & Hermann, R. Fatigue crack growth and closure in aluminum alloys. *Scripta Metallurgica et Materialia* **30,** 1337–1342. ISSN: 0956716X. https://linkinghub.elsevier.com/retrieve/pii/0956716X94902690 (May 1994).

52. Tomlinson, R. A. & Patterson, E. A. A study of residual caustics generated from fatigue cracks. *Fatigue and Fracture of Engineering Materials and Structures* **20,** 1467–1479. ISSN: 8756758X (1997).

53. Hirsch, P. B. & Kellar, J. N. A study of cold-worked aluminium by an X-ray microbeam technique. I. Measurement of particle volume and misorientations. *Acta Crystallographica* **5,** 162–167. ISSN: 0365-110X. http://scripts.iucr.org/cgi-bin/paper?S0365110X52000496 (Mar. 1952).

54. Shuji, T. & Keisuke, T. Study of fatigue crack propagation by X-ray diffraction approach. *Engineering Fracture Mechanics* **4,** 925–938. ISSN: 00137944 (1972).

55. Withers, P. J. Fracture mechanics by three-dimensional crack-tip synchrotron X-ray microscopy. *Philosophical Transactions of the Royal Society A: Mathematical, Physical and Engineering Sciences* **373,** 20130157. ISSN: 1364-503X. https://royalsocietypublishing.org/doi/10.1098/rsta.2013.0157 (Mar. 2015).

56. Löffl, C., Saage, H. & Göken, M. In situ X-ray tomography investigation of the crack formation in an intermetallic beta-stabilized TiAl-alloy during a stepwise tensile loading. *International Journal of Fatigue* **124,** 138–148. ISSN: 01421123. https://doi.org/10.1016/j.ijfatigue.2019.02.035 (2019).

57. Lopez-Crespo, P., Shterenlikht, A., Yates, J. R., Patterson, E. A. & Withers, P. Some experimental observations on crack closure and crack-tip plasticity. *Fatigue & Fracture of Engineering Materials & Structures* **32,** 418–429. ISSN: 8756758X (2009).

58. ZHANG, W. & LIU, Y. Plastic zone size estimation under cyclic loadings using in situ optical microscopy fatigue testing. *Fatigue & Fracture of Engineering Materials & Structures* **34,** 717–727. ISSN: 8756758X. http://doi.wiley.com/10.1111/j.1460-2695.2011.01567.x (Sept. 2011).

59. Vasco-Olmo, J. M., Díaz, F. A., James, M. N., Christopher, C. J. & Patterson, E. A. Experimental methodology for the quantification of crack tip plastic zone and shape from the analysis of displacement fields. *Frattura ed Integrita Strutturale* **11,** 166–174. ISSN: 19718993 (2017).

60. Thomson, W. On Dynamical Theory of Heat. *Transactions of the Royal Society of Edinburgh* **20,** 261–283 (1853).

61. Harwood, N. & Cummings, W. M. *Thermoelastic Stress Analysis* (Adam Hilger, New York, 1991).

62. Dulieu-Barton, J. M. & Stanley, P. Development and applications of thermoelastic stress analysis. *The Journal of Strain Analysis for Engineering Design* **33,** 93–104. ISSN: 0309-3247 (1998).

63. Stanley, P. & Dulieu-Smith, J. M. The Determination of Crack-tip Parameters from Thermoelastic Data. *Experimental Techniques* **20,** 21–23 (1996).

64. Diaz, F. A., Yates, J. R. & Patterson, E. A. Some improvements in the analysis of fatigue cracks using thermoelasticity. *International Journal of Fatigue* **26,** 365–376. ISSN: 01421123 (2004).

65. Nurse, A. D. & Patterson, E. A. Determination of predominantly mode II stress intensity factors from isochromatic data. *Fatigue and Fracture of Engineering Materials and Structures* **16,** 1339–1354. ISSN: 8756758X (1993).

66. Diaz, F. A., Patterson, E. A. & Yates, J. R. Assessment of effective stress intensity factors using thermoelastic stress analysis. *The Journal of Strain Analysis for Engineering Design* **44,** 621–632. ISSN: 0309-3247. `http://journals.pepublishing.com/openurl.asp?genre=article%7B%5C&%7Did=doi:10.1243/03093247JSA515` (2009).

67. Patki, A. S. & Patterson, E. A. Thermoelastic stress analysis of fatigue cracks subject to overloads. *Fatigue and Fracture of Engineering Materials and Structures* **33,** 809–821. ISSN: 8756758X (2010).

68. Palumbo, D., De Finis, R., Ancona, F. & Galietti, U. Damage monitoring in fracture mechanics by evaluation of the heat dissipated in the cyclic plastic zone ahead of the crack tip with thermal measurements. *Engineering Fracture Mechanics* **181,** 65–76. ISSN: 00137944. http://dx.doi.org/10.1016/j.engfracmech.2017.06.017 (2017).

69. Sakagami, T., Kubo, S., Tamura, E., Nishimura, T. & Steel, K. *Identification of Plastic-Zone Based on Double Frequency Lock-in Thermographic* in *11th International Conference on Fracture* (2005), 3751–3757. ISBN: 9781617820632.

70. Whittle, K. *Nuclear Materials Science* ISBN: 9780750311045 (IOP Publishing, Bristol, 2016).

71. Cranberg, L., Frye, G., Nereson, N. & Rosen, L. Fission Neutron Spectrum of ¡math display="inline"¿ ¡mrow¿ ¡msup¿ ¡mrow¿ ¡mi mathvariant="normal"¿U¡/mi¿ ¡/mrow¿ ¡mrow¿ ¡mn¿235¡/mn¿ ¡/mrow¿ ¡/msup¿ ¡/mrow¿ ¡/math¿. *Physical Review* **103,** 662–670. ISSN: 0031-899X. https://link.aps.org/doi/10.1103/PhysRev.103.662 (Aug. 1956).

72. Odette, G. R. & Lucas, G. E. Embrittlement of nuclear reactor pressure vessels. *Jom* **53,** 18–22. ISSN: 10474838 (2001).

73. Wady, P. *et al.* Accelerated radiation damage test facility using a 5MV tandem ion accelerator. *Nuclear Instruments and Methods in Physics Research Section A: Accelerators, Spectrometers, Detectors and Associated Equipment* **806,** 109–116.

ISSN: 01689002. http://www.sciencedirect.com/science/article/pii/S0168900215011596 (2016).

74. Was, G. S. *Fundamentals of Radiation Materials Science* (Springer, 2007).

75. Zinkle, S., Maziasz, P. & Stoller, R. Dose dependence of the microstructural evolution in neutron-irradiated austenitic stainless steel. *Journal of Nuclear Materials* **206,** 266–286. ISSN: 00223115. https://linkinghub.elsevier.com/retrieve/pii/002231159390128L (Nov. 1993).

76. Jin, H.-H., Hwang, S. S., Choi, M. J., Lee, G. & Kwon, J. Proton irradiation for radiation-induced changes in microstructures and mechanical properties of austenitic stainless steel. *Journal of Nuclear Materials* **513,** 271–281. ISSN: 00223115. https://doi.org/10.1016/j.jnucmat.2018.11.017 (2019).

77. Okamoto, P. R. & Wiedersich, H. Segregation of alloying elements to free surfaces during irradiation. *Journal of Nuclear Materials* **53,** 336–345. ISSN: 00223115 (1974).

78. Marwick, A. D. Segregation in irradiated alloys: The inverse Kirkendall effect and the effect of constitution on void swelling. *Journal of Physics F: Metal Physics* **8,** 1849–1861. ISSN: 03054608 (1978).

79. Kirkendall, E., Thomassen, L. & Upthegrove, C. Rates of Diffusion of Copper and Zinc in Alpha Brass. *Trans. AIME* **133,** 186–203 (1939).

80. Shoji, T., Lu, Z. & Peng, Q. Factors affecting stress corrosion cracking (SCC) and fundamental mechanistic understanding of stainless steels. *Stress corrosion cracking: Theory and practice,* 245–272 (2011).

81. Scott, P. A review of irradiation assisted stress corrosion cracking. *Journal of Nuclear Materials* **211,** 101–122. ISSN: 10054537 (1994).

82. Garner, F. in *Comprehensive Nuclear Materials* 33–95 (Elsevier, Amsterdam, 2012). ISBN: 9780080560335. http://www.sciencedirect.com/science/article/pii/B9780080560335000653%20https://linkinghub.elsevier.com/retrieve/pii/B9780080560335000653.

83. Chung, H. M., Sanecki, J. E. & Garner, F. A. *Radiation-Induced Instability of MnS Precipitates and its Possible Consequences on Irradiation-Induced Stress Corrosion Cracking of Austenitic Stainless Steels* in *Effects of Radiation on Materials: 18th International Symposium. ASTM STP 1325* (1999), 647–658.

84. Mansur, L. K. & Coghlan, W. A. Mechanisms of helium interaction with radiation effects in metals and alloys: A review. *Journal of Nuclear Materials* **119,** 1–25. ISSN: 00223115 (1983).

85. Malaplate, J. *et al.* Characterization of ion irradiated microstructure and cavity swelling evolution up to high doses in austenitic stainless steels representative of PWR internals. *Journal of Nuclear Materials* **517,** 201–213. ISSN: 00223115 (2019).

86. Was, G. *et al.* Emulation of neutron irradiation effects with protons: validation of principle. *Journal of Nuclear Materials* **300,** 198–216. ISSN: 00223115. https://linkinghub.elsevier.com/retrieve/pii/S0022311501007516 (Feb. 2002).

87. Mansur, L. Correlation of neutron and heavy-ion damage. *Journal of Nuclear Materials* **78,** 156–160. ISSN: 00223115. https://linkinghub.elsevier.com/retrieve/pii/0022311578905147 (Nov. 1978).

88. James, L. Fatigue Crack Propagation in Austenitic Stainless Steels. *Atomic Energy Review* **14,** 37–86 (1976).

89. Weertman, J. & Green, W. Fatigue crack growth under continuous radiation. *Journal of Nuclear Materials* **97,** 254–258. ISSN: 00223115. https://linkinghub.elsevier.com/retrieve/pii/0022311581904724 (Apr. 1981).

90. Fenici, P. & Suolang, S. Fatigue crack growth in 316 type stainless steel at temperatures and displacement damage rates representative for the first wall loading. *Journal of Nuclear Materials* **194,** 1408–1412 (1992).

91. Rickerby, D. & Fenici, P. Fatigue crack growth in thin section type 316 stainless steel. *Engineering Fracture Mechanics* **19,** 585–599. ISSN: 00137944 (1984).

92. Murase, Y., Nagakawa, J. & Yamamoto, N. In-beam fatigue behavior of 20% cold-worked 316 stainless steel at 300 °c. *Fusion Engineering and Design* **81,** 999–1003. ISSN: 09203796 (2006).

93. McKelvie, J. *Consideration Of The Surface Temperature Response To Cyclic Thermoelastic Heat Generation* in *SPIE 0731, Stress Analysis by Thermoelastic Techniques* (ed Gasper, B. C.) (Apr. 1987), 44. http://proceedings.spiedigitallibrary.org/proceeding.aspx?doi=10.1117/12.937886.

94. Dulieu-Smith, J. M. Alternative calibration techniques for quantitative thermoelastic stress analysis. *Strain* **31,** 9–16. http://onlinelibrary.wiley.com/doi/10.1111/j.1475-1305.1995.tb00949.x/abstract (1995).

95. Tomlinson, R. A., Nurse, A. D. & Patterson, E. A. On Determining Stress Intensity Factors For Mixed Mode Cracks From Thermoelastic Data. *Fatigue & Fracture of Engineering Materials & Structures* **20,** 217–226 (1997).

96. Muskhelishvili, N. I. *Some Basic Problems of the Mathematical Theory of Elasticity* ISBN: 978-90-481-8245-9. http://link.springer.com/10.1007/978-94-017-3034-1 (Springer Netherlands, Dordrecht, 1977).

97. Murakami, Y., Kanezaki, T., Mine, Y. & Matsuoka, S. Hydrogen embrittlement mechanism in fatigue of austenitic stainless steels. *Metallurgical and Materials Transactions A: Physical Metallurgy and Materials Science* **39 A,** 1327–1339. ISSN: 10735623 (2008).

98. Ziegler, J. F., Ziegler, M. D. & Biersack, J. P. SRIM - The stopping and range of ions in matter (2010). *Nuclear Instruments and Methods in Physics Research, Section B: Beam Interactions with Materials and Atoms* **268,** 1818–1823. ISSN: 0168583X. http://dx.doi.org/10.1016/j.nimb.2010.02.091 (2010).

99. Stoller, R. *et al.* On the use of SRIM for computing radiation damage exposure. *Nuclear Instruments and Methods in Physics Research Section B: Beam Interactions with Materials and Atoms* **310,** 75–80. ISSN: 0168583X. http://dx.doi.org/10.1016/j.nimb.2013.05.008%20https://linkinghub.elsevier.com/retrieve/pii/S0168583X13005053 (Sept. 2013).

100. Bubsey, R., Jones, M. & W.F, B. *Clevis Design for Compact Tension Specimens used in Plane-Strain Fracture Toughness Testing* tech. rep. (1969).

101. Rosencwaig, A. & Gersho, A. Theory of the photoacoustic effect with solids. *Journal of Applied Physics* **47,** 64–69. http://dx.doi.org/10.1063/1.4937565%7B%5C%%7D0Ahttp://aip.scitation.org/toc/jap/118/23 (1975).

102. Aerospace Specification Metals Inc. *ASM Matweb* http://asm.matweb.com (2019).

103. Yang, Y., Crimp, M., Tomlinson, R. a. & Patterson, E. a. Quantitative measurement of plastic strain field at a fatigue crack tip. *Proceedings of the Royal Society A: Mathematical, Physical and Engineering Sciences* **468,** 2399–2415. ISSN: 1364-5021 (2012).

104. Tomlinson, R. A. & Patterson, E. A. *Examination of Crack Tip Plasticity Using Thermoelastic Stress Analysis* in *Thermomechanics and Infra-red Imaging Volume 7* (2011). ISBN: 978-1-4614-0206-0. http://www.springerlink.com/content/u420331217151735/.

105. Sebastian, C., Hack, E. & Patterson, E. An approach to the validation of computational solid mechanics models for strain analysis. *Journal of Strain Analysis for Engineering Design* **48,** 36–47. ISSN: 03093247 (2013).

106. Christian, W. & Patterson, E. A. *Euclid* 2018. http://www.experimentalstress.com/software.htm.

107. Wong, A. K., Sparrow, J. G. & Dunn, S. A. On the revised theory of the thermoelastic effect. *Journal of Physics and Chemistry of Solids* **49,** 395–400. ISSN: 00223697. http://linkinghub.elsevier.com/retrieve/pii/0022369788900996 (Jan. 1988).

108. Wong, A. K., Dunn, S. A. & Sparrow, J. G. *Residual stress measurement by means of the thermoelastic effect* 1988.

109. Dunn, S. A., Lombardo, D. & Sparrow, J. G. The Mean Stress Effect in Metallic Alloys and Composites. *SPIE* **1084,** 129–142 (1989).

110. Krapez, J.-C. & Pacou, D. *Thermography detection of damage initiation during fatigue tests* in *AeroSense 2002* (2002), 435–449. http://proceedings.spiedigitallibrary.org/proceeding.aspx?articleid=884918.

111. Enke, N. F. An Enhanced Theory for Thermographic Stress Analysis of Isotropic Materials. *SPIE* **1084,** 84–102 (1989).

112. Luong, M. P. Infrared thermographic scanning of fatigue in metals. *Nuclear Engineering and Design* **158,** 363–376. ISSN: 00295493 (1995).

113. Shiozawa, D., Inagawa, T., Washio, T. & Sakagami, T. Accuracy improvement in dissipated energy measurement by using phase information. *Measurement Science and Technology* **28.** ISSN: 13616501 (2017).

114. Wong, A. K., Jones, R. & Sparrow, J. G. Thermoelastic constant or thermoelastic parameter? *Journal of Physics and Chemistry of Solids* **48,** 749–753. ISSN: 00223697 (1987).

115. Ohta, A., Kosuge, M. & Sasaki, E. Fatigue crack closure over the range of stress ratios from -1 to 0.8 down to stress intensity threshold level in HT80 steel and SUS304 stainless steel. *International Journal of Fracture* **14,** 251–264. ISSN: 03769429 (1978).

116. Shiozawa, D., Inagawa, T., Washio, T. & Sakagami, T. Fatigue limit estimation of stainless steels with new dissipated energy data analysis. *Procedia Structural Integrity* **2,** 2091–2096. ISSN: 2452-3216. https://www.sciencedirect.com/science/article/pii/S2452321616302736?via%7B%5C%%7D3Dihub (Jan. 2016).

117. Ranganathan, N., Jendoubi, K., Benguediab, M. & Petit, J. Effect of R ratio and ΔK level on the hysteretic energy dissipated during fatigue crack propagation. *Scripta Metallurgica* **21,** 1045–1049. ISSN: 00369748. https://linkinghub.elsevier.com/retrieve/pii/003697488790247X (Aug. 1987).

118. Klingbeil, N. W. A total dissipated energy theory of fatigue crack growth in ductile solids. *International Journal of Fatigue* **25,** 117–128. ISSN: 01421123 (2003).

119. Bär, J. & Urbanek, R. Determination of dissipated energy in fatigue crack propagation experiments with lock-in thermography. *Frattura ed Integrita Strutturale* **13,** 563–570. ISSN: 19718993 (2019).

120. Soppera, N., Dupont, E. & Bossant, M. *JANIS Book of proton-induced cross-sections* http://www.oecd-nea.org/janis/book/book-proton.pdf (OECD NEA Data Bank, 2012).

121. Spencer, R. P. & Patterson, E. A. Observations of fatigue crack behaviour in proton-irradiated 304 stainless steel. *Fatigue & Fracture of Engineering Materials & Structures,* ffe.13087. ISSN: 8756-758X. https://onlinelibrary.wiley.com/doi/abs/10.1111/ffe.13087 (July 2019).